Computer Simulation of Bottom Hole Cleaning in Oil-Well Drilling operations

By

Alireza Zakeri

Submitted in accordance with the requirements for the degree of

Doctor of Philosophy

School of Chemical and Process Engineering

University of Leeds

August 2021

Declaration

The candidate confirms that the work submitted in his own and that appropriate credit has been given where reference has been made to the work of others.

Alireza Zakeri August 2021

Acknowledgements

My most sincere gratitude must be expressed first to my supervisor, Dr Ali Hassanpour and Dr Mohammadreza Alizadeh whom have both provided me with invaluable guidance on all aspects of my research and encouragement throughout the duration of my studies.
I would like to thank the EPSRC for the project funding (EP/N509681/1) and support at university of Leeds.

I would like to extend gratitude to Professor Hakan Nilsson at Chalmers university of technology in Sweden for the guide through my first steps starting with OpenFOAM and

Dr Chris Greenshields, co-founder and director of CFD Direct London.

I am very grateful to my family, particularly Zobaideh Haydari, my wife, for all the support from beginning to the end of this project. Without her support, completion would have not been possible.

Dedication

This thesis is dedicated to my late mother, Hajar Zerafat (1943-2019), who at birth, saw the potential in me and never ceased to reiterate it in the time I spent with her.

Abstract

Oil-well cleaning operation is the ability of a drilling fluid to transport drilled cuttings from the bottom hole to the surface through the annular space between the drill string and the drilled hole (annulus). Better well cleaning leads to more efficient drilling operation which lowers the cost of development. In order to predict and prevent the cuttings accumulation at the bottom hole, it is essential to study the critical parameters affecting the cuttings transport. Computational model is one of the helpful methods to predict the hole-cleaning process as experiments are somewhat difficult and expensive to be carried out due to the harsh drilling conditions. Furthermore, having a good understanding about the physical properties of the particles (cuttings) and in-depth analysis of transport phenomenon can help the researchers to identify strategies to improve the cleaning efficiency. In spite of the extensive investigations carried out in this field, few numerical studies have been conducted considering the effect of particles dynamics and interactions in the fluid domain. Most of the modelling studies are limited to the methods which do not fully consider the discrete nature of cuttings in fluids. Nevertheless, very few investigations implemented fully coupled particle-fluid interactions, while there is a lack of focus and careful investigations of effect of cutting size with appropriate mesh configuration and refinement for particle-fluid interaction near the wall regions of annulus. This is significantly important for the transportation, sedimentation and suspension of cuttings. Moreover, a systematic study of the effect of mud rheology on cuttings transport in a fully coupled CFD-DEM is still lacking in the literature. This study is focused on modelling of the hole-cleaning process using fully coupled computational fluid dynamics and discrete element method (CFD-DEM) approach with carful mesh configuration, for particle-fluid interaction near the annulus wall regions. The aim is to identify the effective strategy for the removal of generated cuttings in oil-well drilling operation from bottomhole to the surface in order to avoid cuttings concentration in the wellbore. This study employed a coupled computational fluid dynamics/discrete element method (CFD-DEM) to predict and optimise the hole-cleaning efficiency of drilling fluid (mud) in different drilling conditions. Simulations have been carried out to investigate the dynamic behaviour of cuttings where the rheology of fluid phase is expressed by the Herschel-Bulkley non-Newtonian model, in an Eulerian framework (CFD) and the cuttings are modelled using the Lagrangian approach (Discrete Element Method, DEM). The CFD-DEM coupled approach,

considers the particle-particle, particle-wall, particle-fluid and fluid-particle interactions. In this work, the effects of cuttings size, drill rotation, inclination angles, mud rheology and annular velocity on the cleaning efficiency are investigated. The simulations input parameters have been chosen based on the data reported in the literature. It has been found that the role of mud viscosity and annular velocity in improving the cleaning efficiency are dominant while they can be increased to their maximum/limiting values. Increasing the well deviation from vertical position leads to higher cuttings concentration particularly at the inclination angles close to horizontal. Interestingly at low annular velocity the cuttings concentration at the inclined $45°$ well is found to be higher than the horizontal annulus due to the sliding motion of cuttings on the lower section of the annulus. Overall, the drill pipe rotation has little effect on decreasing cuttings concentration but the effect is more pronounced at low annular velocity, nevertheless it does not change the behaviour of cuttings at $45°$ as compared to the horizontal well.

The overall results from fully coupled CFD-DEM in this study can be used to improve the cleaning efficiency in vertical and deviated annuli in oil and gas drilling.

Table of Contents

List of Figures

List of Tables

Nomenclatures

Roman Letters

Re_r	Relative Reynolds number
Rep	particle Reynolds number
D_p	particle diameter
D_{hyd}	Hydraulic diameter
C_D	Drag force
u_f	fluid velocity
u_p	particle velocity
St	Stokes number
D_T	throat diameter
V_s	Slip velocity
F_D	Drag force
Cc	Cuttings concentration
F_r	Froude number
T_a	Taylor number
T_r	Temperature ratio
Va	Annular velocity
S_f	cell volume interaction force
F^{f-p}	particle-fluid interaction force
F_c	Contact force
F_g	Gravitational force
C_{fr}	Coefficient of rolling friction
f^d	steady drag force
$f^{Saffman}$	Saffman force
f^{Magnus}	Magnus force
T_R	Rayleigh time step
PV	plastic viscosity

Greek Alphabets

$\propto_p$	Volume fraction of particle phase
$\propto_q$	Volume fraction of continuous phase
μ_f	viscosity of fluid
μ_{ap}	Apparent Viscosity
μ_{yield}	Yielding viscosity
ν	kinematic viscosity
ρ_f	Density of fluid
ρ_p	density of particle
τp	particle response time
τ_f	fluid response time
ε	turbulence dissipation rate
τ_k	Kolmogorov time scale
Πmom	Momentum flux
ω	Drill pipe rotation

List of Acronyms

DEM	Discrete Element Method
DPM	Dense particle method
TFM	Two fluid model
LPT	Lagrangian particle tracking
RANS	Reynolds average Navier-Stokes
DNS	Direct numerical simulation
LES	Large eddy simulation
CFD	Computational fluid dynamics
RES	Reynolds Stress method
RCC	Relative cuttings concentration
ROP	Rate of penetration
LVM	Low-viscosity mud
IVM	Intermediate-viscosity mud
HVM	High-viscosity mud

Chapter 1

Introduction

1. Introduction

1.1 Context of Research

Rotary drilling has been introduced for oil and gas exploration and production Since 1880s as an effective method for well drilling. In rotary drilling, the drilling operation is carried out by rotating a drill bit which is suspended on sets of drill pipes, forming a drill string. The drill string is usually rotated by the rotation of drill string using a rotary table or top drive on the surface. In some cases, particularly directional drilling, the bit is rotated by hydraulic means, using the flow of a drilling fluid, commonly known as mud, through a turbine (mud motor) installed in the bottom section of the drill string, just behind the drill bit.

Further illustration can be seen in Fig. 1.The rocks are drilled by the bit rotation while an axial load is exerted on the bit using a fraction weight of drill string (weight on the bit (WOB)). As the drilling progresses, broken rocks, known as cuttings, have to be removed from the hole, in order to drill further. This is done by the circulation flow of drilling fluid (mud) which is pumped from mud pits, through the drill string down the hole and flushed out of the drill bit into the bottom hole section, flowing upward through the annular space between the drill string and the drilled well walls, a process which is known as bottom hole cleaning.

Since the introduction of rotary drilling, the circulation of mud has become a critical component of the drilling operation. The flowing mud transports the generated cuttings from bottom hole of the well and takes it back up to the surface through the annular space between the drill pipe and the hole wall. The cuttings are filtered out, the mud will be treated in mud pit and returns back to the cycle.

Hole cleaning in drilling operation can be assessed by the function of mud. The ability of the mud to lift the generated cuttings from the bottomhole and carrying it out to surface through the annulus is generally referred as the carrying capacity of mud. Consequently, an optimum cleaning efficiency can be affected by the most relevant parameters involving in carrying capacity of mud in cutting transport. The most significant factors are hole-inclination, mud velocity, mud rheological properties, cuttings parameters (size, shape, and density), cutting volume concentration (as an index of deposition) etc.

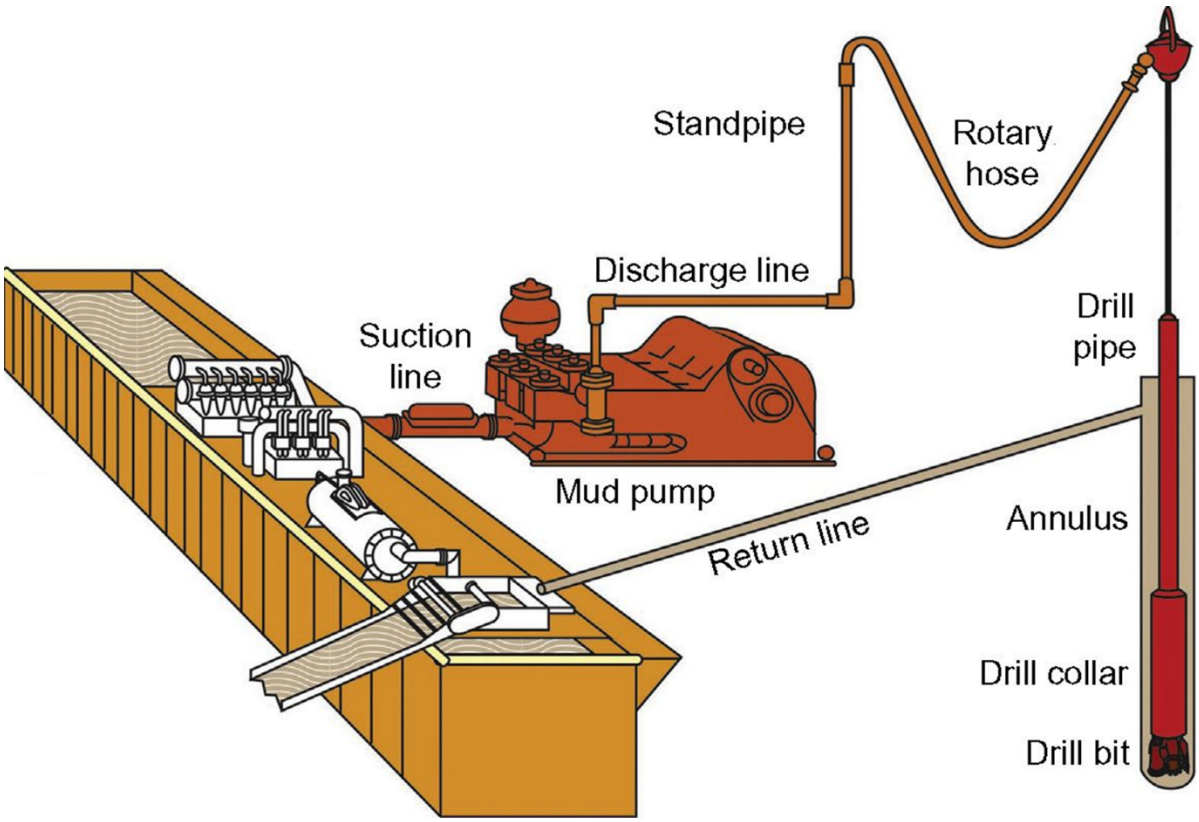

Fig. 1. Schematic figure of drilling operation [1].

Fig. 2. Drill bit [1].

After drilling and interval, the open-hole section of the well is protected by a steel pipe namely casing, which is inserted in the borehole and cemented onto the wall of the well. This safety isolation provides structural integrity to the wellbore. For the next interval of drilling, a smaller drill bit is used to drill from the bottom of casing, while the mud is still in circulation, but this time flows into the different annular spaces, i.e. the open hole section and the cased hole. The mud system is the single component of the well-drilling operation that remains in contact with the wellbore throughout the entire drilling process and is an important element of drilling. Drilling muds are divided into types:1) water-based drilling mud and 2) oil-based drilling mud.

With the challenges and in the era of low oil prices, selection of the mud type and its properties is essential to optimizing the drilling time and cost. Water-based muds (WBMs) including fresh water, seawater, brine, are used depend on well condition or on the specific interval of well drilling. In general, the water-based muds are more satisfactory for the vertical well at medium depth. Water-based muds are less expensive and more preferred in drilling operations as they are environmentally friendly. However, under more complicated drilling condition with the presence of Shale in drilling process, the mud need to maintain a high pressure and be able to forbearing a high temperature; hence, oil-based muds are often desired due to their greater drilling performance [2].

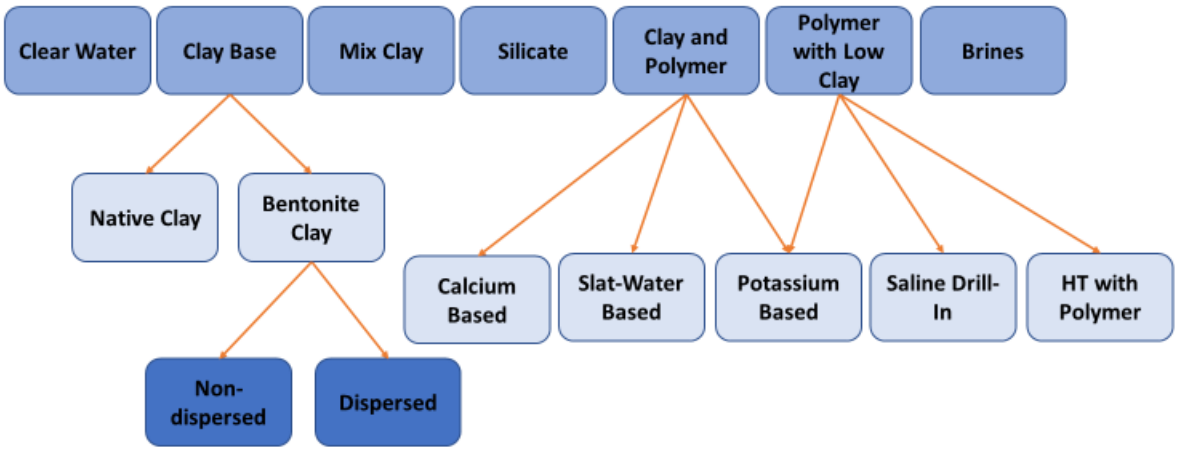

Fig. 3. Classification chart for water-based mud.

Oil-based muds (OBMs) are suitable for greater depth in directional drilling with greater stress on the drilling devices due to their tolerant against high temperature. While OBM is often preferred for its better performance in drilling a complicated well, as it can simply combat with the drilling problems. For instance, Barite is used to rise the system density and bentonite is the Viscosifier in oil-based system.

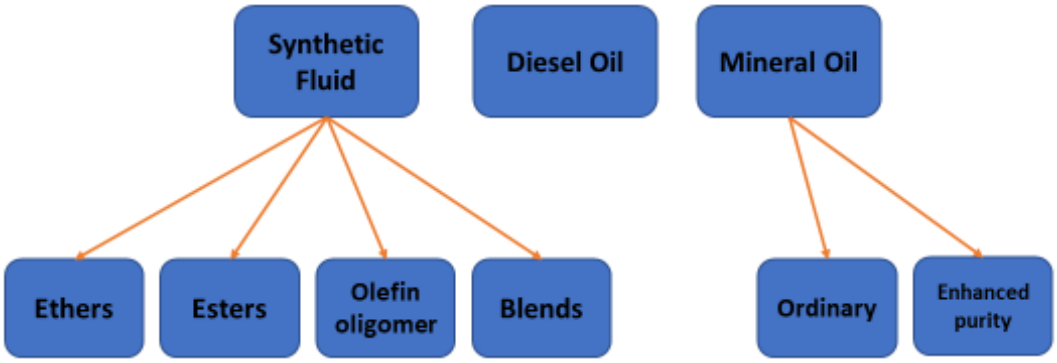

Fig. 4. Classification chart of Non-water-based mud.

A large-scale study of cutting transport has been carried out to facilitate the optimum design of drilling fluid system. These efforts have been conducted by experimental techniques, modelling or simulation to investigate the key factors affecting cuttings transport. Measurement and visualization of mud parameters at bottomhole is not feasible during the drilling operation. On the other hand, it is difficult to obtain accurate and realistic data while studying the impact of these parameters simultaneously. Therefore, the concept of cuttings transport can be observed better via simulation techniques. In addition, the running costs and health and safety issues make it difficult to experimentally investigate these operations empirically.

Many numerical researchers have used Computational Fluid Dynamics (CFD) to simulate the cuttings transport in wellbore annulus through the two-phase flow theory, nevertheless the dynamic behaviour of particles has not been fully reflected. Akhshik et al. [3] presented coupled Computational Fluid Dynamics (CFD) and Discrete Element Method (DEM) approach to study the drill pipe rotation in cleaning efficiency where they considered the bulk properties of cuttings such as the flow velocity, cuttings size, fluid rheology and their results showed good agreement with experimental data of Osgouei et al. [4]. Furthermore, Akhshik

et al. [5] studied the impact of the microscopic properties of cuttings collision on the characteristics of the cuttings transport mechanism in order to reach the optimum cleaning efficiency. Despite extensive research in the field, there are still challenges to be addressed. Most of the recent studies are suffering from lack of mesh refinement for particle-fluid interaction near the wall region which is significantly important for the sedimentation and suspension of cuttings. Moreover, a systematic study of the effect of mud rheology on cuttings transport in a fully coupled CFD-DEM is still lacking in the literature.

In this work, the mathematical modelling technique used is based on Reynolds Stress Model (RES) embodied in the commercial CFD code FLUENT, with flow solutions provided by this method coupled to a second commercial code, EDEM, based on Discrete Element Method (DEM) used in the prediction of particles (cuttings) transport in annulus and improve the cleaning efficiency. In this study, careful consideration has been given to the mesh arrangements and refinements near the wall. Furthermore, effects of cutting size, drill string rotation, inclination angle and rheological properties of water-based mud, i.e. low-viscosity bentonite, intermediate viscosity mud and high-viscosity bentonite, are carried out in simulations.

1.2 Aims and Objectives

There is insufficient uniformity and comprehensiveness in available literature for cuttings transport at annulus and bottom of wellbore in oil-well drilling operation. This is consequence of several reasons (related to harsh condition of drilling process and complexity of particles/cuttings collision at bottomhole) and is increased by the uncertainty in methodologies, mainly owing to large number of physical and computational parameters involved and ignoring the particle collision impact.

The work presented in this study is step toward better understanding the mud rheology and dynamic behaviour of particles in the fluid domain due to drill sting rotation. The main objectives of this report are set on the list given below:

1. Using CFD coupled with DEM to simulate cuttings transport process in the bottomhole
2. Employing three types of mud viscosity (low, intermediate and high viscosity) to investigate their impact on cutting transport in annulus
3. Study the effect of cutting size, mud rheology, annular velocity, inclination angle, and drill pipe rotation on the cuttings transport and hole-cleaning efficiency

This work is structured according to the following format. Chapter 2 presents a review of previous experimental and computational approaches used in cuttings transport in consort with associated literature. In chapter 3, the methodology in particular the computational fluid dynamics (CFD) based on Reynolds stress model (RES) coupled with discrete element method (DEM) to study the behaviour of particles are outlined with a focus on the numerical methods, coupling procedure and fluid-particle contact models. Chapter 4 provides the studies on mud rheology and the effects of yield point on the cutting concentration and cleaning efficiency. Chapter 5 explores the impacts of inclination angle, cutting size, drill pipe rotation on cleaning efficiency. Chapter 6 provides a summary of the findings of this work, concluding comments and potential areas of future work.

Fig. 5. Thesis structural plan.

Chapter 2

Literature Review

2. Literature Review

2.1 Introduction

Hole cleaning is defined as the ability of mud to transport and suspend the drilling cuttings. The essential function of mud is the circulating capacity to lift and carry the cuttings to surface. Carrying capacity and solid transport are controlled by solid-liquid velocities and cuttings concentration [6]. The significance of mud flow in annulus leads us to understand solid-liquid phase behaviour in hole cleaning process.

This chapter begins by introducing some of the influential parameters when classifying particle-fluid phase flow, flowed by an overview of modelling and simulation techniques frequently used in this field. Furthermore, an overview of published work on previous numerical studies is given.

2.2 Introduction to Particle-Fluid Flow

Particle-fluid flow is simply consisting of two distinct phases flowing simultaneously in mixture where a phase can be defined as an identifiable class of material that has a similar response to and interaction with the field which it is immersed.

The transport of solid particles in liquid-Solid flow is studied where one of the phases is continuous (primary) and the other (secondary) is dispersed within the continuous phase. The volume fraction of the dispersed phase can be defined as:

$$\frac{Volume\ of\ the\ phase\ in\ a\ cell\ or\ domain}{Volume\ of\ the\ cell\ or\ domain} = Volume\ fraction\ of\ a\ phase$$

$$\propto_p = \frac{\delta V_p}{\delta V} \tag{2.1}$$

Where the volume fraction of continuous phase is:

$$\propto_q = \frac{\delta V_q}{\delta V} \tag{2.2}$$

Where the sum of the volume fractions must be:

$$\propto_q + \propto_p = 1 \tag{2.3}$$

2.2.1 Response Times

The interaction between particles and fluid flow is complex, due to all of the parameters involved; Particle response (relaxation) time is the required time for a particle to be released to achieve flow stream velocity. In other word, it is used to characterize the capability of particles to follow velocity changes in the flow.

Defining the dispersed phase Reynolds number as Relative Reynolds number:

$$Re_r = \frac{\rho|u_f - u_p|D_p}{\mu} \tag{2.4}$$

Where u_p is the particle velocity, u_f is the fluid velocity, D_p is the particle diameter, ρ is the density and μ is the viscosity of the continuous phase.

The equation of motion for a spherical particle inside a viscous fluid by considering only drag force is given below after dividing by particle mass and in terms of the particle Reynolds number:

$$\frac{du_p}{dt} = \frac{18\mu_f}{\rho_p D_p^2} \frac{C_D\, Re_p}{24} \left(u_f - u_p\right) \tag{2.5}$$

Where the drag force coefficient C_D is usually obtained from Rowe [7]:

$$C_D = \begin{cases} \frac{24}{Re} \;\; if\; Re_p < 1 \\ \frac{24}{Re_p}\left(1 + 0.15\, Re_p^{0.687}\right) \quad if\; 1 \le Re_p \le 1000 \\ 0.44 \;\; if\; Re_p > 1000 \end{cases} \tag{2.6}$$

In formula (2.5), for the limits of low Reynolds numbers, the $\frac{C_D\, Re_p}{24} \to 1$ where the $\frac{18\mu_f}{\rho_p D_p^2}$ factor has dimensions of reciprocal time that defines the velocity response time:

$$\tau_p = \frac{\rho_p D_p^2}{18\mu_f} \tag{2.7}$$

So, the equation of motion can be rewritten as:

$$\frac{du_p}{dt} = \frac{1}{\tau_p}\left(u_f - u_p\right) \tag{2.8}$$

The solution to the (2.8) equation for constant fluid velocity and initial particle velocity of zero is:

$$u_p = u_f(1 - e^{-\frac{t}{\tau_p}}) \quad (2.9)$$

Thus, the velocity response time is the time requires for a particle released from rest to achieve 63% ($\frac{e-1}{e}$) of the free stream velocity

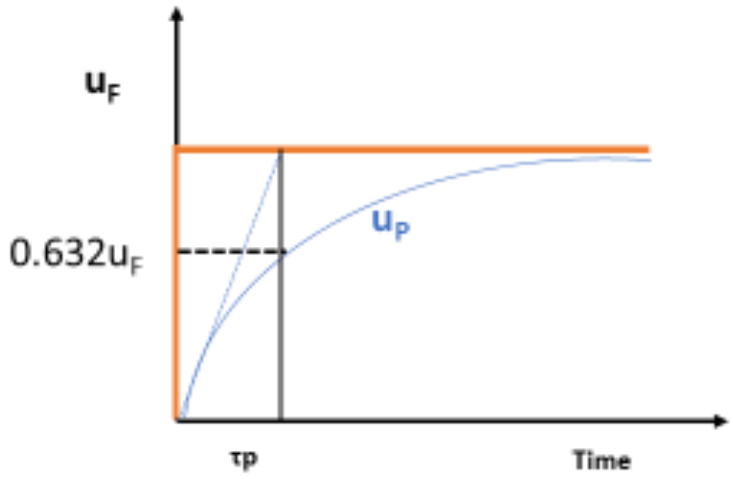

Fig. 6. Graphical illustration of the particle response time. Schwarzkopf, Sommerfeld [8].

2.2.2 Stokes Number

The Stokes number (St) is a very important (dimensionless) parameter in fluid-particle flows that related to the particle velocity. It is a characteristic time scale of the flow and can be defined as the ratio of the particle response time.

$$St = \frac{\tau_p}{\tau_f} \quad (2.10)$$

Where τ_f is the characteristic time of flow field and it can be defined as:

$$\tau_f = \frac{l}{u_f} \quad (2.11)$$

Where (l) is the length scale for instance it can be the throat diameter $(D_T)$for the flow through a Venturi tube. So, it can be rewritten as:

$$St = \frac{\tau_p u_f}{D_T} \quad (2.12)$$

If St≤1, the particle response time is much less than the characteristic time associated with the flow field. As a result, the particle has sufficient time to respond to changes in flow velocity. Consequently, the particle and fluid velocities will reach velocity equilibrium.

Conversely, if St≥1, the particle has no time to respond to changes in flow velocity the particle velocity will be unaltered.

The particle-fluid velocity ratio can be defined as a function of Stokes number and can be found from the "Constant Lag" solution. The velocity ratio is specified as $\emptyset = \frac{u_p}{u_f}$ and is assumed to vary slowly with time. Substituting this variable into equation (2.8), gives:

$$\emptyset \frac{du_f}{dt} = \frac{u_f}{\tau_p}(1 - \emptyset) \tag{2.13}$$

The carrier phase acceleration can be approximately expressed by:

$$\frac{du_f}{dt} \sim \frac{u_f}{\tau_f} \tag{2.14}$$

Substituted into equation (2.13), gives:

$$\emptyset\ St \sim (1 - \emptyset) \tag{2.15}$$

As a final point solving for ∅ gives:

$$\emptyset = \frac{u_p}{u_f} \sim \frac{1}{1+St} \tag{2.16}$$

If$St \to 0$, the particle velocity approaches the carrier phase velocity. If$St \to \infty$, the particle velocity approaches zero and the particle velocity is not affected by fluid phase.

2.2.3 Cuttings Slip Velocity

Cuttings slip velocity is the velocity of particles relative to the adjacent fluid. For instance, while particles experience an upward force by drilling fluid velocity, inversely the gravity force them downward (settling tendency of cuttings). Therefore, in cleaning process mud flow velocity should be greater than cuttings slip velocity, otherwise, the cleaning process fails (Fig. 7).

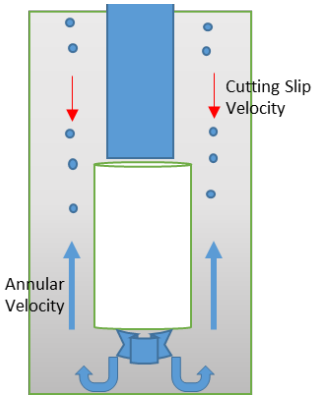

Fig. 7. Annular Velocity > Cutting Slip Velocity.

Various equations have been derived to evaluate the slip velocities of spherical particles in different flow regimes. The degree of applicability of theses equations depends on the particle Reynolds number and equation (2.4) can be rewritten as:

$$Re_p = \frac{\rho_f d_p V_s}{\mu} \tag{2.17}$$

Where particle Reynolds number (Re_p) is a function of slip velocity (V_s), diameter of particles (d_p), viscosity (μ) and density (ρ_f) of fluid.

According to equations (2.5) and (2.6) in turbulent flow, the drag coefficient becomes constant. Slip velocity can be calculated by Zeidler's equation[9]:

$$V_s = 9\sqrt{\frac{D_p(\rho_p - \rho_f)}{\rho_f}} \qquad Re_p > 1000 \tag{2.18}$$

In the intermediate range of Reynolds number, which particles in this study experience in the annulus, Stokes law relates the drag coefficient to the particle Reynold number. Thus,

$$V_s = \sqrt{\frac{4gD_p\,(\rho_p - \rho_f)}{3\rho_f C_D}} \qquad 1 < Re_p < 1000 \tag{2.19}$$

Zeidler equation has been derived for uniform and smooth spherical particles. In the case of irregular shaped particles, it is difficult to estimate an equivalent diameter based on sphericity and volume of particles.

2.2.4 Dilute vs. Dense Flows

A dilute particle-fluid flow is one in which the particle motion is affected by the fluid phase forces (mainly drag and lift). On the other hand, a dense flow is one in which the particle motion is affected by collisions or continuous phase contact.

The flow can be considered dilute if the ratio of particle response time to the time between collisions is smaller than one where the particles have enough time to respond the local fluid forces before the next collision.

$$\frac{\tau_p}{\tau_c} < 1 \tag{2.20}$$

Where (τ_c) is the average time between particle-particle collisions. Alternatively, the flow can be called dense if particles have no time to respond to the fluid forces before the next collision.

$$\frac{\tau_p}{\tau_c} > 1 \tag{2.21}$$

The time between particles collision can be estimated but there is no definitive scaling parameter that describes the boundary between dilute and dense flows.

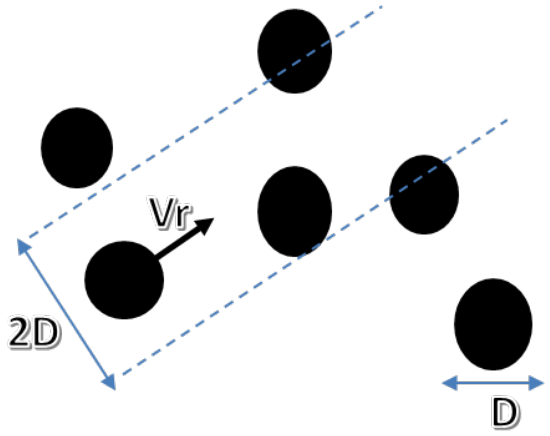

Fig. 8. Particle-Particle collisions.

A group of particles illustrates in Fig. 8 with uniform diameter D where one particle is moving with a relative velocity v_r with respect to the other particles. The one particle will intercept all the particles in tube with radius 2D, length $v_r \delta t$ and in a time δt. Thus, the number of particles in tube can be obtained from:

$$\delta N = n\pi D_p^2 v_r \delta t \tag{2.22}$$

Where (n) is the number density of particles and the collision frequency is defined by this equation:

$$f_c = n\pi D_p^2 v_r \tag{2.23}$$

Also, the time between collisions is:

$$\tau_c = \frac{1}{f_c} = \frac{1}{n\pi D_p^2 v_r} \tag{2.24}$$

Abrahamson [10] Suggested formula (2.22) for the particle collision frequency with a mean velocity of v'

$$f_c = 4\sqrt{\pi} n D_p^2 v' \tag{2.25}$$

The ratio of response time can be obtained with respect to collision frequency:

$$\frac{\tau_p}{\tau_c} = \frac{4n\sqrt{\pi}\rho_p D_p^4 v'}{18\mu_c} \tag{2.26}$$

The above formula after solving for the particle diameter:

$$D_p = \frac{3\sqrt{\pi}\ \mu_c}{4\rho_p v' \propto_p} \frac{\tau_p}{\tau_c} \tag{2.27}$$

Thus, the particle diameter can be used as a function of particle volume fraction ($\propto_p$) for different range of $\frac{\tau_p}{\tau_c}$ to classify dilute and dense flows.

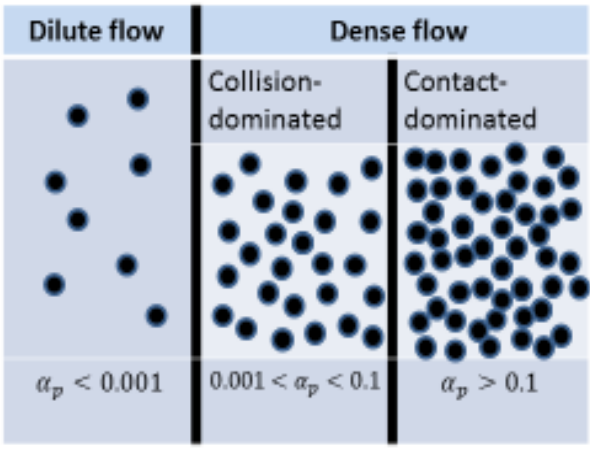

Fig. 9. Flow regimes for Dilute & Dense flows**.**

There are many mechanisms that are responsible for particle-particle collision thus it is difficult to distinguish the limits of dilute and dense flows. Nevertheless, the scale of particle volume fraction ($\propto_p$) provides a general scale as it is illustrated in Fig. 9.

2.2.5 Phase Coupling

A major concept in the analysis of particle-fluid flows is phase-coupling which significantly influences the behaviour of the continuous and dispersed phase and it can be determined by particle volume fraction ($\propto_p$). Elghobashi [11] Proposed the phase- coupling classification map, where a one-way coupling can be used for highly diluted flows with$\propto_p \leq 10^{-6}$.The particle trajectories is affected by flow of the carrier fluid phase but the particles cannot influence on the fluid phase flow. For volume fraction of $10^{-6} \leq \propto_p \leq 10^{-3}$ particles can affect the fluid phase flow so a two-way coupling can be used for additional forces exerted on the fluid flow by the particles. The degree of influence depends on the ratio of the particle response time ($\tau_p = \frac{\rho_p D_p^2}{18\mu_f}$) according to the formula (2.7) and the Kolmogorov time scale:

$$\tau_K = (\upsilon/\varepsilon)^{\frac{1}{2}} \tag{2.28}$$

Where (υ) is the kinematic viscosity and (ε) is the turbulence dissipation rate.

$$\tau_e = \frac{l}{u} \tag{2.29}$$

Where (τ_e) is the turnover time of large eddies in turbulent flow, (l) is the turbulent length scale and (u) is the velocity magnitude.

Large particle response time can enhance the turbulence production. Additional particle-particle collisions occur, as the volume fraction exceeds10^{-3}which is referred to four-way coupling. The classification of coupling schemes illustrated in Fig. 10 where phase (1) is for one-way coupling (negligible effect on turbulence). Phase (2) is for two-way coupling where particles enhance turbulence production also phase (3) is for two-way coupling where particles enhance turbulence dissipation. Phase (4) is for four-way coupling where the particle-particle interaction should be considered.

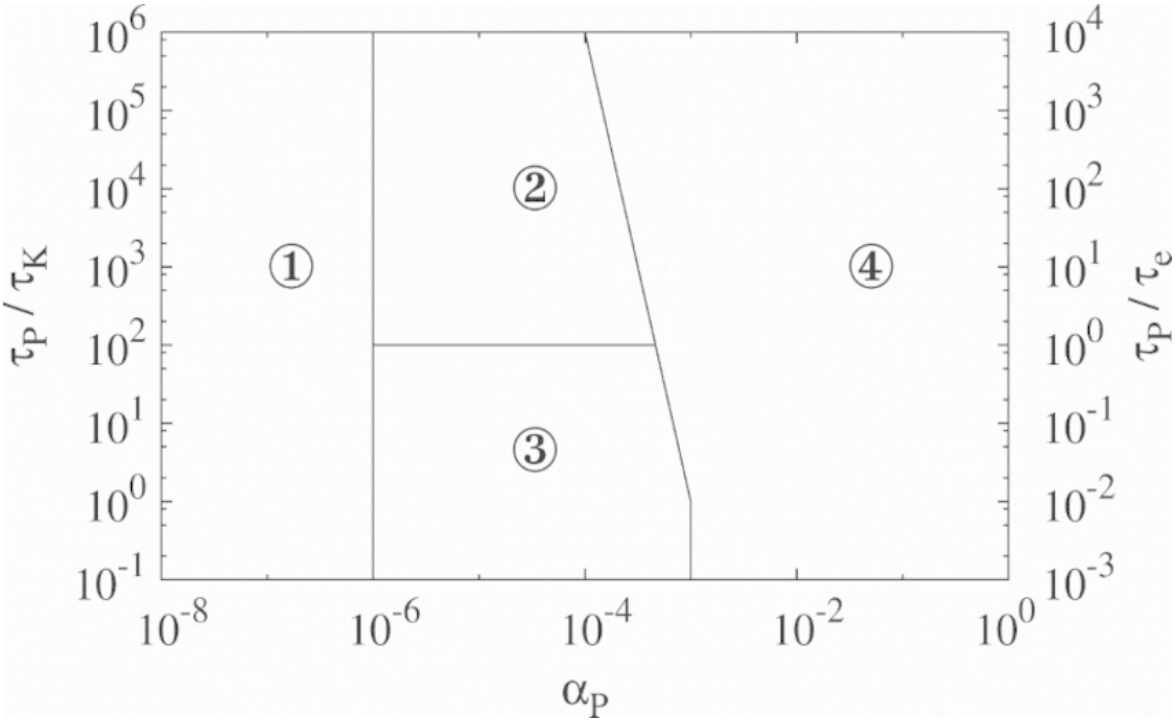

Fig. 10.Classification of phase-coupling according to Elghobashi [11].

Coupling can take place through the mass, momentum and energy transfer between particle and fluid phases, where momentum coupling is the result of drag forces on the dispersed and continuous phase and it can be assessed by comparing the drag force due to the dispersed with the momentum flux of the continuous phase.

$$\prod_{mom} = \frac{F_D}{Mom_c} \tag{2.30}$$

Above formula expressed the momentum coupling parameter where (F_D) is the drag force due to the particles in the volume and (Mom_c) is the momentum flux of fluid phase through the volume. After substituting the drag force associated with particles in volume with side (L) and momentum flux of continuous phase based on Stokes drag, the momentum coupling parameter can be rewritten:

$$\prod_{mom} = \frac{nmL}{\overline{\rho_c}\, u_f \tau_p} \left(1 - \frac{u_p}{u_f}\right) \tag{2.31}$$

Where (m) is the mass of an individual element of dispersed phase and the (nm) product represents the bulk density of the dispersed phase. So, the momentum coupling parameter can be approximated by:

$$\prod_{mom} \sim C \ \frac{L}{u_f \tau_p} \ (1 - \frac{u_p}{u_f}) \tag{2.32}$$

While the velocity factor is excluded, the momentum parameter depends on dynamics of the flow field and the ratio of $u_f \tau_p / L$ is the ratio of the time associated with momentum transfer to a time characteristic of the flow where the Stokes number for momentum transfer can be expressed as:

$$St_{mom} = \frac{\tau_p u_f}{L} \tag{2.33}$$

The momentum coupling parameter can be rewritten as:

$$\prod_{mom} = \frac{C}{St_{mom}} \ (1 - \frac{u_p}{u_f}) \tag{2.34}$$

If$St_{mom} \to 0$, the velocity of dispersed phase approaches the carrier phase velocity. Using formula (2.16) for the velocity ratio, gives:

$$\prod_{mom} = \frac{C}{1+St_{mom}} \tag{2.35}$$

Thus, the effect of momentum coupling enhances for the high concentrations and small Stokes number. On the other hand, it becomes negligible for small concentrations and large Stokes number.

2.3 Numerical Models for Particle-Fluid Flow

2.3.1 Numerical Approaches to Particle Phase

There are different methods for the modelling of particulate phase in particle-fluid flow, where the ideal approach would resolve the dynamics properties of each particle in the system. In Discrete Element Method (DEM), the motion of each particle is investigated including the contact forces, the fluid dynamic forces and the moments regarding to the neighbouring particles. In Discrete Parcel Method (DPM), a group of particles with same properties (size, velocity, shape, etc.) called parcel, represented by one computational particle, so the equations of motion are solved for the parcels as they moved through the flow field. In Two-Fluid models, the properties of the particles are assumed to be continuous and treated as a separate fluid.

These three approaches (DEM, DPM and TFM) can be can categorized into Eulerian modelling (TFM) or Lagrangian particle tracking (DEM & DPM) methods. In the Eulerian approach, conservation equations are solved simultaneously for each node in the field, where in the Lagrangian approach, the motion of particles individually are tracked through the field as they pass the point in the field.

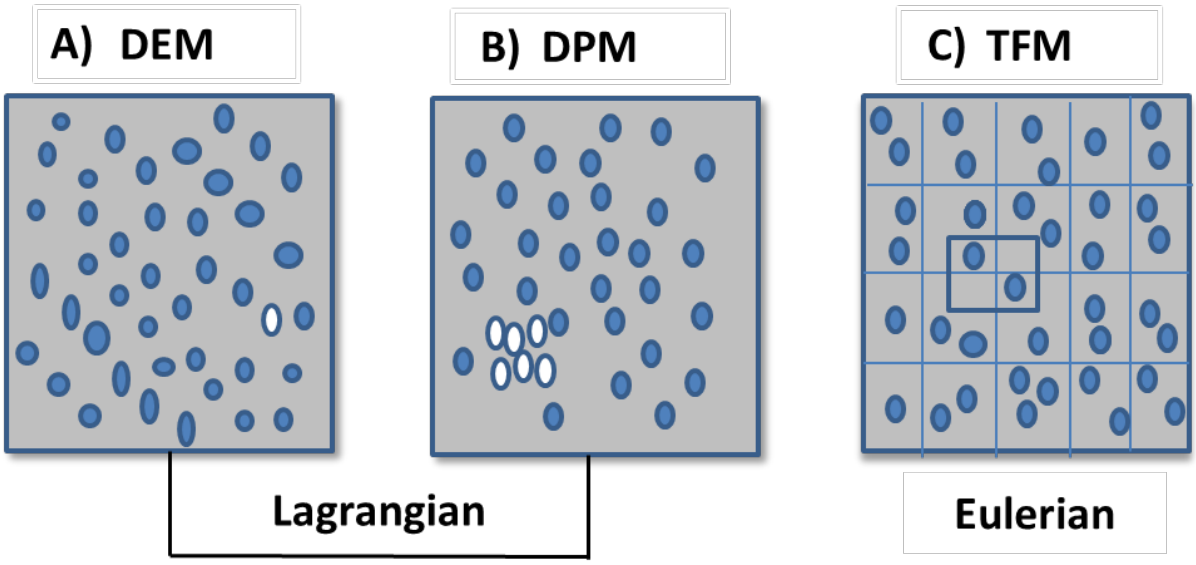

Fig. 11. Different particle-phase approaches.

2.3.2 Numerical Approaches to Fluid Phase

The continuous phase in a particle-fluid flow is always modelled using the Eulerian approach where the motion and properties of particles are calculated based on the continuous phase velocity and in a “complete” numerical simulation, it obtained by solving Navier-Stokes equations with suitable boundary conditions consistent to the particle surface and walls. This method can be called Reynolds Average Navier-Stokes (RANS) approach which is limited the application to a few particles at low Reynolds number due to high computational cost of the simulations.

Direct Numerical Simulation (DNS) is an approach with focus on the modelling of the fluid phase turbulence and the Navier-Stokes equations are solved numerically for the higher frequencies and the smallest scales of turbulence. Therefore, at every point in the flow, through proper interpolation, the flow velocity is available. The “point” particles are not occupied any volume of the flow field. This method is also limited to low Reynolds numbers.

Large Eddy Simulation (LES) is an approach to model a turbulent flow field where the Navier-Stokes equations are “filtered” hence the numerical calculations produce the large-scale turbulent eddy motion and the small scale is modelled with a residual stress tensor. This method enables simulations at higher Reynolds numbers.

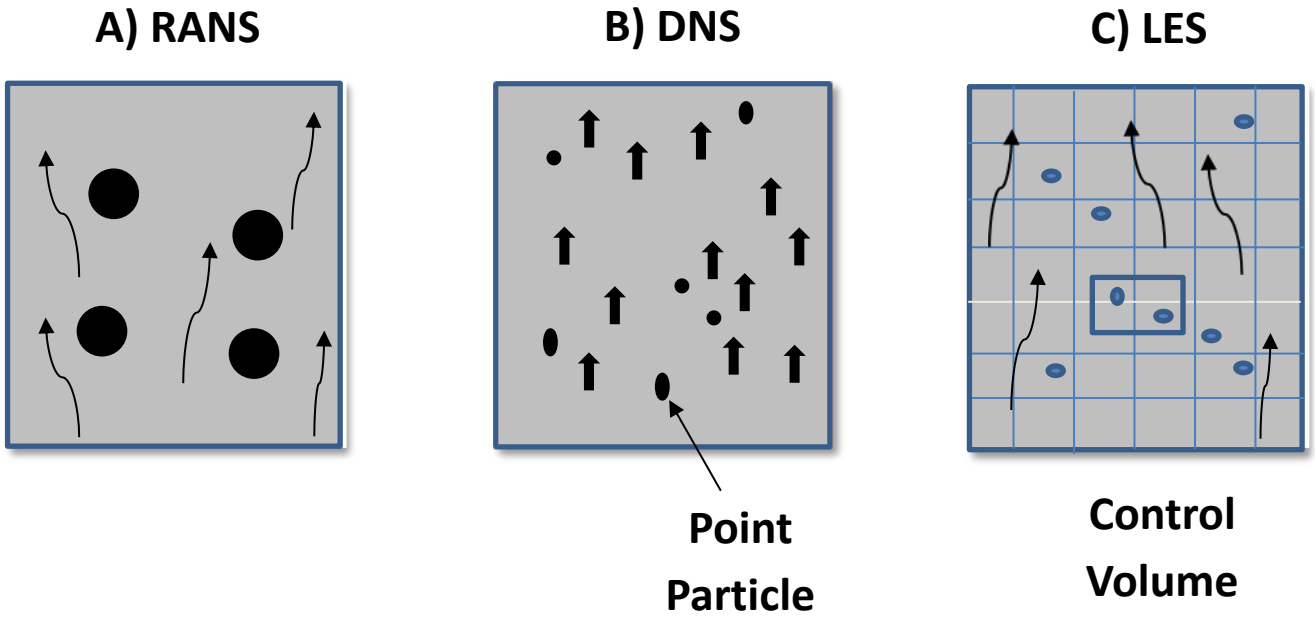

Fig. 12.Different fluid-phase approaches.

2.4 Review of Experimental and Numerical Studies

2.4.1 Experimental Studies

The cleaning process of oil-well drilling operation is the ability of the drilling fluid to eventuate cuttings transport optimisation and prevent the accumulation of those cuttings at bottom hole during the drilling operation. This is carried out to reduce the drilling cost and improve the penetration rate. So, the cleaning efficiency is a function of different parameters in drilling operation. Due to harsh drilling conditions and high cost of these operations, numerical studies are becoming more popular in compare with experimental investigations as result of recent progress in the simulation algorithm and computational power. Although, effect of different parameters was studies experimentally. One of the first studies on the drilling cuttings was by Zeidler [9]. His laboratory tests were carried out to study the removal of drilled cuttings in a well borehole simulated annulus. He found the influential impact of pipe rotation and turbulent flow in mud drilling circulation resulting a better hole cleaning performance. Later, Okrajni and Azar [12] studied the impact of rheological properties based on the field-measured data on cuttings transport in different flow regimes. They considered the impact of different inclination angles on cuttings transport (Fig. 13). They found the most critical inclination angles in the rage of 45^0 to 55^0. In addition, they showed under laminar flow regime, higher mud yield values provide higher cleaning efficiency in the range of 0^0 to 45^0 inclination angles but not effective in range of 55^0 to 90^0. They recommended the cuttings transport was not generally affected by the mud rheological properties under turbulent flow regime. Brown, Bern [13] at BP research centre carried out similar investigations and suggested the most critical inclination angles in the range of 50^0 to 60^0.

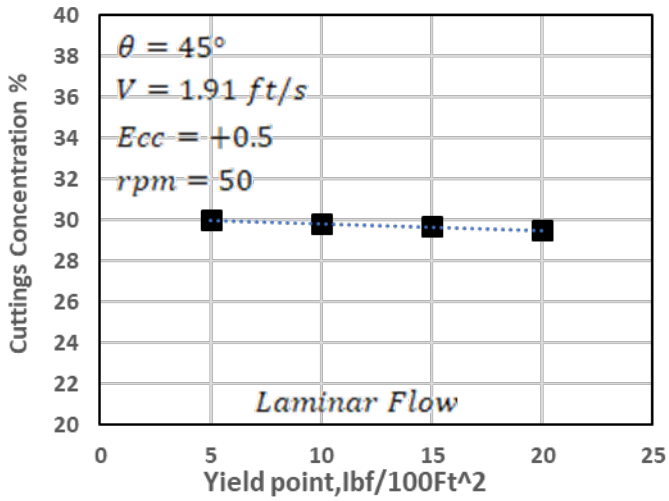

Fig. 13. Effect of yield value on cuttings concentration at inclination angle of $\mathbf{45^0}$[10].

Tomren and Azar [14] studied the drilling cutting transport process in directional wells by experimental approach. They found higher annular velocities are required in directional well to perform effective hole cleaning operation. They observed better performance of high-viscosity mud in cuttings transport in comparison with the low-viscosity muds. They found an increase in hole angle reduces the transport performance where the hole angles of 40 to 50^0 are critical due to cuttings build-up and downward sliding of the bed of cuttings (Fig. 14).

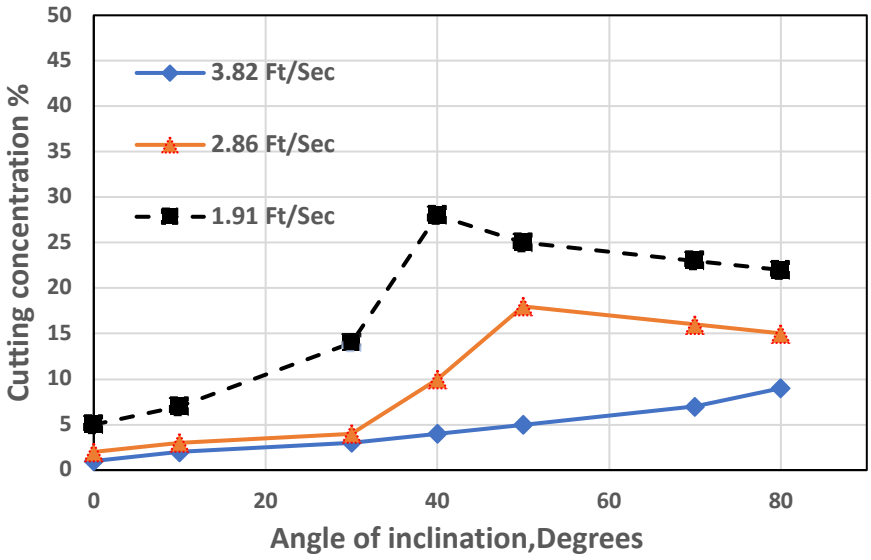

Fig. 14. Variation of cuttings concentration with inclination angles **[14]**.

Peden, Ford [15] carried out studies on the impact of drill pipe rotation, inclination angles and cuttings size using experimental facilities at Herriot-Watt University have proven the significant influence of pipe rotation in transportation of the drilling cuttings. Furthermore, they found the angles in range of 40 to 60^0 are the most the difficult angles to transport the cuttings. They reported that the transport of larger particles was easier than small ones.

Sifferman and Becker [16] analysed the impact of the particle size on the cutting transport and prove that in the range of angles close to the horizontal line with smaller diameter particles, drill pipe rotation had significant effect on cuttings transport.

Bassal [17] studied the impact of particle size (2-7mm) on cuttings transport and found the difficulty of smaller particles size transportation in compared with larger ones in hole cleaning process. Later, Sanchez, Azar [18] conducted over 600 tests to study drilling cuttings transport using the Bassal's experiment particle size (2-6mm) and found the difficulty of smaller particles transportation as compared with the larger ones in hole-cleaning process. Alfredo Sanchez, Azar [19] carried out their experimental investigations on impact of drill pipe rotation and they suggested the dramatic effect of the rotation pipe, specifically in angles close to the horizontal line. In the case of fine particles, the implementation of high-speed rotation with high viscous drilling mud was recommended to improve the cleaning process.

Yu et al. conducted a full scale experimental study of hole cleaning under simulated conditions to develop the correlations formulas that can be used for field operations [20].

The effects of drilling mud rheology, mud density, borehole inclination, pipe rotation, eccentricity and rate of penetration (ROP) were investigated in their experimental study. They selected a variety of muds with different rheological parameters and densities to conduct their experiments and provide their correlation formula in which the cutting concentration is related to the dimensionless parameters:

$$C_c = 0.062 F_r^{-1.31} Re^{0.157}\, T_r^{0.165} Drp^{0.045} \tanh\left(1 + 0.0043 T_a\right) \tag{2.1}$$

$$\begin{cases} F_r = \dfrac{V_a}{\sqrt{g(D-d)}} \\ T_a = \dfrac{\rho_f * \Omega * (D_{hyd}{}^2)}{\mu} \end{cases} \tag{2.2}$$

Where C_c is the cutting concentration, T_a is the Taylor number, F_r is the Froude number, μ is the mud viscosity, V_a is the annular velocity, Ω *i*s the drill pipe rotation speed, Re is the generalized Reynolds number, Drp is the dimensionless rate of penetration (ROP), *D* is the outer diameter and *d* is inner diameter of annulus respectively, D_{hyd} is the hydraulic diameter of annulus and T_r is the temperature ratio.

A comparison of cuttings concentration calculated by equation (2.1) with filed data is illustrated for different mud (Fig. 15) and water (Fig. 16) which indicates that the regressed correlation is sufficiently accurate to predict the cuttings concentration for full scale experimental study where the cuttings size distribution is not considered.

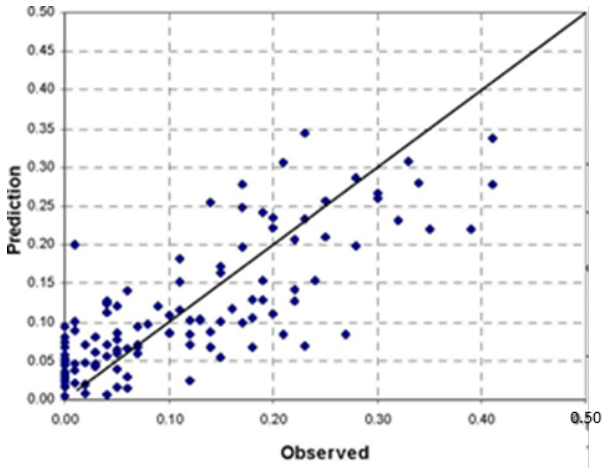

Fig. 15. Comparison between model perdition with experimental data[20].

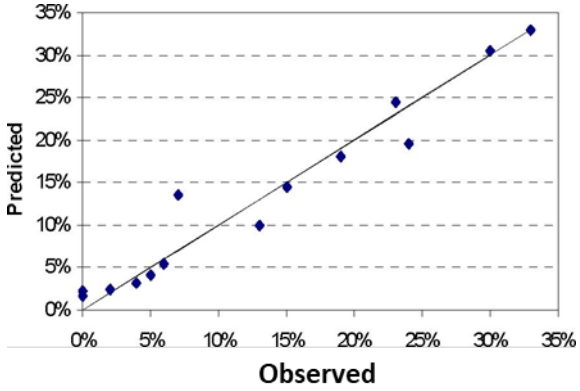

Fig. 16. Observed versus predicted cuttings for water[20].

In the above-mentioned studies, they tested different drilling strategies on cleaning optimisation by utilising the laboratory-scale drilling rigs. The most prevalent challenge for

the experimental studies is attaining the mud rheology based on the temperature and pressure during the actual drilling operation. Moreover, during the rig performance, the risk of operation due to the high temperature and pressure condition for the laboratory environment is quite high. Considering operational limits and boundaries besides unexpected situations which typically occur during the drilling processes, it is difficult and relatively expensive to create a well-designed and controlled full-scale laboratory rig in order to obtain highly accurate and reliable experimental results. A reliable numerical simulation can help to understand the hole cleaning process while investigating the effects of various key parameters in cuttings transport simultaneously.

Table 1. Experimental Studies in Hole Cleaning Process

Author	Description
Zeidler [9]	Found the impact of pipe rotation on drilling cutting transport.
Okrajni and Azar [12]	Studied the impact of inclination angles, Found the critical angles.
Brown, Bern [13]	Suggested the critical angles 50- 60^0 for cuttings transport
Peden, Ford [15]	Studied on impact of drill pipe rotation, inclination angles and cutting size**.**
Sifferman and Becker [16]	Analysed the impact of particle size and drill pipe rotation on cutting transport. Found the drill pipe rotation effective for smaller particles in range of angles close to horizontal line.
Bassal [17]	Investigated the effect of particle size (2-7mm)**.** Found the difficulty of smaller particles transport
Alfredo Sanchez, Azar [19]	Investigated the impact drill pipe rotation and particle size. Suggested dramatic effect of the drill pipe rotation in angles close to horizontal lines.
Yu et al. [20]	conducted a full scale experimental study of hole cleaning to develop the correlations formulas**.** Investigated the effects of mud rheology, inclination angle, pipe rotation, eccentricity.

2.4.2 Numerical Studies

2.4.2.1 CFD Studies

Many investigators have contributed to model the cuttings transport performance in the directional well drilling using numerical techniques. With the increase in computational power in the past decades several studies were carried out using Computational Fluid Dynamics (CFD) simulation approaches. Bilgesu, Ali [21] carried out CFD studies on influential parameters in cuttings transport using a TFM approach and found the significant role of the annular velocity in cleaning efficiency where an increase in flow rate can leads to higher cutting transport efficiency for the muds and wellbore used in their study. Later, Bilgesu, Mishra [22] simulated cuttings transportation in the annular section of a well bore using an Eulerian approach in CFD to determine the effects of different parameters such as cutting size, fluid velocity, rate of penetration, drill pipe rotation and inclination angles in deviated wells. They found more efficient hole cleaning for larger particle compared to smaller ones. Furthermore, they reported more problematic drilling cuttings transport to the surface while the inclination angle increases.

Wang, Li [23] carried out simulation using TFM approach to investigate the effect of drill pipe rotation and its influence on mud hydraulic in annulus space. They found that the rotation of the drill pipe reduces the volume fraction of solid phase in annular space and increases the solid phase migration rate, consequently promoting the borehole cleaning efficiency. Han, Hwang [24] studied hydraulic transport of drilling cuttings in vertical and inclined annuli with a rotating inner cylinder using TFM (Eulerian) approach in CFD program. They found that rotation of the inner cylinder generally improves the transport performance of particles and it is more noticeable at lower velocity rates. In addition, the impact of drill pipe rotation enhances the cuttings transport efficiency using non-Newtonian mud fluid (5 % Bentonite solutions) in compare with water. Osgouei, Ozbayoglu [25] studied the interactions between cuttings and drilling fluid in horizontal eccentric annulus using an Eulerian approach. They investigated the impact of the rate of penetration (ROP) and mud flow rate using a Newtonian fluid, i.e. water in an eccentric annulus. They noticed as the annular flow rate increases, the cuttings concentration reduces in annulus where increasing the ROP leads to more cuttings generation and consequently more cuttings accumulation at

bottomhole. Rooki, Ardejani [26] used TFM Eulerian approach via CFD software package (FLUENT) in their numerical simulation and expressed the impact of fluid properties and inclination angles on cuttings transport in annulus. They used a non-Newtonian pseudo-plastic fluid, i.e. foam to define the rheological properties of mud and found that the cuttings transport ratio increases with the increasing of the foam velocity in axial direction of annulus. Sun, Wang [27] used CFD models to investigate the effect of drill pipe rotation on cuttings transport in annulus. They carried out simulations for different inclination angles, flow rate and pipe rotation speeds and reported lower cuttings concentration near the drill pipe due to high tangential velocity under drill pipe rotation which improve the hole cleaning process. Later, Wang and Long [28] studied on unsteady model of cuttings transport for extended-reach well (ERW) and developed a three-layer unsteady cuttings transport model for all sections of ERW based on their CFD study to investigate the mechanisms of suspension, rolling and sliding of cuttings where the relative velocity between solid and liquid in suspension layer including the effect of drill pipe rotation are all considered. Their model can describe the impact of drill pipe rotation to some extend by modifying the fluid velocity of suspension layer and it can be used for the simulation of all sections and process in actual drilling condition. Mohammadzadeh, Hashemabadi [29] studied the effect of viscosity on cuttings transport by oil-based drilling fluid in wellbore. They carried out the CFD simulations using viscosity modifier to predict the cuttings transport in wellbore by considering various particle parameters. Simulations were conducted for inclined well to study the impact of density, shape, diameter and initial particle concentration where the rheology of the drilling fluid was expressed by Herschel-Bulkley non-Newtonian model. They found that higher fluid viscosity improves the cuttings transport capacity but its effect reduces in higher concentration. Similarly, higher particle density or larger particle size and higher initial particle concentration have an adverse impact on cuttings transport in wellbore. Amanna et al. [30] investigated cuttings transport behaviour in directional drilling using TFM approach in CFD. They studied the impact of mud flow rate, hole inclination, drill pipe rotation and cutting size in the annulus and found that the angles in range of $45 - 60^0$ can cause difficulty in drilling cuttings removal. They noticed that an increase in mud flow rate and drill pipe rotation mainly for larger particles can decrease the cutting concentration in the annular space. Yilmaz [31] implemented Eulerian-Lagrangian model in CFD framework to study the impact of fluid properties, wellbore

inclination angle, particles factors and drill string rotation on the cuttings transportation. Simulations carried out using non-Newtonian mud and compared with water, he realized that the yield point is the leading influential factor in mud. His model had few limitations; it was two-way coupled in which the effects of particle motion on flow field is neglected. The particle-particle interactions are neglected due to the assumption where the solids are not highly concentrated.

Table 2. Recent Numerical Models Studies on Hole Cleaning Process Using CFD Tools

Author	Description
Bilgesu, Ali [21]	Using TFM approach, found the significant role of the annular velocity in cleaning efficiency.
Bilgesu, Mishra [22]	Using an Eulerian approach, reported more problematic drilling cuttings transport while the inclination angle increases.
Wang, Li [23]	Using TFM approach, found rotation of the drill pipe reduces the volume fraction of solid phase in annular space.
Osgouei, Ozbayoglu [25]	Using an Eulerian approach, found as the annular flow rate increases, the cuttings concentration reduces.
Rooki, Ardejani [26]	Used TFM Eulerian approach, found influential impact of velocity in axial direction of annulus.
Sun, Wang [27]	Using CFD model to investigate the mechanisms of suspension, rolling and sliding of cuttings.
Amanna et al. [30]	Using TFM approach, found that an increase in mud flow rate and drill pipe rotation mainly for larger particles can decrease the cutting concentration.
Yilmaz [31]	Using Eulerian-Lagrangian model in CFD framework, found the yield point is the leading influential factor in mud.

2.4.2.2 CFD-DEM Studies

Tsuji, Tanaka [32] primarily proposed the CFD-DEM technique for the modelling purpose of particle-fluid flow system. Recently, the CFD-DEM approach is developed to simulate the cuttings transport in inclined wellbore where the motion of discrete particles is calculated by the Newton's second low of Motion in DEM and the fluid phase treated as an Eulerian continuum described by CFD method. The most recent approach to model the hole-cleaning process in oil wells is the four-way coupling CFD-DEM method. A few studies have been conducted using this approach addressing the common issues with the transport of rock fragments during the drilling operation [3, 33, 34]. For example, the effect of mud flow rate, inclination angle, well pressure, and raised temperature on the cuttings transport efficiency in a concentric annulus for an aerated mud drilling process are studied by Akhshik et al.[35] In another study they investigated the effect of drill pipe rotation on cuttings transport behaviour using CFD-DEM approach [3]. Their model has been established based on Osgouei et al. experimental data and their traditional CFD model [36, 37]. Simulations are carried out for different flow velocities, well inclination, and rate of penetration (ROP).They also developed a coupled CFD-DEM model to investigate the impact of the microscopic properties of particles, such as the sliding and rolling friction coefficients of particles-particles, particles-drill string and particles-wall contacts on the characteristics of cuttings transport mechanism near a horizontal deviated well [34]. They reported that sliding friction coefficient has a dominant role in comparison with the rolling friction factor. They set the grid size three times bigger than particle size (6.35 mm) where their model hydraulic diameter was only 78 mm. So, the number of grids was very limited across the annulus. Moreover, considering the turbulence of the carrier phase (fluid) the velocity gradient near the wall be significantly high and where the simulation results tend to be more influenced by grid size [38]. So, reliability of their numerical results is under question.

Parameter	Variable	Value	Units
Drill String Length	L	12	m
Angle of Inclination	0	00,20,40,60,80	deg
Pipe Diameter	D_p	48.26	mm
Hole Diameter	D_h	127	mm
Particle Diameter	d_p	6.35	mm
Particle Density Dry density	Pp	2619	Kg/m^3
Fluid Density	Pf	1012	Kg/m^3
Power Law Exponent	n	0.65	-
Consistency Factor	k	0.28	Pa.sn
Fluid Inlet Velocity	$u_{f,\ inlet}$	0.58(1.9), 0.72(2.39), 1.165(3.82)	m/s (ft/s)
Drill Pipe Rotation Speed	drillpipe	50	Rpm
Eccentricity Ratio	s	0.5	-

Table 3. Data used for CFD-DEM numerical solution[34].

Sun et al., investigated the critical deposition velocity of cuttings in an inclined slim-hole well using CFD-DEM method [39]. They conducted the simulations to study the cutting deposition phenomena at the bottom of the annular section which reduce drilling efficiency and increase the cost. For fully coupled CFD-DEM simulations the mesh size should not be less than the particles diameter, and according to their model the annulus structured grid size contradicts this basic rule [40], although their simulation results agrees with experiments. Their approach has been to use unresolved CFD – DEM framework where the numerical simulation has been performed in concentric annulus section with outer diameter of 44 mm, an inner diameter of 30 mm and length of 1.8 m. In this study, the hydraulic diameter of 14 mm has been divided into 60 x 6 meshes in cross section and the total number of grids is 29,000, with an average mesh dimension of 1.17 mm where the cuttings diameter is set as 2mm.

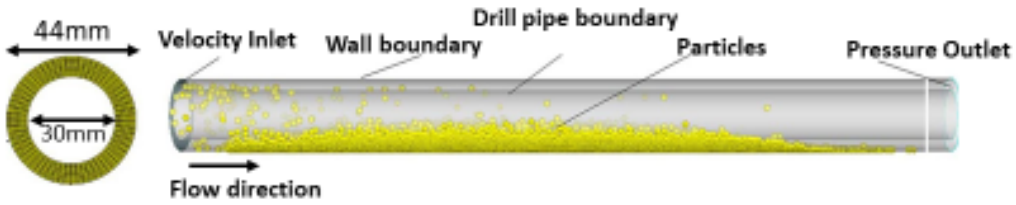

Fig. 17. Annulus flow field mesh used by shao et al. [39].

In recent years, effect of particle shape [33], non-spherical and large-sized cuttings [41], and four-looped shape drill pipe [42] on transportation mechanism in hole cleaning process have also been incorporated in some studies using CFD-DEM method.

Table 4. Recent Numerical Models on Hole Cleaning Process Using CFD-DEM Tools

Author	Description
Akhshik et al. [3]	Studied the impact of drill pipe rotation on cuttings concentration
Akhshik, Behzad [43]	Studied the effect of particle-particle contact on cleaning efficiency.
Akhshik et al. [35]	Investigated the impact of an aerated mud on cuttings transport efficiency.
Sun et al. [39]	Investigated the critical deposition velocity of cuttings in an inclined slim-hole well.
Akhshik et al. [33]	Studied the impact of particle shape on cuttings concertation.
Shao et al. [41]	Investigated the effect of non-spherical and large-sized cuttings on cleaning efficiency.
Yan et al. [42]	Studied four-looped shape drill pipe on cuttings concentration.

2.5 Summary of knowledge Gap Within the Literature

There has been numerous works reported in the literature on the well cleaning and its paramount importance on the drilling efficiency. Experimental investigations, particularly the work reported by Yu et al. [20] provides a comprehensive study on the cuttings concentration in simulated well conditions in laboratory, however in real well conditions, cuttings have different size distribution, depending on the geology and rock types and it has not been reported in their work. Furthermore, it is very challenging to create the real conditions of the well in the lab and changing experimental conditions are very costly and difficult. Hence the simulation work would have great potential in this respect. Computational Fluid Dynamics (CFD) has been used in majority of these studies, mainly in Eulerian framework, to assess the impact of different parameters on the cleaning efficiency of oil-well drilling operation. The shortcoming of the CFD models was the negligence of solid phase (cuttings) in the simulations. For example, Rooki et al. [23] developed a two-phase fluid model (TFM) to study the impact of mud properties on cuttings transport mechanism.

Since the cuttings are treated as continuous phase in Eulerian-Eulerian framework, their discrete characteristic information is not considered. Yilmaz [28] studied the impact of mud properties, well inclination angle, and pipe rotation speed on cuttings transport using Discrete Dense Particle Method (DDPM) two-way coupling approach. DDPM (Lagrangian-Eulerian) overcomes the TFM limitations and allows to track solid particles individually or in grouped (Parcels) according to Newton's second laws of motion. However, in DPM the particle-particle interaction is ignored and it's only valid for dilute system where the suspension layer of cuttings has enough time to settle. The more appropriate approach for this purpose is the use of fully coupled CFD with Discrete Element Method (DEM). However, use of this method requires careful consideration of particle-fluid interactions, particularly considering appropriate mesh configurations, which would be computationally very expensive for fully resolved systems. Hence approximations based on unresolved systems, where mesh size should be larger than particles, need careful attention, particularly for investigating the effect of particle-fluid interactions as well as the near wall conditions. However, most of the recent studies are suffering from lack of careful investigation of effect of cutting size and appropriate mesh configuration and refinement for particle-fluid interaction near the wall region which is significantly important for the transportation, sedimentation and suspension of cuttings. Moreover, a systematic study of the effect of mud rheology on cuttings transport in a fully coupled CFD-DEM is still lacking in the literature. This work focuses on optimisation of the hole-cleaning process using four-way coupled CFD-DEM approach. The impact of mud rheology on dynamics of cuttings is evaluated by varying the mud fluid rheological attributes. Also, the effects of cutting size, drill rotation, inclination angle, and mud flow rate on the hole cleaning efficiency are investigated. To improve the reliability of the simulations, special attention has been paid to the mesh refinement in the concern of CFD – DEM coupling.

Chapter 3

Methodology

3. Methodology

3.1 Introduction

The aim of this chapter is to present the governing equations and the numerical methods (CFD-DEM) used in predicting the cleaning efficiency in oil-well drilling process including the behaviour of two-phase flow (mud) of interest to this chapter. In this work, the fluid phase is calculated using Reynolds stress equation model (RSM) embodied in the commercial code FLUENT 19.2 which has the ability to predict complex dynamic flow phenomena. The flow solutions are coupled to a Lagrangian particle tracking – District element method (LPT-DEM) in EDEM 18 to predict the particle phase behaviour [44-62].

3.2 Fluid Phase Modelling

The basis for modelling a fluid flow comes from the mathematical statements of the fundamental laws of conservation including conservation of mass, momentum and energy. The derivations of these equations over a finite control volume for a Newtonian fluid is expressed as Navier-Stokes equations. The NS equations on a computational cell scale for the mass conservation can be written as:

$$\frac{\partial(\alpha\rho_f)}{\partial t} + \nabla.\left(\alpha\rho_f \boldsymbol{u_f}\right) = 0 \qquad (3.1)$$

Where $\boldsymbol{u_f}$ is the fluid velocity, ρ_f is the fluid density and α is the volume fraction of the fluid phase. The momentum conservation equation is expressed:

$$\frac{\partial(\alpha\rho_f \boldsymbol{u_f})}{\partial t} + \nabla.\left(\alpha\rho_f \boldsymbol{u_f}\boldsymbol{u_f}\right) = -\alpha\nabla p + \alpha\nabla.\tau - \boldsymbol{S}_f + \alpha\rho_f \boldsymbol{g} \qquad (3.2)$$

Where p is the fluid pressure, τ is the viscous stress tensor and $\boldsymbol{S}_f$ is the in the cell volume-averaged interaction force. For a particular computational cell, the source term $\boldsymbol{S}_f$ force is obtained:

$$\boldsymbol{S}_f = \frac{(\sum_{i=1}^{M} F_{f,i})}{V_{cell}} \tag{3.3}$$

Where M is the number of particle and V_{cell} is the volume of fluid in the computational cell.

In oil-well drilling operation, the mud displays non-Newtonian fluid properties. Oil industries usually apply Bingham and Ostwald (power law) models to express the non-Newtonian behaviour of the mud fluid. But in reality, the Herschel-Bulkley model shows better rheological performance of drilling fluids [63]. The dynamic viscosity in Herschel-Bulkley model is expressed:

$$\begin{cases} \mu = \mu_{yield} & if \ \ \dot{\gamma} < \left(\frac{\tau_0}{\mu_{yield}}\right) \\ \mu = \frac{\tau_0 + k(\dot{\gamma}^n - (\frac{\tau_0}{\mu_{yield}})^n)}{\dot{\gamma}} & if \ \dot{\gamma} \geq \left(\frac{\tau_0}{\mu_{yield}}\right) \end{cases} \tag{3.4}$$

Where k is the consistency factor, n is the power law exponent, μ_{yield} represents the yielding viscosity, τ_0 defines the yield stress threshold and $\dot{\gamma}$ expresses the strain rate magnitude.

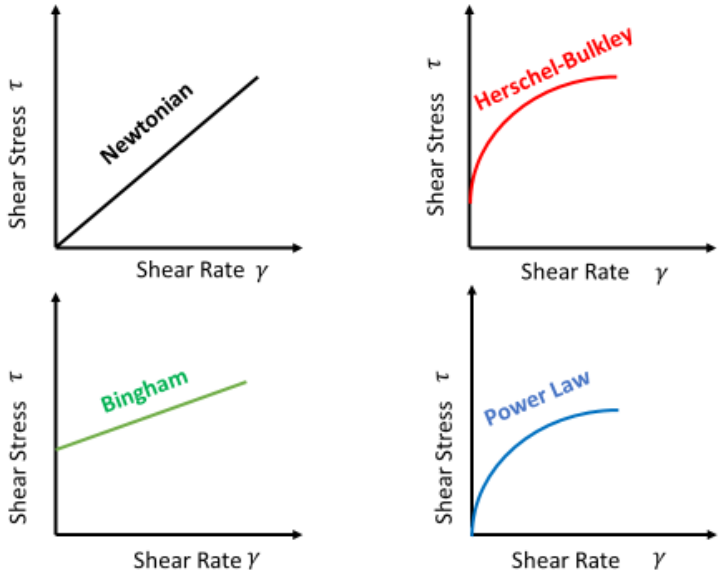

Fig. 18. Different Rheological Models.

3.3 Reynolds Stress Equation Model (RES)

Reynolds Stress equation Model (RES) is the most complete classical turbulent model in ANSYS FLUENT where the eddy-viscosity hypothesis is avoided and the individual components of the Reynolds stress tensor are directly computed by solving transport

equations for Reynolds stresses with an equation for the dissipation rate. In 3D flow model seven additional transport equations are solved in FLUENT.

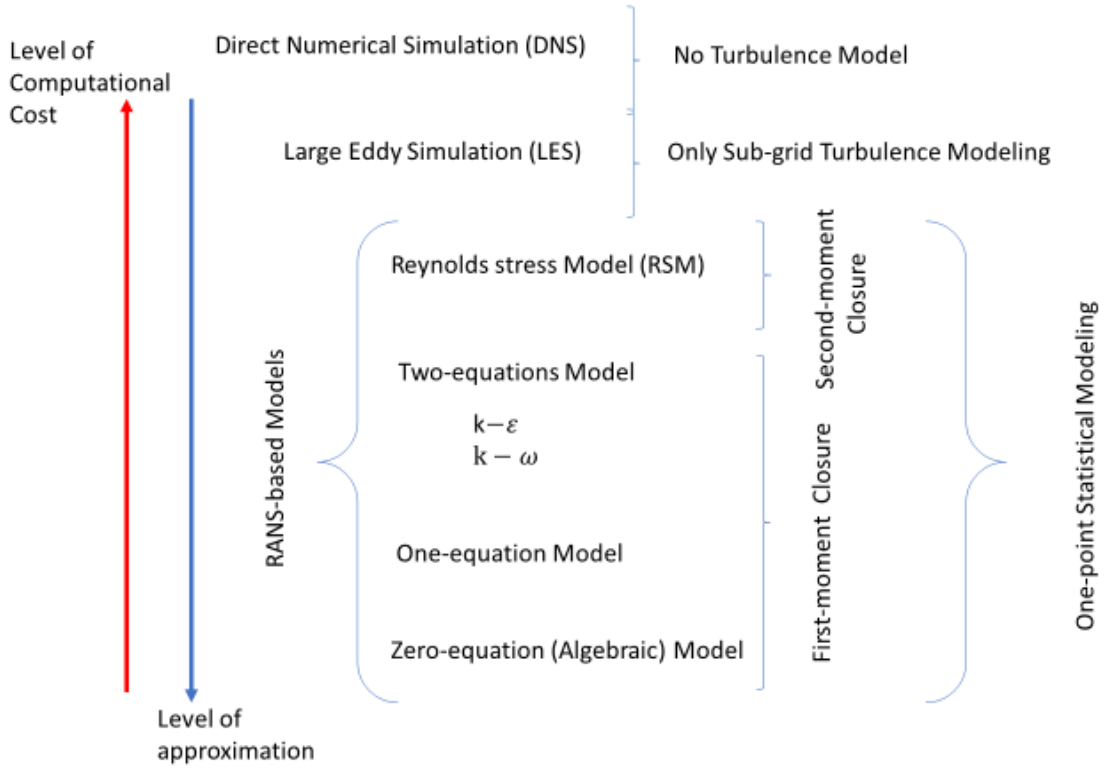

Fig. 19. Overview of different turbulent models [64].

Statistical (time-smoothed) models focus on the effects of turbulence on average properties of the flow. So, only mean time scales and turbulence length can be estimated where the structure or dynamics of eddies cannot be predicted [65]. For instance, all flow variables are individually decomposed into their smoothed and fluctuating components in these approaches:

$$\vec{u} = \bar{\vec{u}} + \vec{u}' \tag{3.5}$$

Where $(.')$ is the fluctuating part and $(\bar{.})$ is the time-smoothed value in Reynolds decomposition. For the fluid with constant density and viscosity the equation of motion can be derived from Navier-Stokes equations by changing the p, u and $\bar{\bar{\tau}}$ terms:

$$\nabla.\left(\rho_f \bar{\vec{u}}\right) = 0 \tag{3.6}$$

$$\rho_f \nabla.\left(\bar{\vec{u}}\,\bar{\vec{u}}\right) = -\nabla\bar{p} - \nabla.\bar{\bar{\tau}} + \rho_f \vec{g} \tag{3.7}$$

The shear tensor is consisted of turbulent momentum and viscous flux tensors:

$$\overrightarrow{\overrightarrow{\tau_f}} = \overrightarrow{\overrightarrow{\tau_f}}^{\nu} + \overrightarrow{\overrightarrow{\tau_f}}^{t} \quad (3.8)$$

Where

$$\overrightarrow{\overrightarrow{\tau_f}}^{\nu} = -\mu_f [\nabla\vec{u} + (\nabla\vec{u})'] \quad (3.9)$$

$$\overrightarrow{\overrightarrow{\tau_f}}^{t} = \rho_f \overline{\acute{u}\acute{u}} \quad (3.10)$$

The components of turbulent momentum flux are referred to as Reynolds stresses and the Reynolds stress tensor can be expressed as:

$$\overrightarrow{\overrightarrow{\tau_f}}^{t} = -\mu_f^t \nabla\vec{u} \quad (3.11)$$

The Reynolds stresses can be estimated from correlations of turbulent viscosity or solving equations of change for the Reynolds stresses where μ_f^t is the eddy (turbulent) viscosity. The statistical (time-smoothed) turbulence models are classified into turbulent viscosity (first-moment closure) models and Reynolds-stress models (second-moment closure) [66](Fig. **19**).

3.3.1 Reynolds Stress Equations

3.3.1.1 Transport Equations

The transport equations for Reynolds stresses can be written as:

$$\underbrace{\frac{\partial}{\partial t}(\rho\overline{\acute{u}_i\acute{u}_j})}_{\text{Local Time Derivative}} + \underbrace{\frac{\partial}{\partial x_k}(\rho u_k \overline{\acute{u}_i\acute{u}_j})}_{C_{ij\equiv}\ \text{Convection}} = -\underbrace{\frac{\partial}{\partial x_k}\left[\rho\overline{\acute{u}_i\acute{u}_j\acute{u}_k} + p(\delta_{kj}\acute{u}_i + \delta_{ki}\acute{u}_j)\right]}_{D_{T,ij} \equiv\ \text{Turbulent Diffusion}}$$

$$\underbrace{+\frac{\partial}{\partial x_k}\left[\mu\frac{\partial}{\partial x_k}\overline{(\acute{u_i}\acute{u_j})}\right.}_{D_{L,ij}\equiv\text{Molecular Diffusion}} \quad \underbrace{-\rho(\overline{\acute{u_i}\acute{u_j}}\frac{\partial u_j}{\partial x_k}+\overline{\acute{u_k}\acute{u_j}}\frac{\partial u_i}{\partial x_k}}_{P_{ij}\equiv\text{Stress Production}} \quad \underbrace{-\rho\beta(g_i\overline{\acute{u_j}\theta}+g_j\overline{\acute{u_i}\theta})}_{G_{ij}\equiv\text{Buoyancy Production}}$$

$$\underbrace{+\overline{p(\frac{\partial\acute{u_i}}{\partial x_j}+\frac{\partial\acute{u_i}}{\partial x_j})}}_{\emptyset_{ij}\equiv\text{Pressure Strain}} \quad - \quad \underbrace{2\mu\overline{\frac{\partial\acute{u_i}}{\partial x_k}\frac{\partial\acute{u_i}}{\partial x_k}}}_{\epsilon_{ij}\equiv\text{Dissipation}}$$

$$\underbrace{-2\rho\Omega_k(\overline{\acute{u_j}\acute{u_m}}\epsilon_{ikm}+\overline{\acute{u_i}\acute{u_m}}\epsilon_{jkm})}_{F_{ij}\equiv\text{Production by system Rotation}} \quad + \quad \underbrace{S_{user}}_{\text{User-Defined Source Term}} \tag{3.12}$$

The terms C_{ij} , $D_{L,ij}$ P_{ij} and F_{ij} do not required any modelling and terms $D_{T,ij}$, G_{ij}, $\emptyset_{ij}$ and ϵ_{ij} need to be modelled to solve the equations. These terms are described in next sections.

3.3.1.2 Turbulent Diffusive Transport

Turbulent diffusive transport equation can be modelled by the generalized gradient-diffusion model of Daly and Harlow formulation [67].

$$D_{T,ij} = C_s\frac{\partial}{\partial x_k}(\rho\frac{\overline{k\acute{u_k}\acute{u_l}}}{\epsilon}\frac{\partial\overline{\acute{u_i}\acute{u_j}}}{\partial x_l}) \tag{3.13}$$

In ANSYS FLUENT the above equation has been simplified to a scalar turbulent diffusivity:

$$D_{T,ij} = \frac{\partial}{\partial x_k}(\frac{\mu_t}{\sigma_k}\frac{\partial\overline{\acute{u_i}\acute{u_j}}}{\partial x_k}) \tag{3.14}$$

Where μ_t is the turbulent viscosity and the value of σ_k is equal to 0.82 by applying the generalized model. This value is different in $k-\varepsilon$ turbulent model ($\sigma_k = 1$).

3.3.1.3 Pressure-Strain Term in Turbulent Modelling

The following decomposition is applied for $\emptyset_{ij}$ modelling in ANSYS FLUENT:

$$\emptyset_{ij} = \emptyset_{ij,1} + \emptyset_{ij,2} + \emptyset_{ij,\omega} \tag{3.15}$$

Where $\emptyset_{ij,\omega}$ is the wall- reflection term, $\emptyset_{ij,1}$is the slow pressure-strain term and $\emptyset_{ij,2}$ is the rapid pressure-strain term.

The wall-reflection ($\emptyset_{ij,\omega}$) is responsible for the normal stresses near the wall and it tends to enhance the stresses parallel to the wall while damping the normal stress perpendicular to the wall. It is modelled as:

$$\emptyset_{ij,\omega} \equiv \acute{C}_1 \frac{\epsilon}{k}\left(\overline{\acute{u}_k\acute{u}_m} n_k n_m \delta_{ij} - \frac{3}{2}\overline{\acute{u}_i\acute{u}_k}\, n_k n_j - \frac{3}{2}\overline{\acute{u}_j\acute{u}_k}\, n_k n_i\right)\frac{C_l k^{3/2}}{\epsilon d}$$

$$+ \acute{C}_2\left(\emptyset_{km,2} n_k n_m \delta_{ij} - \frac{3}{2}\emptyset_{ki,2} n_k n_j - \frac{3}{2}\emptyset_{kj,2}\, n_k n_i\right)\frac{C_l k^{3/2}}{\epsilon d} \tag{3.16}$$

Where $\acute{C}_1$ is equal to 0.5 and $\acute{C}_2$ is equal to 0.3. Also, n_k is the $x_k$component of the unit normal to the wall and *d* is representing the normal distance to the wall.

And $C_l = C_\mu^{3/4}/k$ in which *k* is the Von Karman constant (0.4187) and C_μ is equal to 0.09.

The slow pressure-strain ($\emptyset_{ij,1}$) is modelled as:

$$\emptyset_{ij,1} \equiv -C_1 \rho \frac{\epsilon}{k}\left[\overline{\acute{u}_i\acute{u}_J} - \frac{2}{3}\delta_{ij} k\right] \tag{3.17}$$

Where $C_1 = 1.8$.

The rapid pressure-strain ($\emptyset_{ij,2}$) is modelled as:

$$\emptyset_{ij,2} \equiv -C_2\left[(P_{ij} + F_{ij} + \frac{5}{6} G_{ij} - C_{ij}) - \frac{2}{3}\delta_{ij}(P + \frac{5}{6} G - C)\right] \tag{3.18}$$

Where C_2 is equal to 0.6, $P = \frac{1}{2}P_{kk}$, $C = \frac{1}{2}C_{kk}$ and $G = \frac{1}{2}G_{kk}$.

3.3.1.4 Impact of Buoyancy on Turbulent Modelling

Due to buoyancy the production terms in ANSYS FLUENT are modelled as:

$$G_{ij} = \left(\overline{J_i U_j} + \overline{J_j U_I}\right) = -\beta\left(g_i \overline{U_j \theta} + g_i \overline{U_i \theta}\right) \quad (3.19)$$

$$\overline{U_i \theta} = \frac{\mu_t}{Pr_t}\left(\frac{\partial T}{\partial X_i}\right) \quad (3.20)$$

Where the value of the turbulent Prandtl number (Pr_t) for energy is equal to 0.85 and β is the coefficient of thermal expansion.

3.3.1.5 Kinetic Energy in Turbulent Modelling

The turbulence kinetic energy in ANSYS FLUENT is modelled using the Reynolds stress tensor:

$$k = \frac{1}{2}\overline{\acute{u}_i \acute{u}_i} \quad (3.21)$$

There is an option to solve a transport equation for the turbulence kinetic energy to determine the boundary condition for Reynolds stresses. So, the following equation is used for this purpose:

$$\frac{\partial}{\partial t}(\rho k) + \frac{\partial}{\partial x_i}(\rho k u_i) = \frac{\partial}{\partial x_j}\left[(\mu + \frac{\mu_t}{\sigma_k})\frac{\partial k}{\partial x_j}\right] + \frac{1}{2}(P_{ii} + G_{ii}) - \rho\epsilon(1 + 2M_t^2) + S_k \quad (3.22)$$

Where S_k is the user define term and σ_k is equal to 0.82.

3.3.1.6 Dissipation rate in Turbulent Modelling

The dissipation tensor ($\in_{ij}$) in ANSYS FLUENT is modelled as:

$$\in_{ij} = \frac{2}{3}\delta_{ij}(\rho\epsilon + Y_M) \quad (3.23)$$

Where the dilation dissipation ($Y_M = 2\,\rho\epsilon M_t^2$) term is an additional term to model the dissipation rate and the Mach number is defined as:

$$M_t = \sqrt{\frac{k}{a^2}} \quad (3.24)$$

Where $a(\equiv \sqrt{\gamma RT})$ is the speed of sound and the scalar dissipation rate (ϵ) is computed with similar transport equation in $k-\varepsilon$ model:

$$\frac{\partial}{\partial t}(\rho\epsilon)+\frac{\partial}{\partial x_i}(\rho\epsilon u_i)=\frac{\partial}{\partial x_j}\left[\left(\mu+\frac{\mu_t}{\sigma_\epsilon}\right)\frac{\partial_\in}{\partial x_j}\right]C_{\epsilon 1}\frac{1}{2}[P_{ii}+C_{\epsilon 3}G_{ii}]\frac{\epsilon}{k}-C_{\epsilon 2}\rho\frac{\in^2}{k}+S_\epsilon \qquad (3.25)$$

Where $C_{\epsilon 1}$ is equal to 1.44, $C_{\epsilon 2}$ is equal to 1.92, $C_{\epsilon 3}$ is a function of local flow direction relative to gravitational force (vector) and $\sigma_\epsilon$is equal to 1.

3.3.1.7 Turbulent Viscosity Modelling

In ANSYS FLUENT, the turbulent viscosity of RSM and $k-\varepsilon$ model is computed in the same way.

$$\mu_t=\rho C_\mu\frac{k^2}{\epsilon} \qquad (3.26)$$

Where C_μ is equal to 0.09.

3.3.2 Boundary Condition

3.3.2.1 Inlet Conditions

There are a number of methods available in ANSYS FLUENT for specifying the inlet boundary conditions. In most cases, based on artificial inflow information from experimental data or Reynolds average Navier-Stokes solutions. It is important to represent fully-developed turbulent at inlet. In Reynolds stress model, the turbulence specification method can be used to enter uniform constant values of velocity at inlet. For instance, the turbulence intensity value (*I*) at the core of a fully-developed flow can be estimated from the following formula derived from an experimental correlation for the pipe flows:

$$I\equiv\frac{\acute{U}}{U_{avg}}=0.16\,(ReD_H)^{-\frac{1}{8}} \qquad (3.27)$$

Where $\acute{U}$ is the velocity fluctuation, U_{avg} is the mean flow velocity and $D_H$is the hydraulic diameter. According to the equation (3.27) for high viscosity mud at a Reynolds number of 26000 at this study, the turbulence intensity will be 6% which implies a fully-developed flow at inlet. In this study, the velocity inlet and outlet boundary condition implemented where define the flow entering or exiting of the domain at certain velocity value. So, an uniform

fully-developed flow is considered at inlet to generate realistic turbulent eddies in the geometry.

3.3.2.2 wall boundary Conditions

The main reason wall boundary conditions are used is to bound the solid and fluid regions. In cases where the mesh is fine enough near the wall to capture the viscous sub layer, no-slip conditions can be implemented. The wall shear stress (τ_w) is derived from the stress-strain relationship:

$$z^+ = \frac{\rho z u_\tau}{\mu} \qquad (3.28)$$

Where z is the distance to the nearest wall, $z^+$is the dimensionless wall distance and u_τ is the shear velocity ($u_\tau = (\frac{\tau_w}{\rho})^{1/2}$) at the node closest to the wall.

In this study the inner pipe wall (drill pipe) is moving with angular velocity or stationary (fixed wall) at some cases. The cell zone adjacent to the wall is moving, so the relative to adjacent cell zone option specify the relative velocity. The rotational speed about a specified axis is defined by enabling the rotational speed option (6.2 rad/s). For the 3D geometry of this work, rotation axis origin is parallel to the vector from (x=0, y=0, z=0) to the (x=0, y=0, z=1) point specified under rotation-axis direction (Fig. 20).

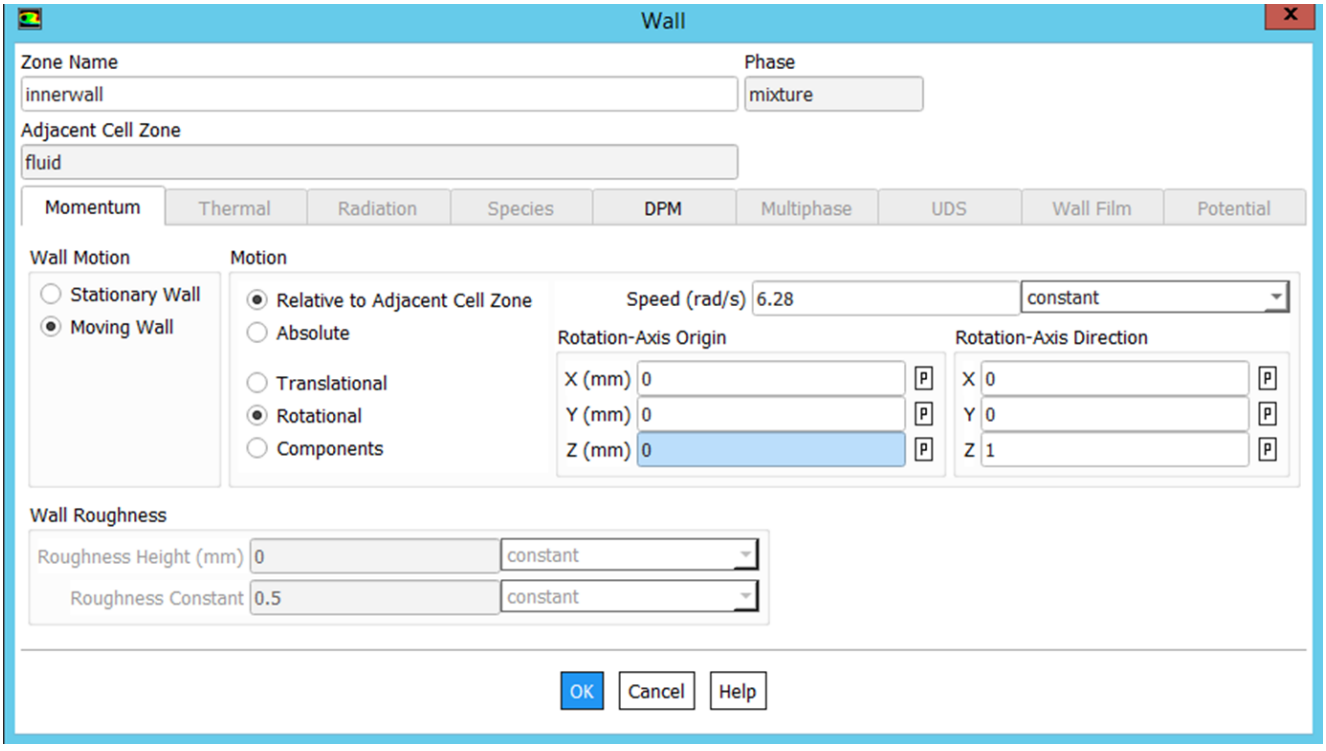

Fig. 20. Wall motion with rotational speed of 6.2 rad/s around the drill pipe in Z direction.

3.3.3 Solution Procedure

In ANSYS FLUENT (version 19.2), the governing integral equations are solved for the conservation of momentum, mass, energy and other scalars like turbulence based on control-volume technique. A finite volume method (FVM) is consisted of following rules:

1) A computational grid to divide the domain into discrete control volume.
2) Constructing algebraic equations for the discrete dependant variables (velocities, pressure) using integration of the governing equations on the individual control volumes.
3) Linearization of the discretised equations and solve the linear equations to obtain the updated values of the dependent variables.

Discretisation of the momentum and continuity and their solution using pressure-based solver are addressed in this section. The discrete values of the scalar are stored in the centre of the cell centre in FLUENT. 3-D discretisation is performed using an upwind scheme while the convection terms are interpolated from the cell centre values. For the numerical procedure, the second order central-differencing scheme is implemented which can cause stability problems. These problems are prevented using a deferred correction for the central-differencing scheme. The momentum equations are discretised using same scheme for a scalar transport equation. The PRESTO (PREssure Staggering Option) scheme is used to compute the face values of pressure from the cell values. The staggered (face) pressure is computed by using the discrete continuity balance for a staggered control volume. The face values of velocity are related to the stored values of velocity at the cell centres to discretise the continuity equation. Momentum-weighted averaging is performed to obtain the face value of velocity. The continuity equation is reformatted using Pressure-Implicit with Splitting of Operators (PISO) algorithm in order to achieve the velocity-pressure coupling. RSM is a time-averaging simulation, and therefore the governing equations need to be discretised in space and time. A bounded second order implicit time integration scheme is performed where the variables including the turbulence kinetic energy and dissipation rate are used. The secondary diffusion terms and velocities derivatives are computed and the values of a scalar at the cell faces constructed by using the gradient of the variables. The

gradients are used to discretise the diffusion and convection terms in conservation equations.

Discretisation of the transport equation is performed by pressure-based solver using an implicit approach. The overall time-discretisation error is specified by the method in which the solutions are advanced to next time step. The iterative approach is selected for the time-advancement scheme to minimize the errors. In this method, for a given time-step, all the equations are solved iteratively until the convergence is reached. A time-advancement solution requires a number of outer iterations (Fig. 21). In this scheme, the splitting errors are eliminated by considering the inter- equation couplings and non-linearity of the individual equations. Further information on the numerical solution approach and the mathematical model employed, may be found in ANSYS FLUENT 19.2 theory guide.

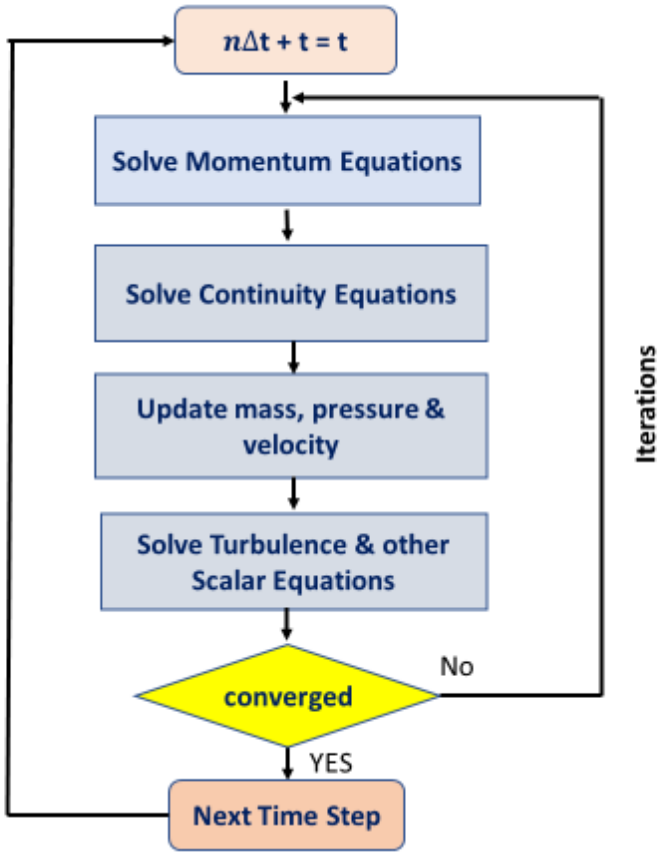

Fig. 21. Overview of the iterative time-advancement solution approach.

3.4 Particle Phase Modelling

The CFD code is coupled to the discrete element method (DEM) solutions (EDEM) software via coupling interface to predict the particle-fluid flows in this study. This section is a description of the fundamental basics of this coupled approach used in the present work

3.4.1 Governing Equations

The particles motion can be divided into two categories: 1) translational and 2) rotational where the particles are tracked explicitly by solving their trajectories in the computational domain for the translational and rotational accelerations. Particles velocities and positions are updated by integrating the accelerations over a time-step. The equation of translational motion for individual spherical particle (*i*) with the mass (*m*) can be written as:

$$m\frac{d\vec{v}}{dt} = \overrightarrow{F_g} + \overrightarrow{F_c} + \overrightarrow{F_{nc}} + \vec{F}^{f-p} \qquad (3.29)$$

Where (*V)* is the translational velocity of particle, $\overrightarrow{F_g}$ is the resultant gravitational force acting on the particle, $\vec{F}^{f-p}$ is the interaction force between fluid and particle, $\overrightarrow{F_{nc}}$ and $\overrightarrow{F_c}$ is the non-contact and contact forces between the particle and walls, respectively.

The equation of the rotational motion can be written as:

$$I\frac{\mathrm{d}\overrightarrow{\omega_p}}{\mathrm{d}t} = \vec{M} \qquad (3.30)$$

Where I is moment of inertia, ω_p is the angular velocity, $\vec{M} = -C_{fr}\left|\overrightarrow{F_c}\right|\omega_p$ is the resultant contact torque acting on the particle and C_{fr} is defined as the coefficient of rolling friction.

The fluid forces on the surface of particle are representing the fluid-particle interaction force where can be treated with two approaches: 1) Resolved-surface force 2) unresolved-surface force. In resolved CFD-DEM, where the fluid cell is smaller than particle size, the velocity and pressure field around the particle can be directly evaluated by integrating fluid tensor (pressure & shear) over the surface of particle. On the other hand, in unresolved CFD-DEM where the fluid cell is larger than particle size, an averaged force is employed to calculate the fluid-particle interaction force. In unresolved-surface approach, a linear decomposition of specific independent forces (e.g., drag force, lift (Magnus and Saffman) force, etc.)[40, 65, 68-78].

3.4.1.1 Fluid-Particle Interaction Force Decomposition

The fluid-particle interaction force is found by[66]:

$$\vec{f}^{f-p} = \vec{f}^{d} + \vec{f}^{u} + \vec{f}^{\nabla p} + \vec{f}^{\nabla \vec{\tau}} + \vec{f}^{l} \qquad (3.31)$$

Where $\vec{f}^{d}$ is the steady drag force, $\vec{f}^{u}$is the unsteady force (consists of unsteady drag force $\vec{f}^{ud}$ and added mass force $\vec{f}^{a}$), $\vec{f}^{\nabla p}$ is the pressure gradient force, $\vec{f}^{\nabla \vec{\tau}} = -V(\nabla.\vec{\tau}_f)$ is the viscous force (resultant of volume of particle V and $\nabla.\vec{\tau}_f$ deviatoric fluid shear stress tensor) and $\vec{f}^{l} = \vec{f}^{Saffman} + \vec{f}^{Magnus}$ is the lift force (consists of Saffman and Magnus forces).

The fluid-particle interaction force acting on particle is assessed at particle scale while the similar term in the fluid phase momentum equation, which is volumetric fluid-particle interaction force acting on the fluid, need to be calculated in each fluid cell. Feng and Yu reviewed different schemes, for unresolved CFD-DEM, the interaction force acting on individual particles is initially estimated in a fluid cell, further this force is counted on all particles to estimate the fluid-particle interaction force in the fluid cell [79].

3.4.2 Surface Force Decomposition

3.4.2.1 Steady Drag Force

Drag and pressure gradient forces play important role in fluid-particle flow. At very low Reynolds number $Re < 0.1$, the resultant force exerted on the surface of a single sphere particle can be written as:

$$\vec{f}^{f-p} = \vec{f}^{(n)} + \vec{f}^{(t)} = \left(V\nabla p + \pi\mu_f d\vec{w}\right) + 2\pi\mu_f d\vec{w} \qquad (3.32)$$

Where $\vec{f}^{(n)}$ is the normal force exerted by the surrounding fluid on a particle, $\vec{f}^{(t)}$ is the tangential force exerted by the surrounding fluid on a particle, $(V\nabla p)$ is the pressure gradient force for a fluid at rest, $(\pi\mu_f d\vec{w})$ is for drag force in which $\vec{w} = \vec{u} - \vec{v}$ is the relative velocity. The term $(2\pi\mu_f d\vec{w})$ represents the friction drag. The equation 3.32 can be rearranged into two parts of the force exerted by fluid at stationary condition and the force associated with the kinetic force. It can be written as:

$$\vec{f}^{f-p} = -V\nabla p + 3\pi\mu_f d\vec{w} = \vec{f}^{\nabla p} + \vec{f}^{d} \qquad (3.33)$$

Where the $\vec{f}^d$ is referred to Stokes-Einstein drag force based on characteristic area ($\vec{f}^d = C_d A^p K$), A^p is the projected area of the particle, K is the characteristic kinetic energy per unit and C_d is the drag coefficient.

The drag force is obtained from a relative function of Reynolds number:

$$C_d = \frac{24}{Re} \tag{3.34}$$

For the CFD-DEM problems, correlation formula has been developed to determine the drag force exerted on particle in the presence of other particles. The drag force in its dimensionless form can be written as:

$$\hat{f}^d(\varepsilon_f, Re) = \frac{\vec{f}^d(\varepsilon_f, Re)}{3\pi\mu_f \varepsilon_f d\vec{w}} \tag{3.35}$$

where $\vec{w} = \vec{u} - \vec{v}$, ε_f is the fluid volume fraction and the particle Re number is:

$$Re = \frac{\rho_f \varepsilon_f d|\vec{w}|}{\mu_f} \tag{3.36}$$

Based on experimental data or numerical studies, a number of correlations have been developed to evaluate the drag force. Gidaspow combined the Wen and Yu works[80] which suits the dilute system with the correlation of Ergun [81] which is valid for dense system and provided a general drag force for fluid-particle system [82]. In this method, the Wen and Yu is used for the volume fraction bigger than 0.8 and Ergun equation for volume fraction equal or less than 0.8.

$$\hat{f}^d(\varepsilon_f, Re) = \begin{cases} \dfrac{150(1-\varepsilon_f)}{18{\varepsilon_f}^2} + \dfrac{1.75}{18{\varepsilon_f}^2} Re & \varepsilon_f \le 0.8 \\ \dfrac{C_d}{24}\, Re{\varepsilon_f}^{-3.65} & \varepsilon_f > 0.8 \end{cases} \tag{3.37}$$

$$C_d = \begin{cases} \dfrac{24}{Re} + (1 + 0.15Re^{0.687}) & Re \le 1000 \\ 0.44 & Re > 1000 \end{cases} \tag{3.38}$$

3.4.2.2 Unsteady Drag Force

Unsteady drag force is occurred by the viscous layer near particles and the time required for penetration of generated momentum into the body of fluid boundary layer. Due to the

instability of the boundary layer, unsteady force exerted on particles. Unsteady drag force for an isolated spherical particle at low Reynolds numbers in a fluid at rest is given by:

$$\vec{f}^{ud} = \frac{3}{2}\, d^2\sqrt{\pi\rho_f\mu_f}\int_0^{\tau_p}\frac{d\vec{v}/dt}{\sqrt{\tau_p - t}}\, dt \qquad (3.39)$$

Where τ_p is the particle momentum response time and the above equation can be written for high Reynolds number by adding a correction factor (C_B) and replacing the velocity derivative to the relative velocity $(\vec{w})$.

$$\vec{f}^{ud} = \frac{3}{2}\, d^2\sqrt{\pi\rho_f\mu_f C_B}\int_0^{\tau_p}\frac{d\vec{w}/dt}{\sqrt{\tau_p - t}}\, dt \qquad (3.40)$$

3.4.2.3 Added Mass Force

An accelerated particle can affect on its surrounding fluid and causes the fluid displacement. The corresponding force is called added mass force and it is equivalent to adding a virtual mass to the sphere. The added mass force can be analytically derived as:

$$\vec{f}^{a} = \frac{\pi}{12}\, d^3\rho_f\frac{d\vec{w}}{dt} \qquad (3.41)$$

3.4.2.4 Lift Force

Lift force is related to the motion of fluid and particle and it causes by fluid shear stress and particle rotation. The Saffman lift force is shear-dependent and is due to fluid velocity gradient where the Magnus lift force is rotational-dependent and it causes by particle contact and rebound from a surface. The pressure difference on a non-rotating particle under non-uniform shear velocity field causes the Saffman force where can be calculated for an isolated particle at low Reynolds number by:

$$\vec{f}^{Saffman} = 1.61 d^2\sqrt{\rho_f\mu_f}\,|\vec{\omega}|^{-0.5}(\vec{w}\times\vec{\omega}) \qquad (3.42)$$

Where $(\vec{\omega} = \nabla\times\vec{u})$ is the curl of velocity vector. The pressure distribution around the particle due to the velocity difference between bottom and top of the particle causes the Magnus lift force and it given by:

$$\vec{f}^{Magnus} = \frac{1}{8}C_{IM}\vec{w}^2\pi d^2\rho_f\sqrt{\rho_f\mu_f}\,\frac{(\vec{w}\times\vec{\omega})}{|\vec{\omega}||\vec{w}|} \qquad (3.43)$$

C_{IM} is the Magnus lift coefficient and given by:

$$C_{IM} = d\frac{|\vec{\omega}_r|}{|\vec{w}|}\begin{cases}1 & Re \leq 1\\(0.178 + 0.822Re^{-0.522} & Re > 1\end{cases} \quad (3.44)$$

3.4.2.5 Rotational Drag

The drag on a rotating particle from the surrounding fluid and the rotational resistance due to the inertia o fluid is combined by rotational drag and is defined as:

$$\vec{M}^d = \pi d^3 \mu_f \vec{\omega}_r \quad (3.45)$$

Where the rotational Reynolds number is given by:

$$Re^{\vec{\omega}} = \frac{\rho_f |\vec{\omega}_r| \, d^2}{4\mu_f} \quad (3.46)$$

3.4.3 Fluid volume fraction

The fraction of fluid volume in fluid cell with volume of (V_{cell}) is called local volume fraction, porosity or void fraction. It is appeared in momentum and mass equations and used in fluid-particle force formulas. Therefore, this parameter affects the results of a CFD-DEM simulation and it can be estimated by the following equation [83]:

$$\varepsilon_f = 1 - \frac{1}{V_{cell}} \sum_{i=1}^{K_V} \varphi_i V_i \quad (3.32)$$

Where $\varphi_i \epsilon\ [0,1]$ is the volume fraction of the fluid cell of the particle *i* and it depends on the accuracy of the geometrical estimation of φ_i and number of the particle (K_V) in located in fluid cell. Exact geometrical 3D method is used to calculate the actual volume of each spherical particle in cell.

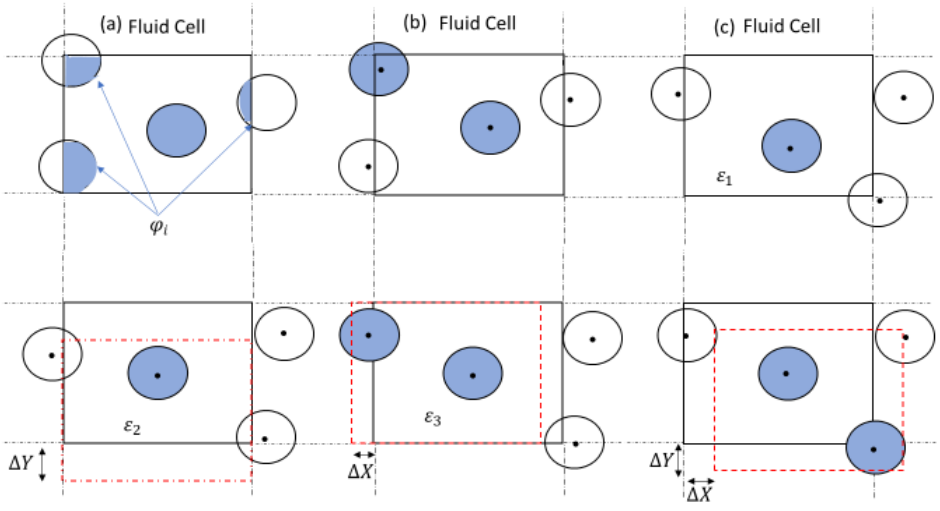

Fig. 22. Estimation of fluid volume fraction. (a) Exact method, (b) Particle centre method (PCM) and (c) improved PCM method. $\varepsilon_{avr} = (\varepsilon_1 + \varepsilon_2 + \varepsilon_3)/n$

The non-analytical approaches of simple particle centre method (PCM) and improved PCM are shown in Fig. 22. In the PCM method, all the volume of the particle is assumed to be in the computational cell if the centre of that particle is located inside the fluid cell (the volume of the fluid cell much bigger that total volume of particles). In improved PCM, the computational cell is adjusted in all direction to obtain the volume fraction by averaging all fluid cells volume fraction considering the number of displacements [44].

3.4.4 Particle-particle Interaction

The most computationally drastic part of DEM is locating pairs that are in close adjacency to each other. At every time step, collision detection is carried out since particles change their position in the following time step. A smaller time step requires more contact detection where the contact between particles needed to be checked with an efficient algorithm of specific set of criteria. In computational domain, Interaction between particles is only checked in the cell and neighbouring cells. Particle-particle interaction are modelled using DEM incorporating the contact model of Hertz-Mindlin to allow simulation of the Van der Waals forces with influence particle behaviour where the approach only considered the attractive forces within the contact area.[84].

The Hertz-Mindlin contact model is used to prevent particles from interpenetrating each other and to ensure that contact forces are transmitted between the different geometrical elements of in the simulation domain. The contact force is expressed with two components of normal and tangential shear with respect to the contact plane.

$$\vec{F}_c = \vec{F}_n + \vec{F}_t \tag{3.33}$$

Where F_c is the contact force, F_t and F_n is the tangential and normal components of contact force, respectively. The above equation can be expanded as:

$$\vec{F}_n = -k_n\delta_n - \gamma_n\vec{v}_n \tag{3.34}$$

$$\vec{F}_t = \begin{cases} -k_t\delta_t - \gamma_t\vec{v}_t & if\ |k_t\delta_t| < |k_t\delta_t|C_{fs}\delta_t \\ \frac{|k_t\delta_t|C_{fs}\delta_t}{|\delta_t|} & \end{cases} \tag{3.35}$$

Where $k_t\ and\ k_n$ are tangential and normal stiffness respectively, $v_t\ \ and\ v_n$ are the tangential and normal velocity respectively, $\gamma_n\ and\ \gamma_t$ are the damping coefficients to the normal δ_n and tangential δ_t overlap respectively and C_{fs} is the static friction.

The normal overlap can be defined as:

$$\delta_n = R_1 + R_2 - \|\vec{r}_1 - \vec{r}_2\| \tag{3.36}$$

And tangential overlap is defined as:

$$\delta_t = \int_t^{t+\Delta t} \vec{v}_t \, dt \tag{3.37}$$

The normal stiffness k_n and tangent stiffness k_t are functions of the Young's modulus and Poisson's ratio of the particle material respectively (EDEMSimulation.com).

3.4.5 Sequence of Calculation CFD-DEM Model

Diagram of the unresolved CFD-DEM model is illustrated in Fig. 23. The calculation process is beginning with the initialization of all components of simulation, CFD, DEM and coupling phases. Based on the position of the particles and mesh information, the fluid volume fraction in each computational cell is computed and transferred to the coupling phase. Henceforward, the fluid cell information (velocity, pressure and stress tensor) at current fluid time step is used to compute the fluid-particle interaction force ($\vec{f}^{f-p}$) acting on each particle. In addition, the volumetric fluid-particle interaction force in each fluid cell is calculated. The next step, is consisted of the iteration loop of the DEM where the data from coupling phase is used in the equation of the motion of each particle. The particle time step (Δt_p) for integrating the equation of motion of particles is repeated *m* times in the loop of DEM (here, the DEM time step is typically 10^{-2} times smaller than CFD time step). Following, after the DEM loop completion, the new information of all particles is computed at the next fluid time step. In CFD, all fluid phase equations are used to obtain volumetric fluid-particle interaction forces in each computational fluid cell. The CFD solver iterates over next time step until the solution converges in sequence of calculations. The fluid phase time step for the integrating the equation of motion is appointed stabilized by accurate Courant number. In order to stabilize the condition, the Courant number need to be less than 0.5 where the fluid time step falls in range of 10^{-5} to 10^{-2} second. But, different conditions are applied when solving equations of the motion of the coupled fluid-particle flow under impact of the interphase momentum exchange term. The new condition imposed upon fluid time step is specified by the fluid response time. The required time for the acceleration of fluid to react the particle velocity is defined by fluid response time and affected by the

particle drag force in the fluid computational cell. The fluid time step is chosen larger than the particle time step to avoid lagged integration of equations of motion of phases.

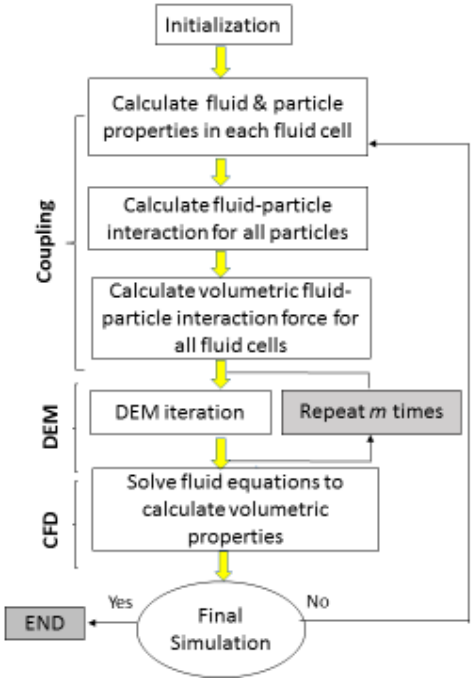

Fig. 23. Diagram of coupling in CFD-DEM model.

The maximum allowable time step in DEM is specified by based on Rayleigh analysis for the particle and falls in the range of 10^{-7} to 10^{-5} for numerical integration. In DEM, any disturbance cannot run from each particle further than its immediate neighbouring particles [85]. Based on the physical properties of the discrete phase, the speed of disturbance waves was estimated by Rayleigh time-step and given by:

$$T_R = \frac{\pi R(\frac{\rho}{G})^{\frac{1}{2}}}{0.16361\upsilon+0.8766} \qquad (3.38)$$

Where *R* is the particle radius, *G* is the shear modulus, ρ is the density and υ is Poisson's ratio for the particle. In this work, a time-step of 0.4 T_R was selected.

The selected time step for DEM is much smaller than the time step for the CFD in coupled CFD-DEM. In this work, the time step (Δt_p) for DEM is 5e-6 and the time step (Δt_f) for CFD is 5e-4. So, the time step in CFD is 100 times bigger than that in DEM. That means in each

coupling step, the system must perform 100 iterations (100 particle time steps) in the DEM section and 1 iteration (fluid time step) of the CFD.

Chapter 4

Mud Rheology and Hole Cleaning Efficiency

4. Mud Rheology and Hole Cleaning Efficiency

Hole cleaning operation and drilling cuttings removal from the annulus is only occurs with the essential presence of mud. Therefore, the mud properties, especially mud viscosity, have a significant impact on hole cleaning process.

The aim of this chapter is to describe the behaviour of different types of mud and their impact on drilling cutting transport. This chapter starts with the problem description and model set up for numerical simulation in FLUENT-EDEM platform using different mud properties followed by the results presentation, analysis of the discussion.

4.1 Model Description

The model is considered as a confined-length concentric annulus consisting of two cylindrical bodies. The interior cylinder represents the drill pipe which can rotate with a constant angular velocity around its axis. In drilling process, the length of the annulus can be thousands of meters in which the drill string is placed. The mud is injected through drill string all the way to the drill bit, exerted from the nozzles of the bit, flushing the cuttings from the bottomhole and transferring drill cuttings to the surface through the annulus. In order to reduce the computational cost, a section of the annulus with fully developed length is modelled [86].The length of the annulus (l) is selected in a way to ensure fully developed fluid flow within the annulus at different Reynolds number ($l > 20D$). A concentric annulus with outer diameter of 120 mm and inner diameter of 50 mm with 1500 mm length is modelled, as presented in Fig. 24.

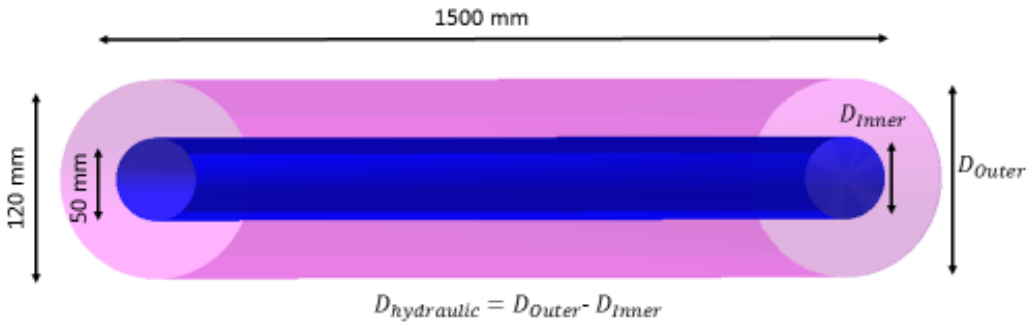

Fig. 24. Configuration of problem.

A two-phase flow (particle-fluid) with uniform bulk velocity and uniform cutting velocities enters the annulus from one end and exits from the other end. Boundary conditions for the fluid were considered as the inlet flow velocity and the ambient pressure outlet (Fig. 25). The process is isothermal and the wall boundary (contact between particles and walls) were treated as no-slip condition. Particles were generated at the inlet with the same velocity as the inlet fluid.

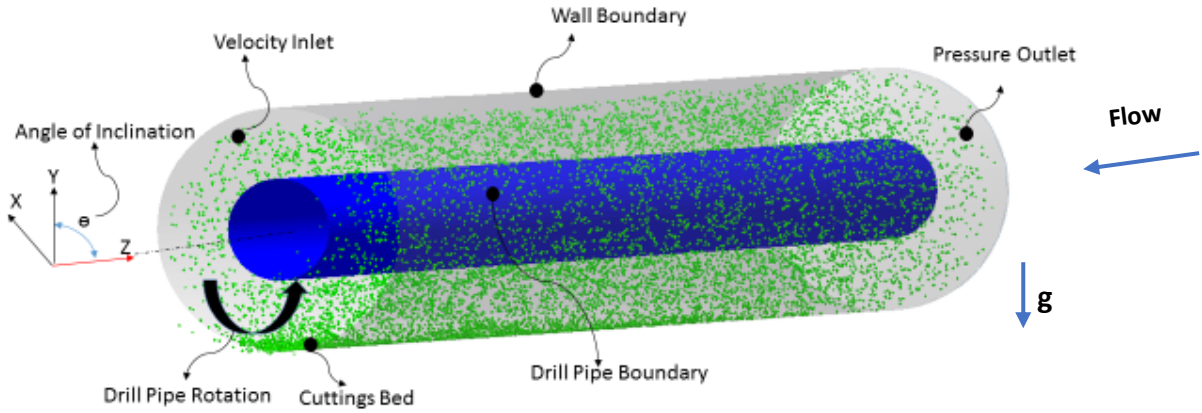

Fig. 25. Geometry domain and boundary conditions.

In this study, 10,000 particles per second are injected into the system where the particle density is 2600 kg/m^3. The particle mass flow rate is calculated knowing the volume, density, and number of particles in simulations. The volume fraction of drilling cuttings at the annulus inlet can be obtained by dividing the volumetric flow rate of cuttings over the total annulus volume. The cuttings mass flow rate of 0.037 kg/s is calculated based on the representative Rate of Penetration (ROP) of 4.57 m/h or 15 ft/h, which results in cutting generation, equivalent to injection of 10,000 particles per second into the annulus. The rheological properties, geometrical characteristic, and simulation input parameters in this study are shown in **Table. 5**.

Table. 5. simulation input parameters

Parameter	Tomren et al 1986	Simulation Data	Units
Drill string length	12	1.5	m
Angle of inclination	0,20,40,60,80	0,45,90	deg
Wellbore (hole) diameter	127	120 (4.75")	mm
Drill pipe diameter	48.26	50	mm
Drill pipe rotation (rpm)	0,50	60,120	rpm
Eccentricity ratio	0.5	0	-
Fluid behaviour index (n)	0.65	0.65	-
Consistency index (k)	0.28	0.28	$Pa.s^n$
Fluid inlet velocity	0.58,0.72,0.87,1.1	0.5, 1, 1.5	m/s
Fluid density	1018	1018	Kg/m^3
Particle density	2619	2600	Kg/m^3
Cutting diameter (average)	6.35	0.8-1.1 (1) , 1.3-1.5 (1.4)	mm

4.2 Mesh information

The discretisation of the computational domain is preformed based on the fluid phase calculations. It should be also noted that for the unresolved CFD-DEM modelling, the grid size must be larger than the largest particle in the domain. To obtain the optimum mesh arrangement with minimum number of computational cells, a mesh sensitivity study is usually carried prior to running the main simulations. In this work, the results obtained using different number of mesh elements are presented in Fig. 26. In this figure, the steady state cuttings concentration is plotted against the mesh number. It can be seen that cuttings concentration decreases slightly as the mesh number is increased. This could be due to the reason that smaller mesh size (due to higher number of mesh number) could result in more accurate consideration of fluid-particle interactions leading to more particles being transported by fluid in annulus. It can be also observed that the change in cuttings

concentration from 450,000 to 569,710 mesh cells, the reduction in cuttings concentration is very small. It was not possible to increase the mesh number beyond 569,710 as this would result in mesh sizes being equal or smaller than particle size which is not compatible with the unresolved CFD-DEM principles.

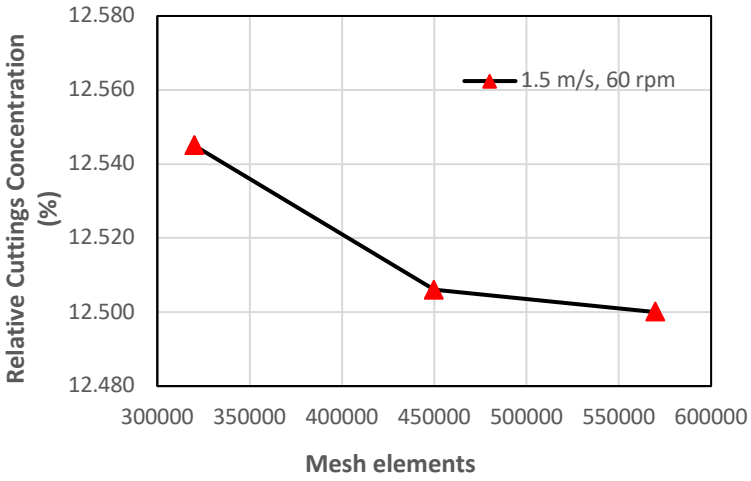

Fig. 26. Mesh independency study; mud annular velocity 1.5 m/s.

Based on the results in Fig. 26 with respect to particle size and grid size limitation, the most suitable mesh was chosen. The computational cells on the cross section of the annulus are presented in Fig. 27 where a computational domain with 629,132 nodes and 569,710 cells were selected with refined mesh near the walls.

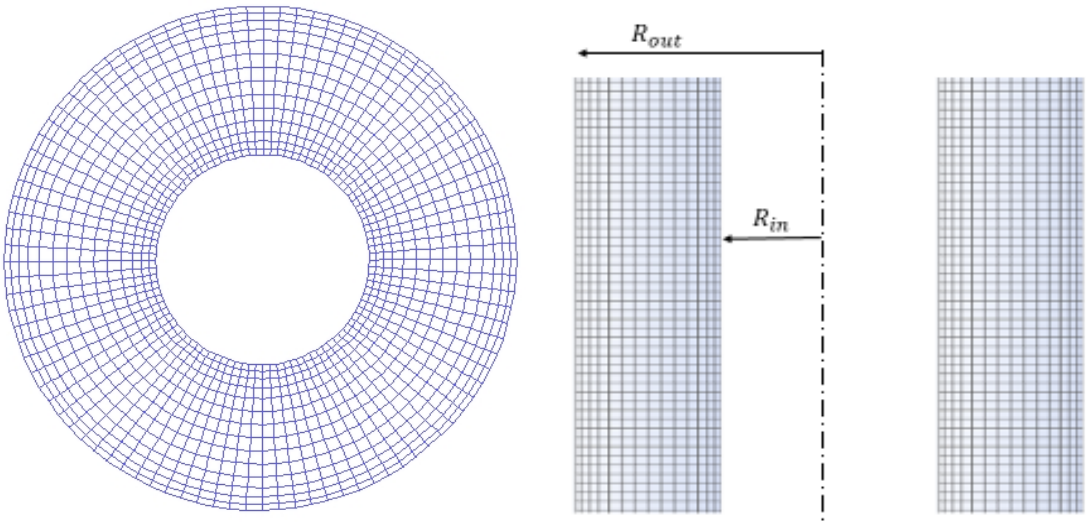

Fig. 27. Computational grid on the cross section of the concentric annuls.

4.3 Mud properties

Simulations were carried out for fully developed fluid-solid phase flow in a vertical (0^0) and deviated annuli ($45°\& 90°$) where muds with different rheological properties, i.e. low, intermediate, and high viscosities, were used. The mud properties shown in Table. 6 were selected based on the experimental studies of Tomren at al. [14] and Okranji and azar [87]. The mud was considered as Hershel-Bulkley non-Newtonian fluid as classified in the methodology section.

Table. 6. Rheological Properties of Mud Studied

Drilling Fluid	Low-Viscosity mud (LVM)	Intermediate-Viscosity mud (IVM)	High-Viscosity mud (HVM)
Apparent Viscosity (Pa.s)	0.004	0.013	0.028
Plastic Viscosity (Pa.s)	0.003	0.009	0.019
Yield Point (Pa)	0.5	4	8
Mud Re	9000-26000	3000-8000	4000-12000
Particle Re	1 < 89-143 < 1000	1 < 13-18 < 1000	1 < 3-6 < 1000
Slip Velocity (m/s)	0.25-0.4	0.12-0.16	0.05-0.12
Particle Stokes's number	1 - 0.5	0.15-0.45	0.07-0.2

4.3.1 Mud Viscosity

The rheological behaviour of mud plays an important role in efficient drilling cuttings transport [88]. Mud viscosity is independent of shear rate in Newtonian mud, while it is a function of the shear rate in non-Newtonian muds where the shear stress is not linearly related to the shear rate. The slope of the shear stress versus shear graph is called the apparent viscosity. For shear thinning mud the apparent viscosity decreases with increasing shear rate, i.e. the harder the mud is sheared the less viscous it gets [89]. The power law non-Newtonian model is the model which is valid for fluids with zero shear stress when the strain rate is zero. Whereas, Bingham plastic model suggests a non-zero shear stress (τ_0) when the shear rate is zero. As mentioned in Chapter 3, Herschel-Bulkley model combines the effects of Bingham and Power-law behaviour in a non-Newtonian mud. Therefore, apparent viscosity and other rheological properties of non-Newtonian mud, including the

plastic- viscosity and yield point, are determined in the oil industry using the Herschel-Bulkley rheological model. All the rheological properties are obtained from the rheometer or viscometer reading i.e. R_{300} and R_{600} [90]. Bingham plastic model is expressed using the following equations:

$$\tau = PV\left(\frac{\gamma}{300}\right) + \tau_0 \tag{4.1}$$

$$PV = R_{600} - R_{300} \tag{4.2}$$

$$\mu_a = \frac{R_{600}}{2} \tag{4.3}$$

Where τ is the shear stress, γ is the shear rate, *PV* is the plastic viscosity, τ_0 is the yield point, and μ_a is the apparent viscosity. R_{600} and R_{300} are the viscometer reading at 600 rpm, 300 rpm respectively.

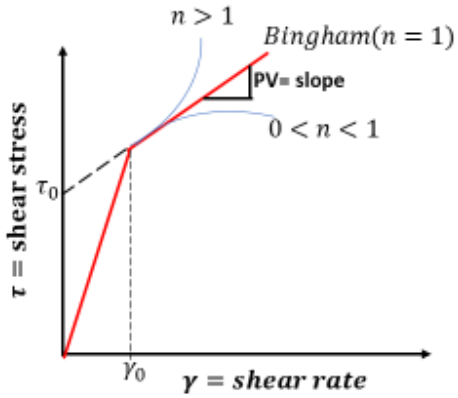

Fig. 28. Variation of shearing stress with rate of shearing strain.

Herschel-Buckley model is expressed as:

$$\begin{cases} \tau = \tau_0 + k\gamma^n & \tau > \tau_0 \\ \gamma = 0 & \tau < \tau_0 \end{cases} \tag{4.4}$$

Where *k* is the consistency factor and *n* is the power low index. If *n* equals to 1, the mud follows the Bingham model. If *n* is larger than one, the mud behaves as a shear-ticking fluid and if n is smaller than one, the mud is a shear-thinning fluid. In this work, the simulations are carried out using Herschel-Buckley model with shear-thinning behaviour for three levels of mud viscosity i.e. high viscosity mud (HVM), intermediate viscosity mud (IVM) and low viscosity mud (LVM).

4.4 Steady-State Condition

A typical behaviour of number of particles in annulus as a function of simulation time is plotted and shown in Fig. **29**. In this figure, the results are showed for a horizontal wellbore with high viscosity mud (HVM), annular velocity of 1.5 m/s with an average particle size of 1.4 mm, while the pipe is rotated at 60 rpm. It can be seen that there is a linear correlation between number of particles and time in the beginning which is similar to the rate of particle injection (10,000 particle/second). After point about 0.8 second, the number of particles in annulus starts to level off and reaches the steady state for this particular case at around 4.3 second where a constant value is achieved for number of particles in annulus.

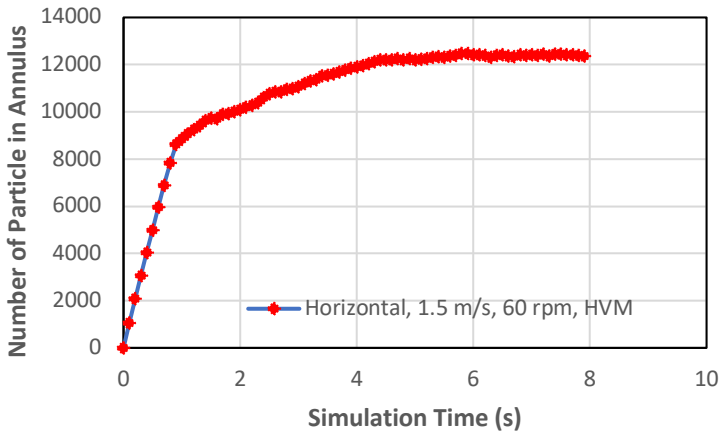

Fig. 29. Number of particles remained in annulus in horizontal wellbore,1.5 m/s, 60 rpm, d_p=1.4 mm, HVM.

To reach the steady-state condition, all simulations were carried out until the cutting concentration was statistically reached nearly to a constant value. The impact of mud flow rate, yield stress, inclination angle, and drill rotation speed on hole-cleaning efficiency is investigated in this study.

4.5 Relative Cuttings Concentration

Sifferman et al., defined the cuttings transport efficiency as the ratio of the average cuttings transport velocity to the average fluid velocity [91]. In addition, previously works reported,

full scale drill strings have been considered while in the simulations in this work a small fraction of the drill string has been simulated so that the computations could be performed in a reasonable time scale. In this study, a different concept is defined to investigate the cuttings transport capacity of mud. The ratio of the number of remaining particles in annulus (until reaching steady state) and the total number of particles injected into annulus is defined as relative cuttings concentration or in other words:

$$\mathrm{RCC} = \frac{\text{Number of particles remained in annulus}}{\text{Total number of injected particles}} \qquad (4.5)$$

A Lower RCC means there is lower cuttings concentration in the annulus and better transport performance. In this study, RCC needs to be distinguished from the absolute cuttings concentration and it is the ratio of the volume of remaining particles to the total volume of the annulus at steady state.

4.6 CFD-DEM Model Performance against Experimental Correlation

In this section, the results obtained by the CFD-DEM model is compared with cuttings concentration predicted by Yu et al. correlation formulae (Chapter 2), where the absolute cutting concentration is explicitly related to two dimensionless parameters, F_r *and* T_a [20].

$$\mathrm{C_c} = 0.062\mathrm{F_r^{-1.31}Re^{0.157}\ T_r^{0.165}Drp^{0.045}\tanh(1 + 0.0043T_a)} \qquad (4.6)$$

$$\begin{cases} \mathrm{F_r} = \dfrac{\mathrm{V_a}}{\sqrt{\mathrm{g(D-d)}}} \\ \mathrm{T_a} = \dfrac{\rho_f * \Omega * (\mathrm{D_{hyd}}^2)}{\mu} \end{cases} \qquad (4.7)$$

The cuttings concentration is depicted in Fig. 30 and Fig. 31 for selected mud velocities (0.5 m/s, 1 m/s and 1.5 m/s) and 60 rpm drill rotational speed (6.2 rad/s). The experimental correlation is obtained based on real drilling tests, where cuttings could be produced with a wide size distribution (in reality there are large cuttings in cm range) which this was not considered in the correlation, whereas in the CFD-DEM simulations, the particles are injected with a narrow size distribution and somewhat small (mm range) due to the limitation of mesh size for conventional DEM-CFD (unresolved). As it will also be shown in

Chapter 5, cutting concentration will reduce with decreasing the size, and sedimentation and poor transport could be expected for larger cuttings (cm range), hence, one could except that the cuttings concentration predicted by the correlation formulae would be much higher than that of the CFD-DEM simulations. Furthermore, in real tests near full scale drill strings has been considered while in the simulation in this work a small fraction of the drill string has been simulated so that the computations could be performed in a reasonable time scale. What is more important here is that for both approaches the cuttings concentration varies with a similar trend against the mud velocity and mud rheology.

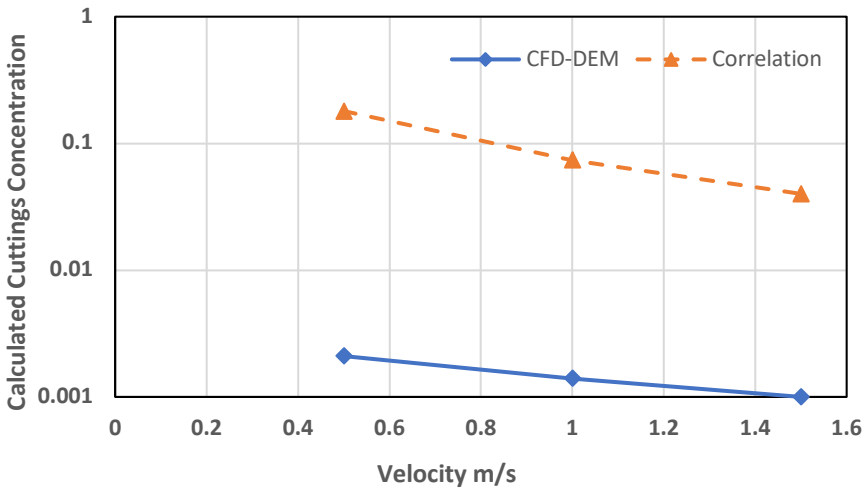

Fig. 30. Comparison between Correlation data and CFD-DEM model for HVM.

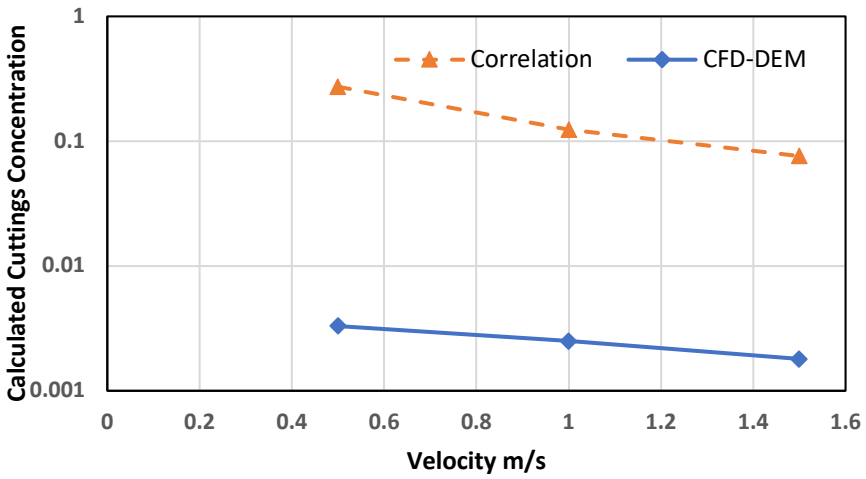

Fig. 31. Comparison between Correlation data and CFD-DEM model for LVM.

4.7 Cuttings Volume Fraction Distribution and Mud Velocity

The cuttings distribution across the annulus is an important factor in the well cleaning process. To obtain the particles volume fraction the annulus was divided into longitudinal bins with equal width across the radius Fig. 32 and the volume of particles within each layer was calculated and divided by the total volume of that layer.

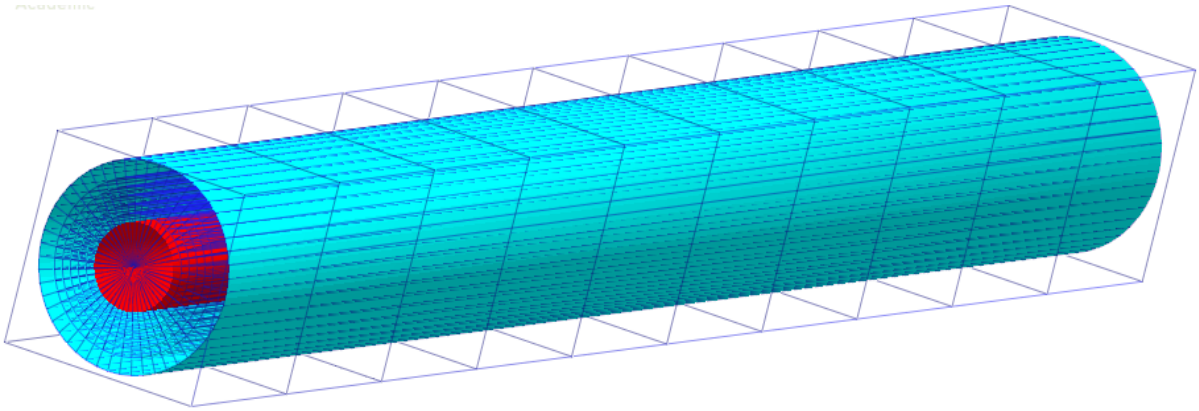

Fig. 32. Annulus divided into longitudinal bins with equal width across the radius of horizontal wellbore.

The volume fraction of cuttings across the radial direction of the vertical annulus is depicted in Fig. 33. It is observed that the volume fraction of cuttings near the walls are higher than the middle of the annulus, illustrating an arc-shape distribution of cuttings along the radial direction of annulus. Due to the no-slip condition near the walls, the highest level of shear rate occurs at the boundaries of the annulus. The high variation of velocity near the wall and shear thinning behaviour of mud fluid both leads to a more viscous mud in the middle of the annulus with a higher capacity of carrying cuttings compared to other. Therefore, the cuttings concentration decreases more easily in the middle of the annulus. In Fig. 34, cuttings distribution colour coded with respect to their stream wise velocity is plotted. It can be seen that most particles in the annulus have gain nearly fluid velocity, except those near the wall due to the aforementioned reason.

Fig. 35 shows the cuttings volume fraction in radial direction of the horizontal wellbore. Here, the direction of the gravity force has changed in comparison with the vertical annulus. High concentration of cuttings near the lower wall of the annulus is clearly observed in the

figure as a result of gravitational force. Hence, higher annular mud velocity is required in order to enhance the cleaning efficiency in directional drilling process [3, 14, 92, 93].

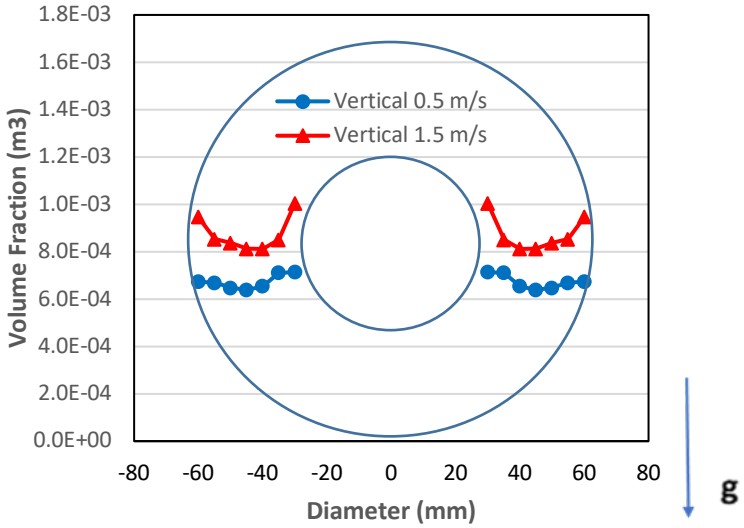

Fig. 33. Volume fraction of cuttings in radial direction of vertical annulus for V=0.5 m/s, $\boldsymbol{d_p}$=1mm, HVM and vertical annulus for V= 1.5 m/s, $\boldsymbol{d_p}$= 1.4 mm, HVM.

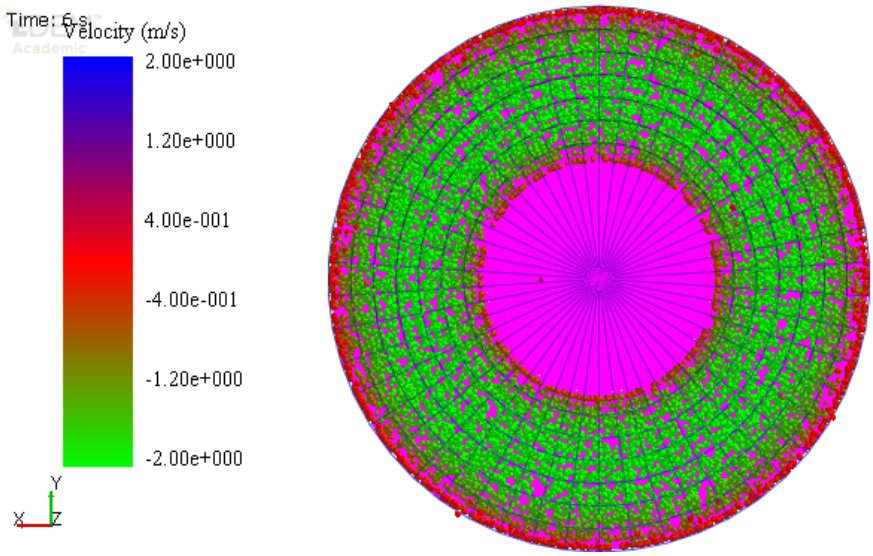

Fig. 34. Cuttings distribution in vertical annulus at V= 1.5 m/s; Background pink colour is for illustration only.

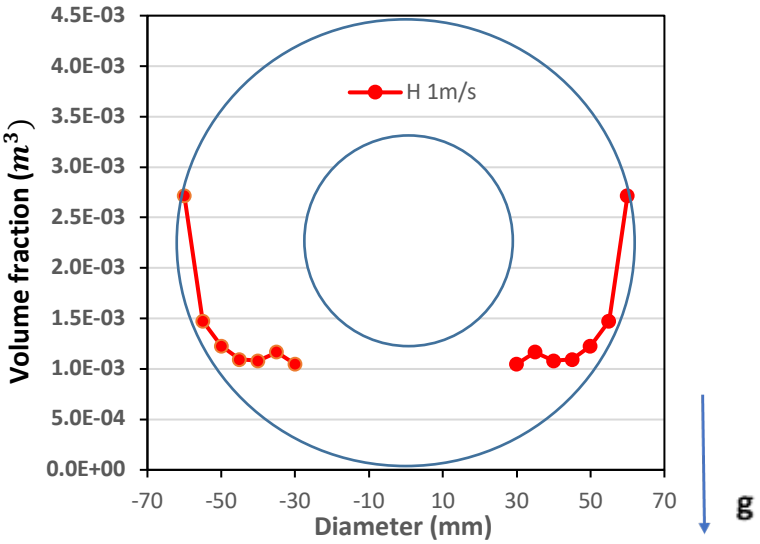

Fig. 35. Volume fraction of cuttings in radial direction of horizontal annulus for annular velocity of 1 m/s, HVM

The cuttings distribution of horizontal wellbore is depicted in Fig. 35. This figure clarifies the tendency of particles for accumulation near the lower wall of the horizontal annulus, particularly at lower velocities. Thus, fewer cuttings are influenced by the motion of the fluid. Consequently, the drag forces decrease and slip velocity increases along the annulus. With slip velocity increase, cuttings transport efficiency reduces in the horizontal annulus. Generally, in the case of the vertical wellbore, the axial component of the slip velocity is dominated. On the other hand, in the horizontal wellbore, the radial component of slip velocity reaches the maximum value and the axial component is minimum. It can be concluded that all the parameters with diminishing impact on the particle slip velocity improve the cuttings transport efficiency. In the case of an inclined annulus, similarly, the high radial component of particle's slip velocity causes cuttings bed formation by pushing the particle toward the lower wall of the annulus.

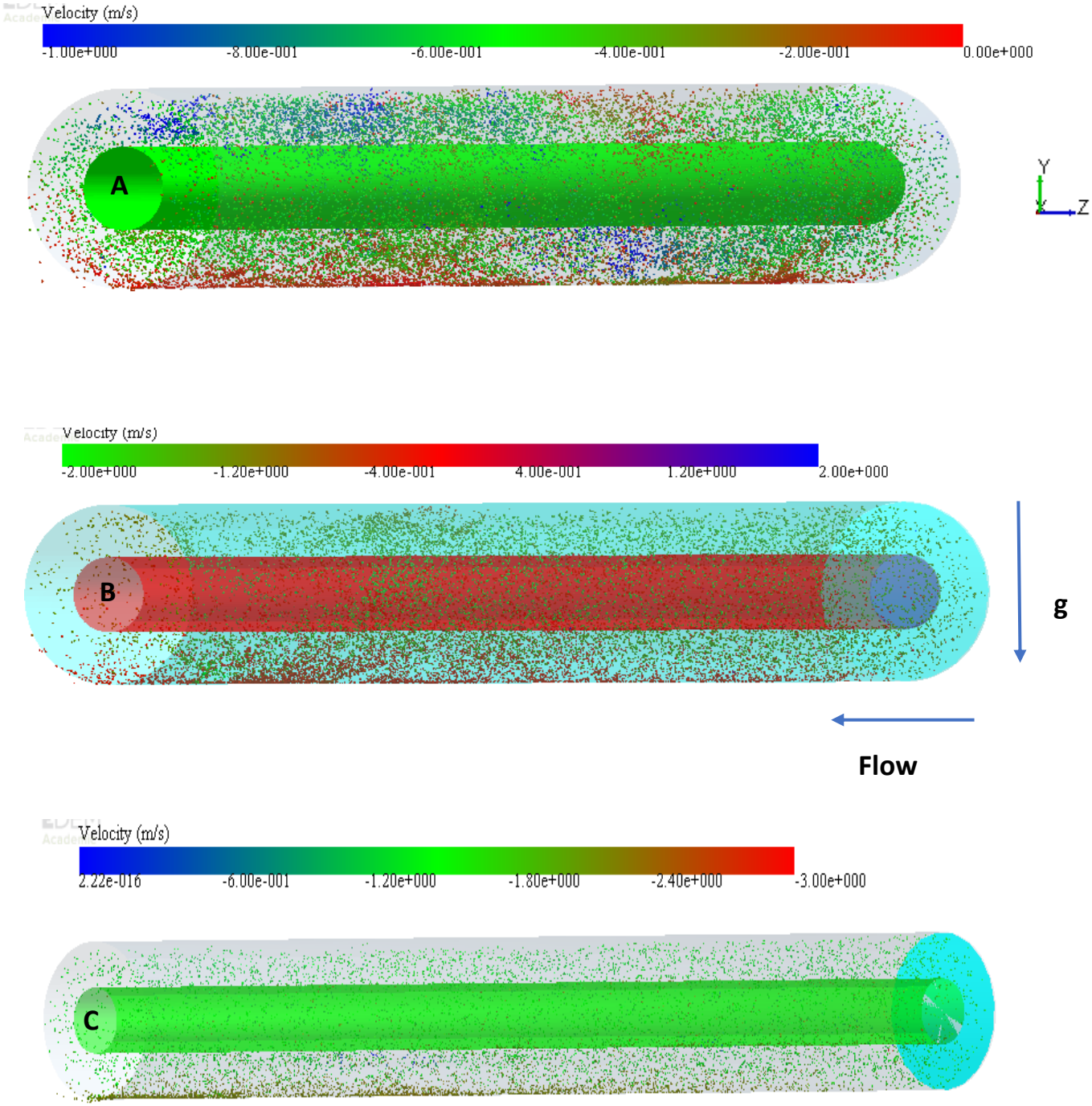

Fig. 36. Cuttings deposition at lower wall of horizontal annulus; (A) V=0.5m/s, (B) V=1 m/s and (C) V= 1.5 m/s.

4.8 Effects of Yield Value and Annular Velocity

As mentioned before, the mud is a non-Newtonian fluid that its rheological behaviour obeys the Herschel-Buckley viscosity model. In this model, presented in Equation (3.4), the yield point is the threshold below which the mud behaves like a solid. Yield stress, therefore, is an important parameter affecting the rheological behaviour of the mud within the annulus. To study the effect of yield point on cleaning performance in the drilling process, three types of mud, i.e. high viscosity mud (HVM), intermediate viscosity mud (IVM) and low viscosity mud (LVM) are modelled representing the high, medium, and low yield stress values, respectively.

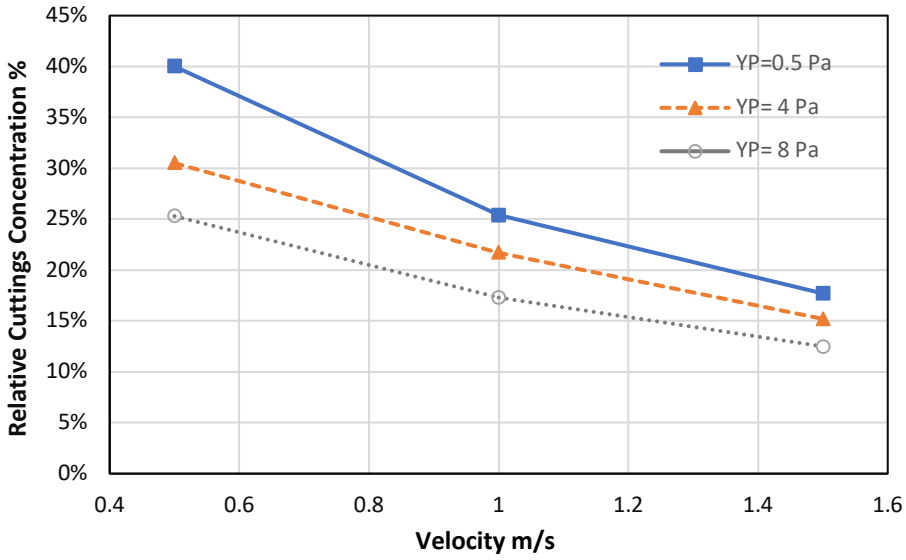

Fig. 37. Effect of yield on cleaning efficiency at different annular velocities for horizontal annulus

The effect of yield value on RCC at different annular velocities for horizontal annulus is presented in Fig. 37. As shown, increasing the yield value has resulted a reduction in RCC in annulus at all range of velocities. By increasing velocity from 0.5 to 1.5 m/s, RCC decreased 50.6 % for higher yield point (YP= 8 Pa), 50% for intermediate yield point (YP= 4 Pa) and 55% for lower yield point (YP=0.5). Also, by increasing yield value from 0.5 to 8 Pa, at constant velocity of 0.5 m/s, RCC decreases by 15% and at constant velocity of 1.5 m/s, RCC decreases 5.5%. It can be derived that the impact of rheology on cuttings transport is less at higher flow rates.

The effect of yield value on RCC at different annular velocities for inclined 45° annulus is presented in Fig. 38. As shown, increasing the yield value has resulted a reduction in RCC in annulus at all range of velocities. By increasing velocity from 0.5 to 1.5 m/s, RCC decreased 60% for higher yield point (YP= 8 Pa), 57% for intermediate yield point (YP= 4 Pa) and 62% for lower yield point (YP= 0.5 Pa). In addition, by increasing yield value from 0.5 to 8 Pa, at low velocity of 0.5 m/s, RCC reduces 17.4 % and high velocity of 1.5 m/s, decreases 6%. It can be derived that the impact of rheology on RCC is less at higher annular velocity.

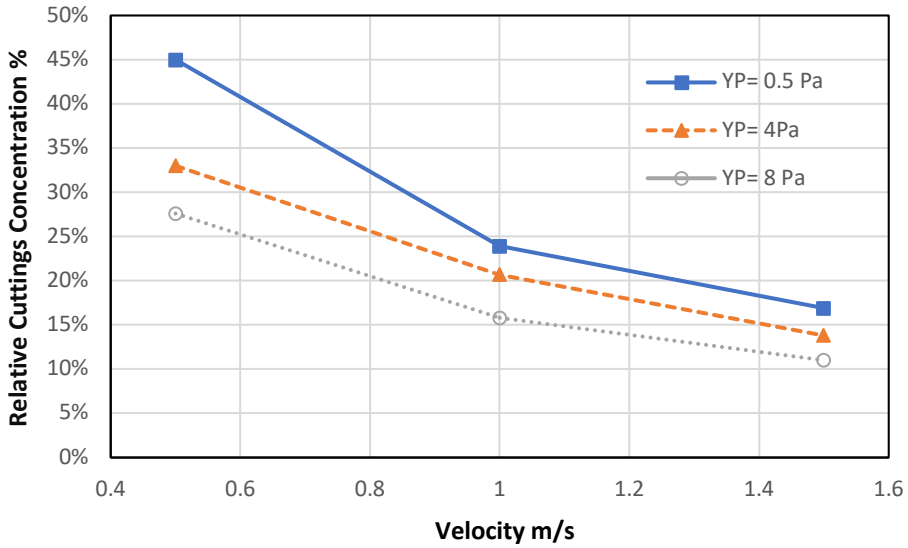

Fig. 38. Effect of yield on cleaning efficiency at different annular velocities for inclined **45°** annulus

The effect of yield value on RCC at different annular velocities for vertical annulus is presented in Fig. 39. As shown, increasing the yield value has resulted a reduction in RCC in annulus at all range of velocities. By increasing velocity from 0.5 to 1.5 m/s, RCC decreased 39 % for higher yield point (YP= 8 Pa), 40 % for intermediate yield point (YP= 4 Pa) and 47 % for lower yield point (YP= 0.5 Pa). In addition, by increasing yield value from 0.5 to 8 Pa, at low velocity of 0.5 m/s, RCC reduces 5 % and high velocity of 1.5 m/s, decreases 1.5 %. It can be derived that the impact of rheology on RCC is less at higher annular velocity.

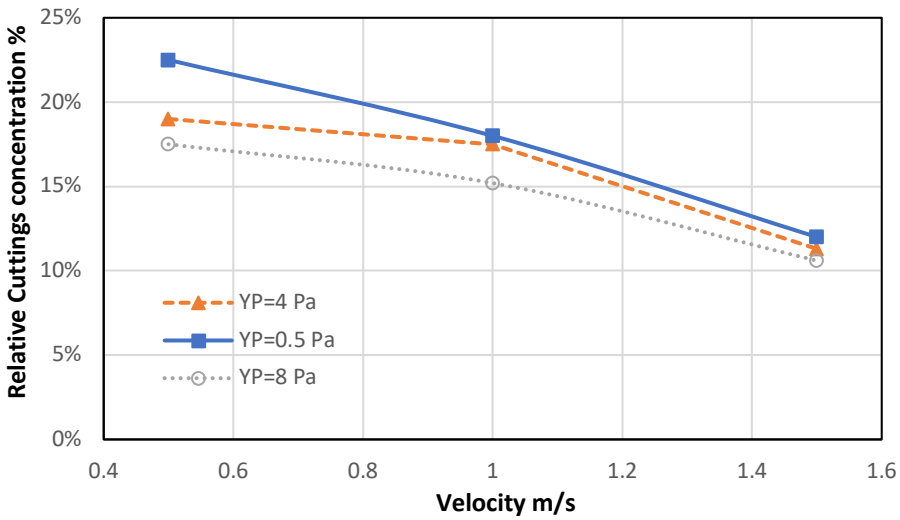

Fig. 39. Effect of yield on cleaning efficiency at different annular velocities for vertical annulus

The effect of mud yield value and annular velocity for horizontal, inclined 45°and vertical annuli is illustrated in Fig. 37, Fig. 38 and Fig. 39. As it shown, the impact of mud yield point on RCC is more pronounced at low annular velocity for horizontal annulus. On the other hand, the effect of mud yield point and annular velocity on RCC is minimized in vertical annulus. Therefore, a high viscosity mud (HVM) causes higher reduction in RCC at low velocity in horizontal annulus.

According to Table. 6 the ratio of YP/PV from LVM to IVM is increased significantly where it remained constant for HVM. The effect of mud viscosity on RCC for horizontal annulus shown in Fig.37, at low velocity of 0.5 m/s, causes higher reduction from LVM to HVM where it is small at high velocity of 1.5 m/s.

4.9 Effects of Yield Value and Inclination Angle

The effect of yield value on RCC at velocity of 1.5 m/s for different angles of inclination is studied and the results are presented in Fig. 40. The results show that the RCC within the annulus rises with an increase in the angle of inclination for all types of mud. It is worth mentioning that changing the drilling direction from vertical to horizontal has contributed to approximately 5% more RCC at low yield point (YP=0.5 Pa) within the annulus. On the other hand, RCC reduces only 1.5% at high yield point (YP= 8 Pa). This is mainly due to the effect of transverse slip velocity component of cuttings induced by gravitational force which pushes particles to the lower side of the annulus in the inclined annuli (Fig. 36). The results in Fig.40 also show a significant decrease in RCC for inclined 45° and horizontal annuli as the yield value is increased where the impact of annular velocity is dominant at vertical annulus. Based on equations (2.1, 19, 21) increasing the mud viscosity causes a reduction in the particles slip velocity. Lower slip velocity means that particles and fluid velocities are closer to each other causing lower RCC and consequently better cleaning performance within the annulus.

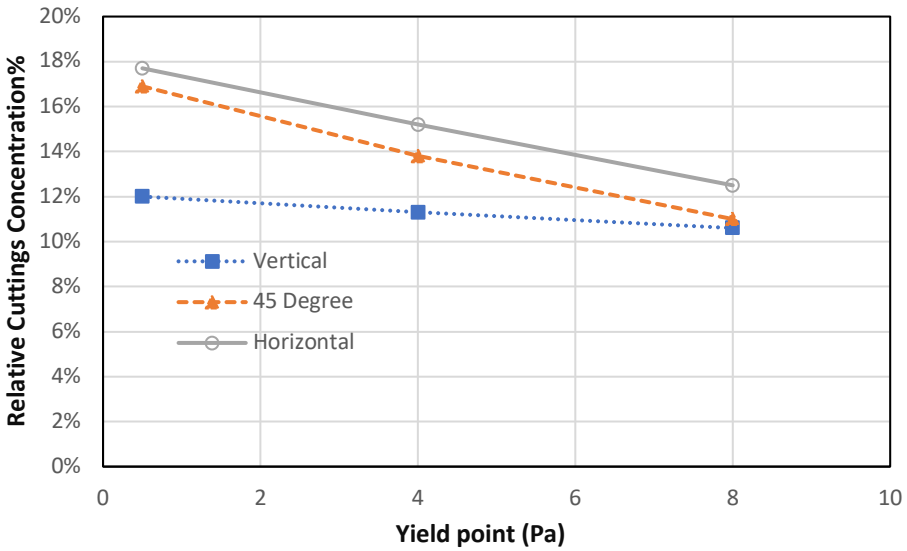

Fig. 40. Effect of yield point on cleaning efficiency at different angles of inclination (velocity 1.5 m/s).

The effect of yield value on RCC at velocity of 1 m/s for different angles of inclination is studied and the results are presented in Fig. 41. The results show that the RCC within the annulus rises with an increase in the angle of inclination for all types of mud. Changing the mud from LVM to HVM has caused nearly 17%, 34% and 32% reduction in RCC within the vertical, inclined 45° and horizontal annuli, respectively. The RCC reduction in inclined 45° and horizontal annuli is significant due to effect of transverse slip velocity component of cuttings induced by gravitational force which pushes particles to the lower side of the annulus.

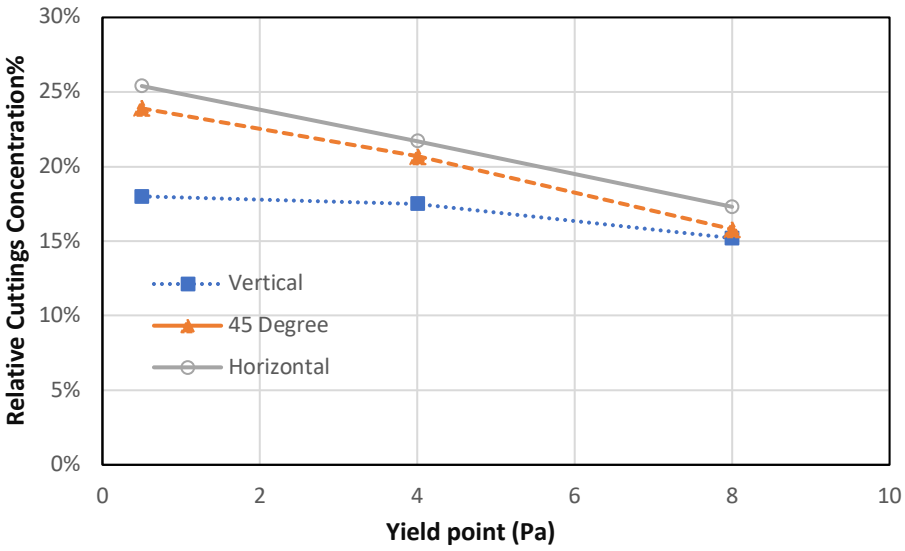

Fig. 41. Effect of yield point on cleaning efficiency at different angles of inclination (velocity 1m/s).

The effect of mud yield value on RCC at velocity of 0.5 m/s for different angles of inclination is studied and the results are presented in Fig. 42. The results show that the RCC within the annulus rises with an increase in the angle of inclination for all types of mud. Changing the mud from LVM to HVM has caused nearly 22%, 38% and 33% reduction in RCC within the vertical, inclined 45° and horizontal annuli, respectively. Increasing the mud viscosity causes a reduction in the particles slip velocity. Lower slip velocity means that particles and fluid velocities are closer to each other causing lower RCC within the annulus. Here, the inclined 45° at low annular velocity (0.5 m/s) shows higher value of RCC in comparison with horizontal annulus. The effect of inclination angle is further investigated in Chapter 5.

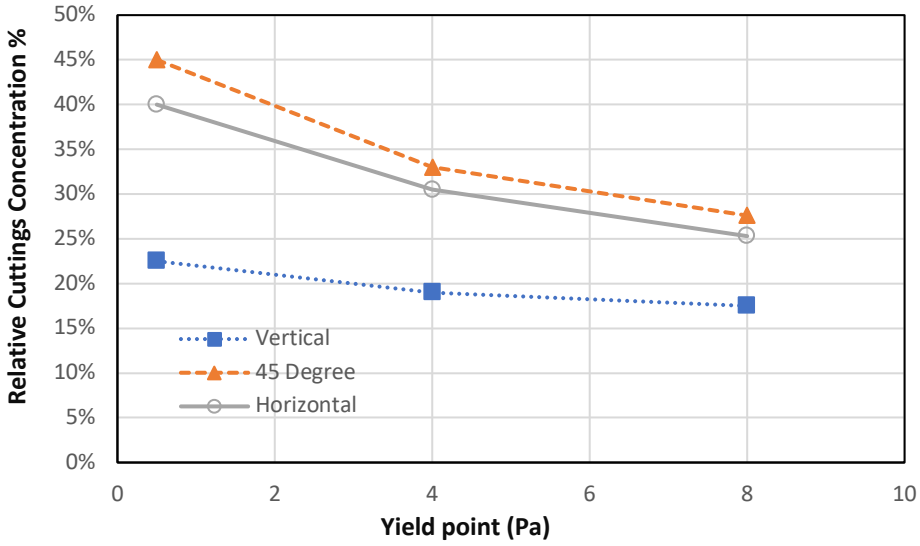

Fig. 42 Effect of yield point on cleaning efficiency at different angles of inclination (velocity 0.5 m/s).

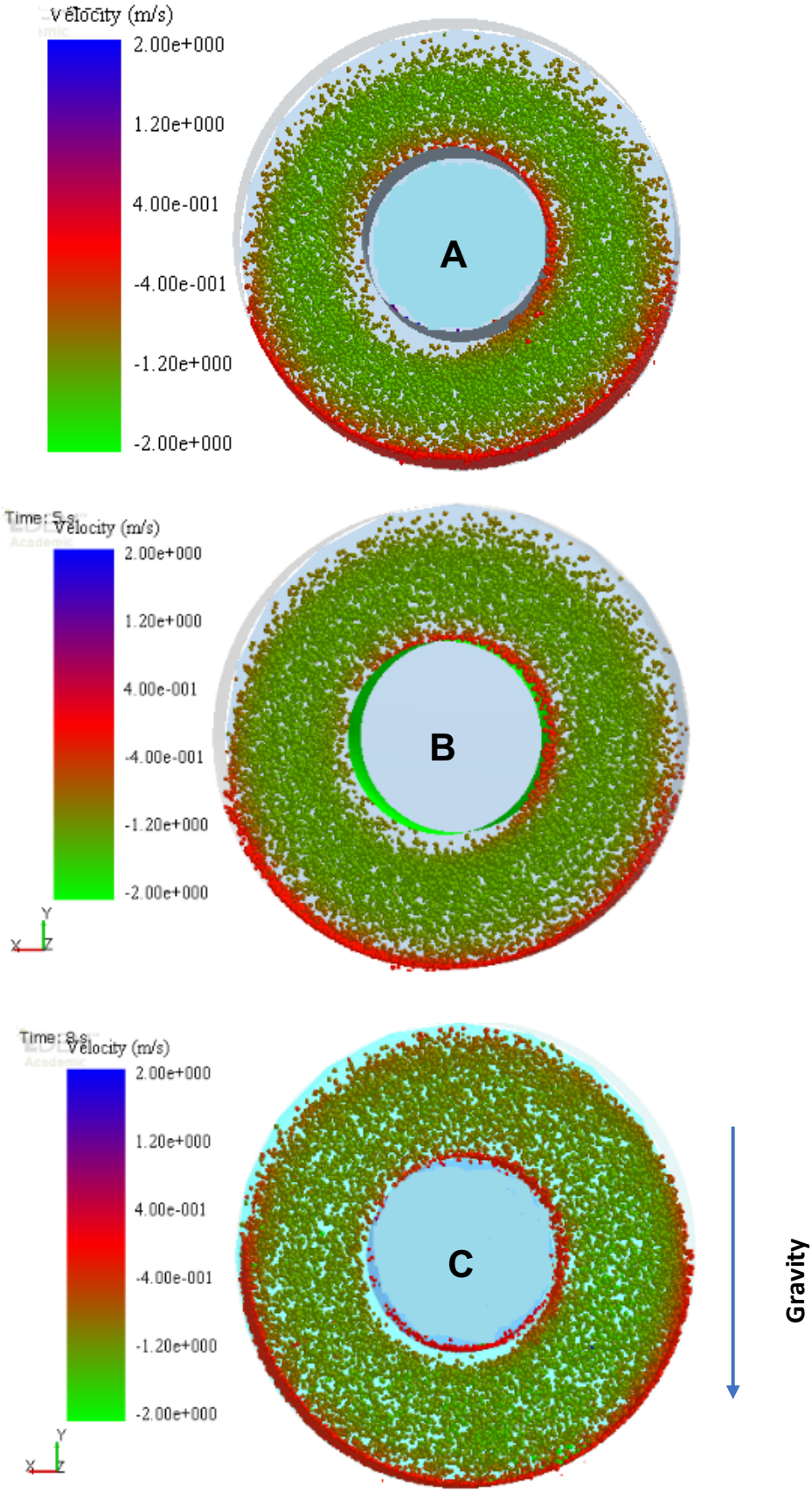

Fig. 43. Cuttings distribution in horizontal annulus at V=1m/s; (A) LVM, (B) IVM and (C) HVM.

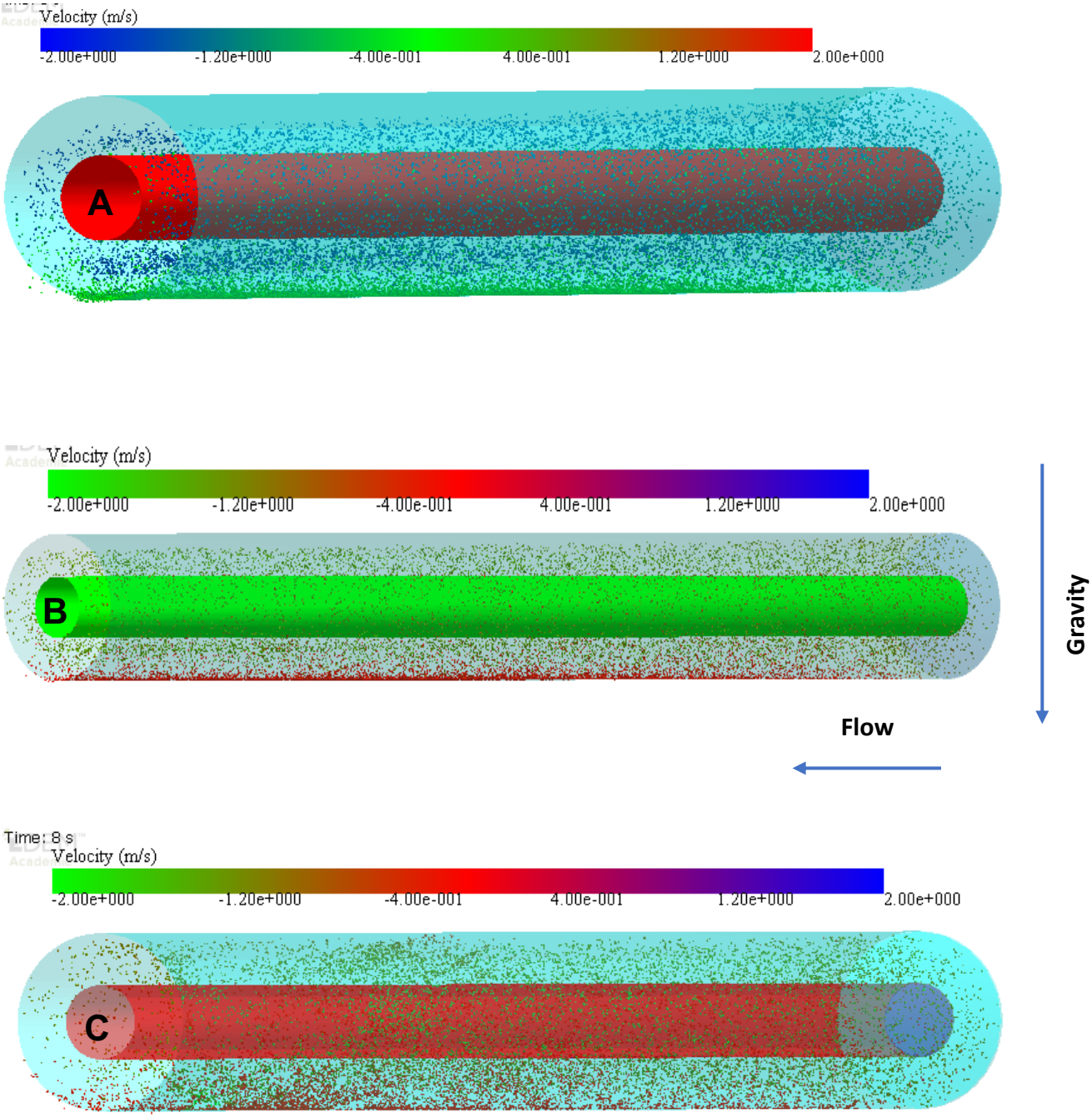

Fig. 44. Cuttings distribution in horizontal annulus at velocity 1 m/s; (a) LVM, (B) IVM and (C) HVM

Cuttings distribution in horizontal annulus at velocity of 1 m/s is shown in Fig. 43 and Fig. 44 for three different types of mud. It can be observed that the tendency of cuttings deposition at lower wall of horizontal annulus is more pronounced at LVM mud and by increasing viscosity the cuttings bed layer and relatively the cuttings concentration reduces particularly in horizontal annulus at HVM mud.

4.10 Conclusions of Mud rheology Studies

This section demonstrated the simulation results of hole cleaning efficiency with particular attention to mud yield value and evaluated on the basis of two other parameters i.e. mud velocity and inclination angle. Moreover, a new concept for analysis of particle transport based on relative cutting concentration (RCC) has been developed in this work which can describe the influence of mud hydrodynamics on cleaning efficiency in small fraction of drill string. According to generated results, the impact of yield value at higher velocities is less and it is more pronounced for lower annular velocities. The impact of yield point on RCC reduction at lower velocity of 0.5 m/s was around 15% where it is resulted in a reduction by 10% at higher velocity of 1.5 m/s. In terms of the effect of yield point on cleaning for inclined well, an increase in yield value reduces the RCC and the transport for lower angles as well as higher angles of inclination. As it is observed, this effect is slightly more significant for higher inclination angles in which the effect of axial component of particle slip velocity is minimal compared with lower inclination angles. Nevertheless, the application of high-viscosity muds to clean an annulus is reasonable for all range of angles of inclination and specifically for higher inclination it is a relief from cuttings bed formation as better drilling cuttings transport happens where the RCC is reduced.

Chapter 5

Effects of Cutting Size, Drilling Pipe Rotation and Inclination-Angle on Hole Cleaning Efficiency

5. Effects of Cutting Size, Drilling Pipe Rotation and Inclination-Angle on Hole Cleaning Efficiency

As discussed in previous chapter (section 4.6) in drilling operation rocks can produce a wide size distribution of cuttings, which will depend on the type of rock to be drilled. Typical formation rocks are sandstone, carbonate and shale have different grain sizes which in practice could influence the cutting size distribution. For example, shale rocks which are made of fine clay and minerals could produce finer cuttings than sandstone and carbonate. Nevertheless, in unresolved DEM-CFD simulation, it is not possible to consider a wide size distribution, particularly large cuttings with sizes equal or large than fluid mesh cannot be simulated. This will need the use of fully resolved particle fluid system, e.g. fluid-structure interaction with dynamic mesh [94], which is computational very expensive. Hence in this work, effect of cutting size is considered with two separate narrow size ranges compatible with the fluid mesh size. Another parameter to consider is the influence of drill pipe rotation on cutting transport in drilling operation, as in drilling conditions, different rotary speeds are implemented and in some cases the drill bit is rotated using mud motors, where the drill string remains stationary. Hence, the effect drill pipe rotation and inclination angle on the hole cleaning has also been presented and discussed. It should be noted that the simulation results are presented and discussed for fully developed fluid-particle systems with average cuttings sizes of dp=1 mm and dp=1.4 mm, drill pipe rotation of 0 rpm, 60 rpm and 120 rpm, and inclination angles of (0°, 45°, 90°).

5.1 Effect of Inclination Angle and Mud Velocity

In this section effect of inclination angle at different mud velocities are presented. In this series of simulation, three different inclination angles (0°, 45°, 90°) with three different mud velocities (0.5 m/s, 1 m/s and 1.5 m/s), 9 simulations, have been considered. All simulations have been done with high viscosity mud (HVM) with constant cutting size (1.4 mm) with 60 rpm rotation of inner pipe. The stream-wise velocity (V_z) contour snapshots of cuttings in the middle section of annulus for different inclination angles and mud velocities is

illustrated in Fig. 45. The impact of mud velocity and inclination on cuttings steam-wise velocity can be observed, where the velocity contours are different for the same cross-section (middle of annulus) of the annulus. It can be seen that the cuttings steam-wise velocity non-uniformity increases by increasing of inclination and decreasing the annular velocity. Furthermore, the velocity contours for V_y (perpendicular to steam-wise) show that at higher inclination and lower annular velocity particle tend to migrate to the bottom of the annular section (Fig. 49). The velocity contours are further investigated for the horizontal annulus (90°) and different annular velocities of 1.5 m/s, 1 m/s and 0.5 m/s as shown in Fig. 46, Fig. 47 and Fig. 48, respectively. It is clear that the uniformity of cuttings stream-wise velocity decreases by decreasing the annular velocity where the cuttings deposition at annular velocity of 0.5 m/s is evident in Fig. 48. The velocity contours for (V_y) shows that at low annular velocity (0.5 m/s) the particles are influenced by the rotation of inner pipe for vertical and horizontal annulus (90°). For inclined 45° annulus particles are moving somewhat with an opposite direction of rotation at 0.5 m/s annular velocity.

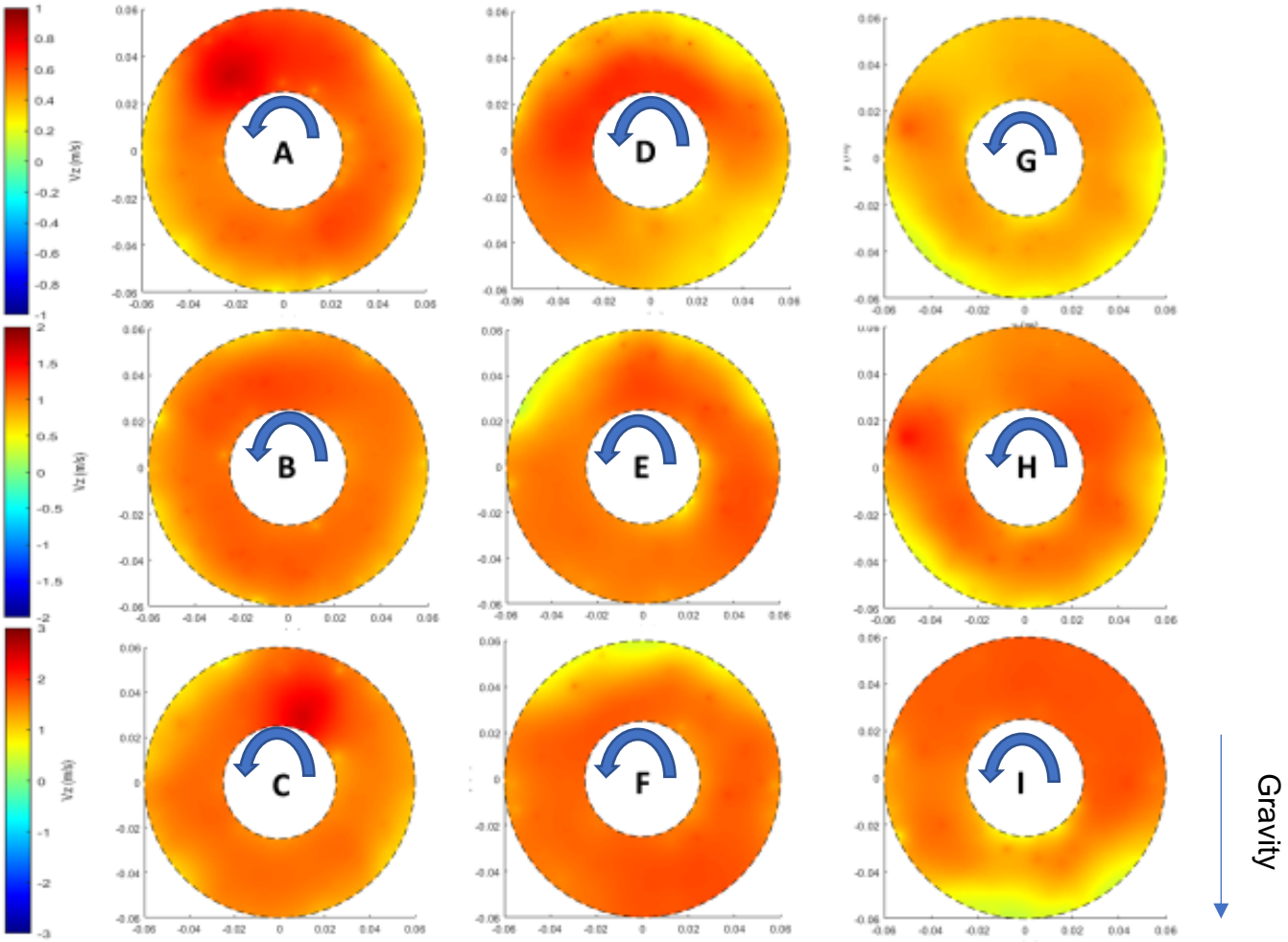

Fig. 45. Particle velocity contour V_z for different inclination angles; Vertical (A= 0.5 m/s, B= 1m/s, C= 1.5 m/s), 45 Degree (D= 0.5m/s, E= 1m/s, F= 1.5 m/s) and Horizontal (G= 0.5 m/s, H=1 m/s, I= 1.5 m/s).

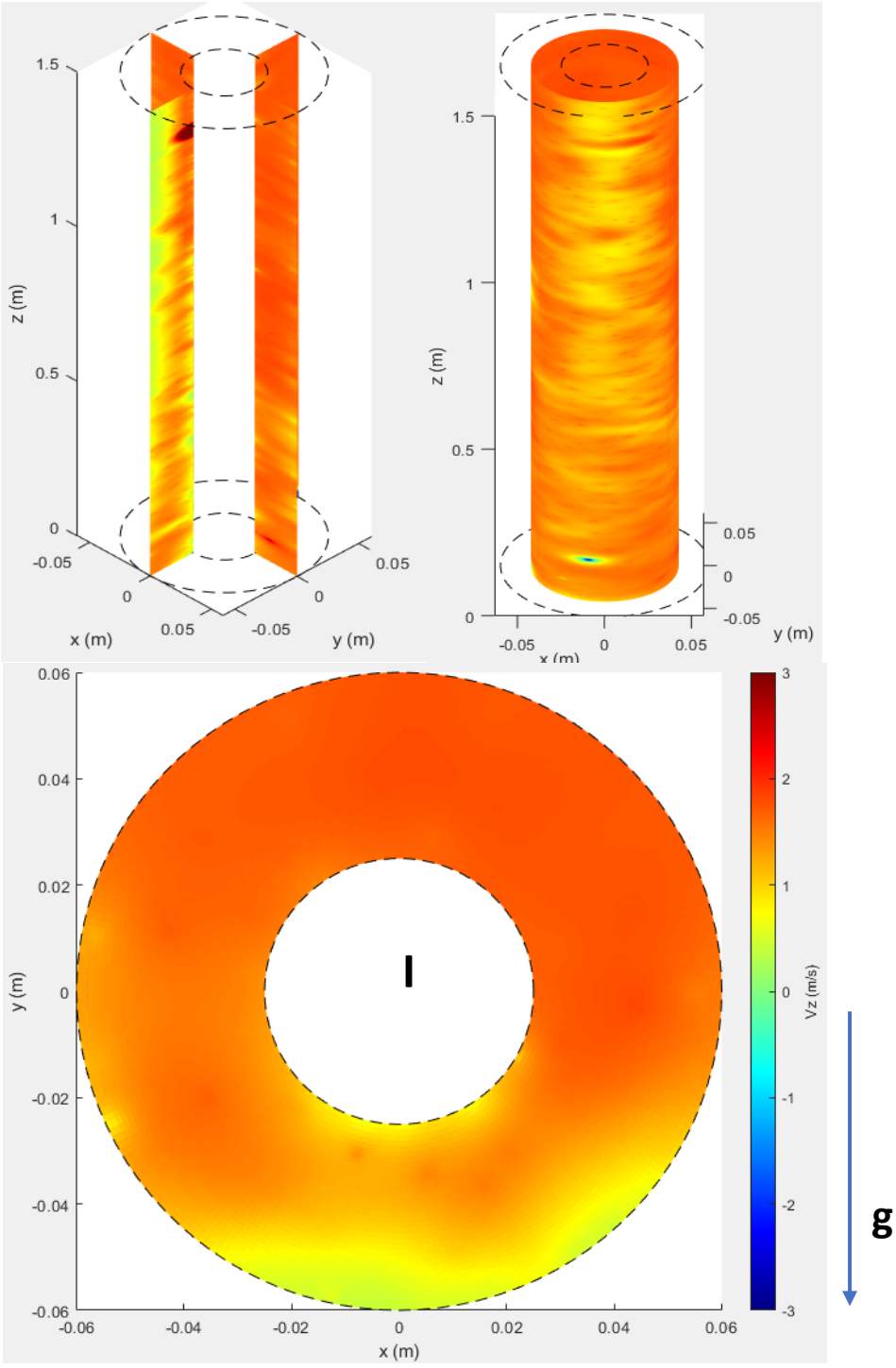

Fig. 46. Velocity contour V_z for horizontal annulus at velocity 1.5 m/s.

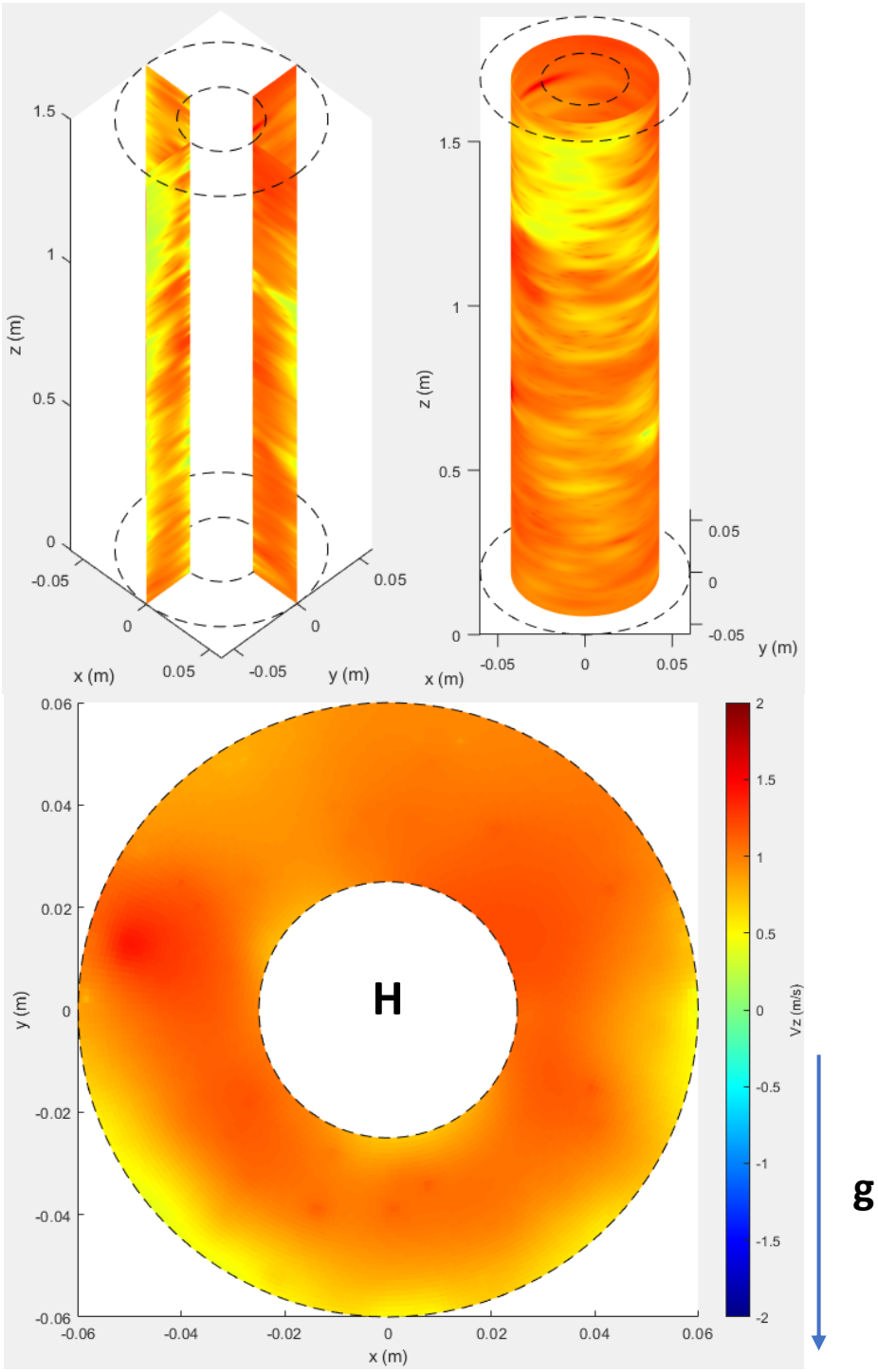

Fig. 47. Velocity contour V_z for horizontal annulus at velocity 1 m/s.

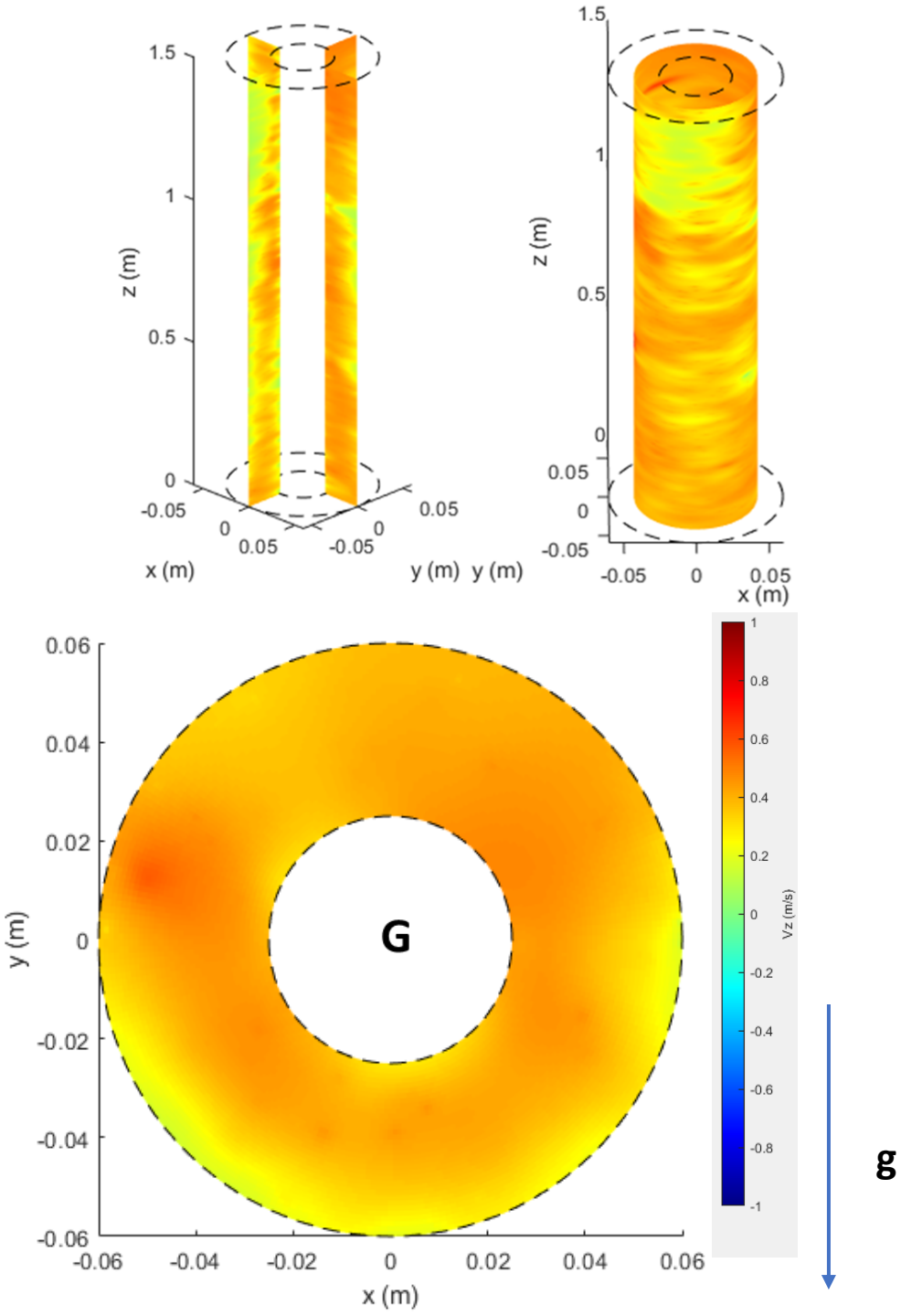

Fig. 48. Velocity contour V_z for horizontal annulus at velocity 0.5 m/s.

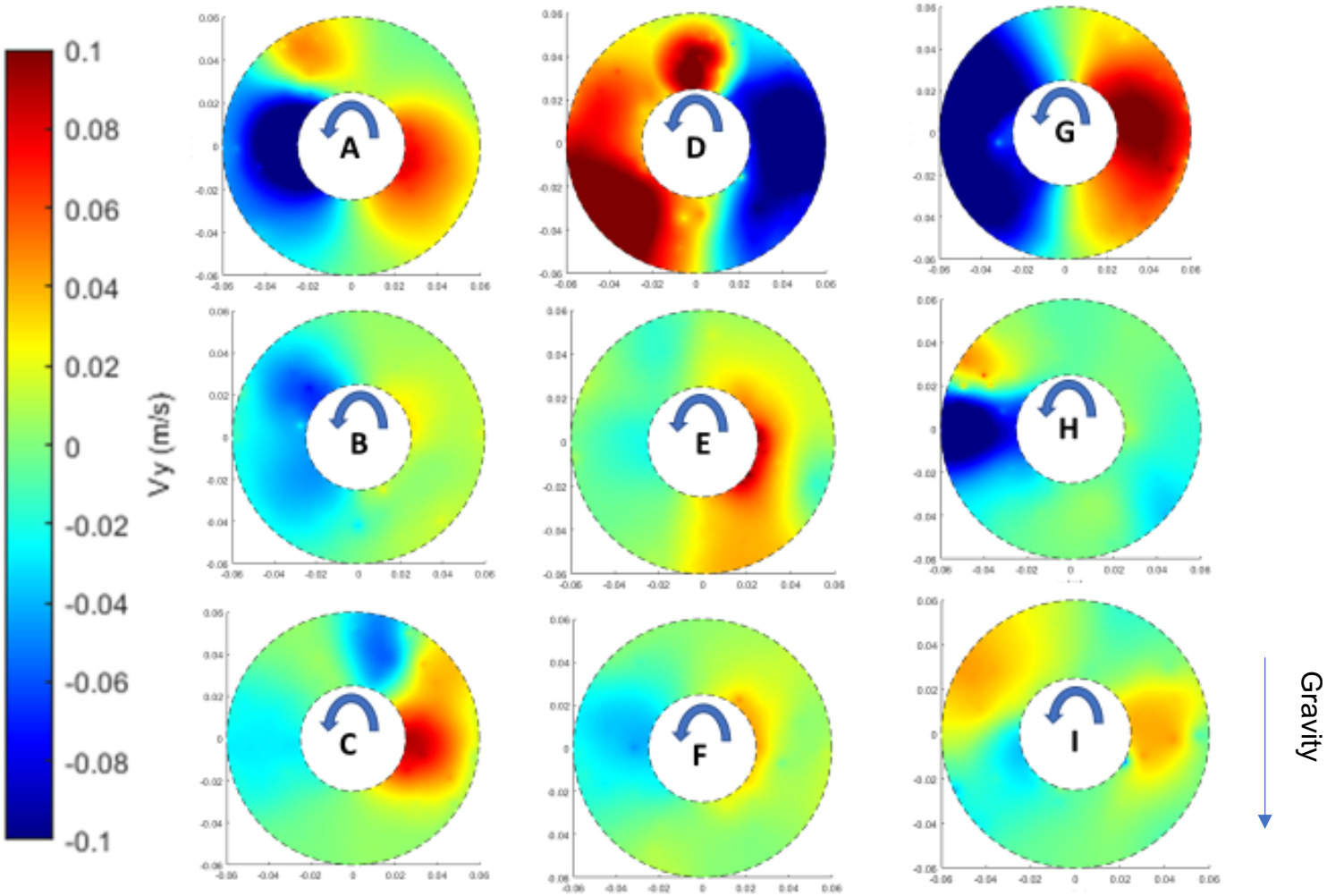

Fig. 49. Particle velocity contour for different inclination angles $\boldsymbol{V_y}$; Vertical (A= 0.5 m/s, B= 1m/s, C= 1.5 m/s), inclined 45° (D= 0.5m/s, E= 1m/s, F= 1.5 m/s) and Horizontal (G= 0.5 m/s, H=1 m/s, I= 1.5 m/s).

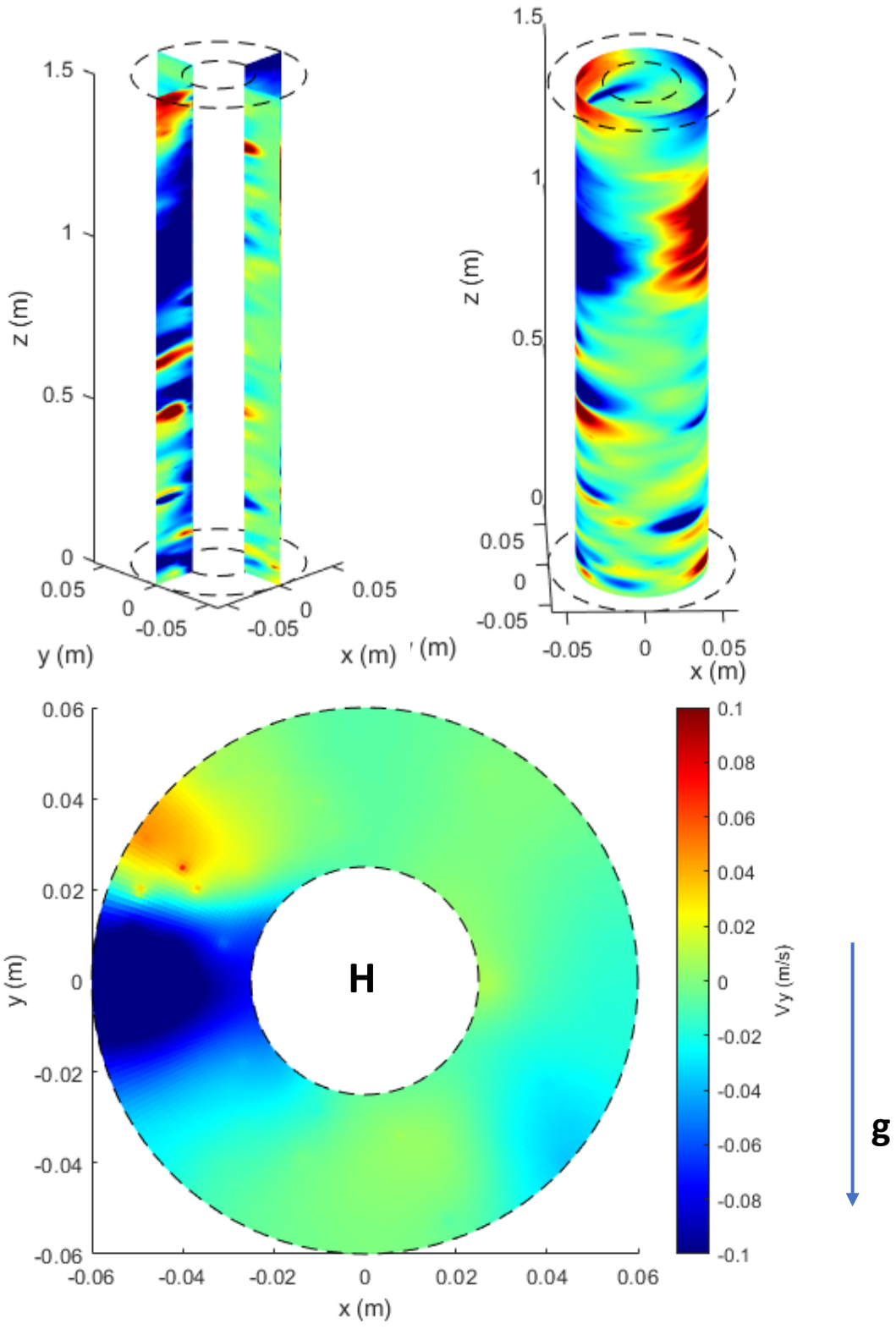

Fig. 50. Velocity contour V_y for horizontal annulus V_y at velocity 1 m/s

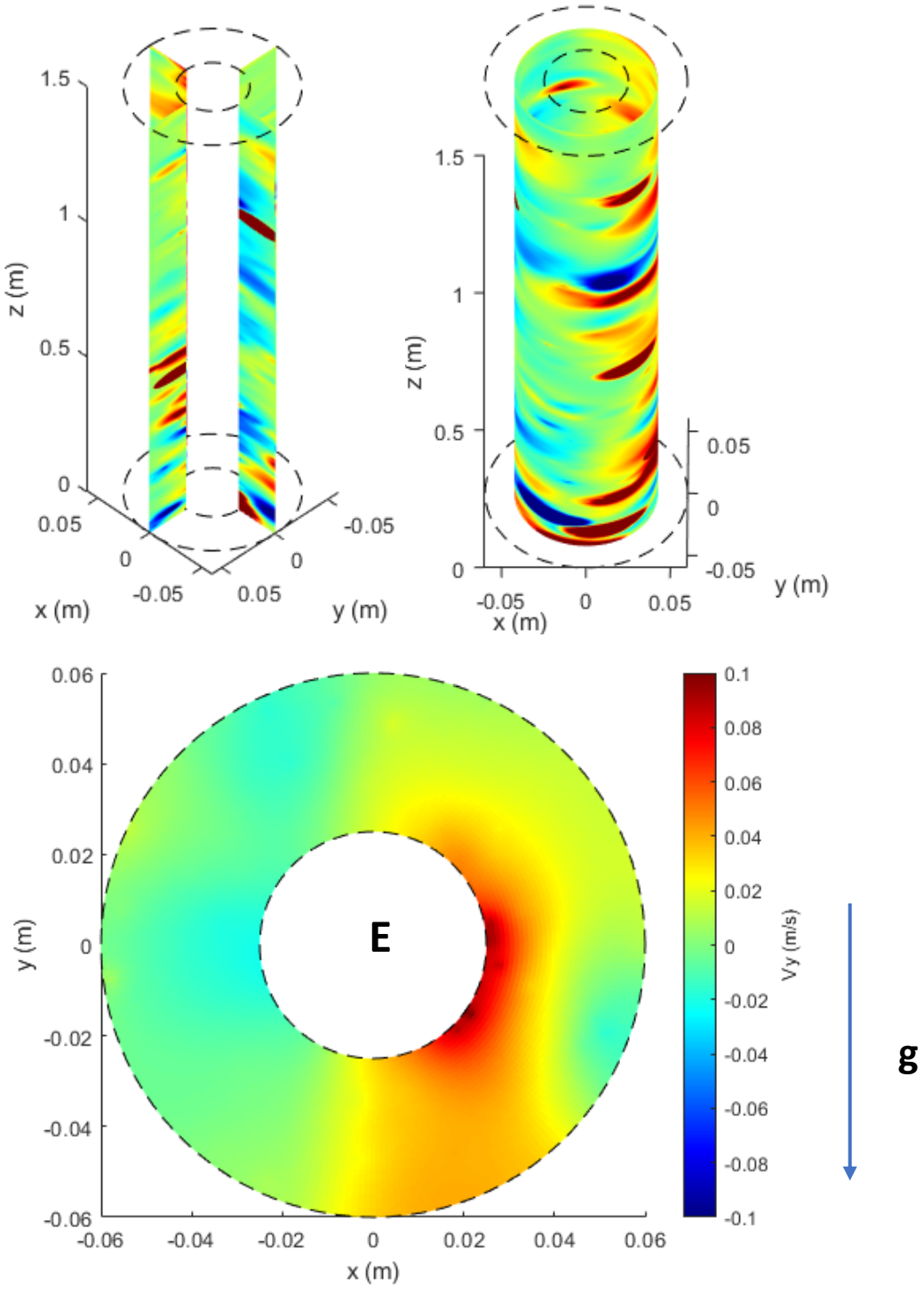

Fig. 51. Velocity contour V_y for inclined 45° annulus V_y at velocity 1 m/s.

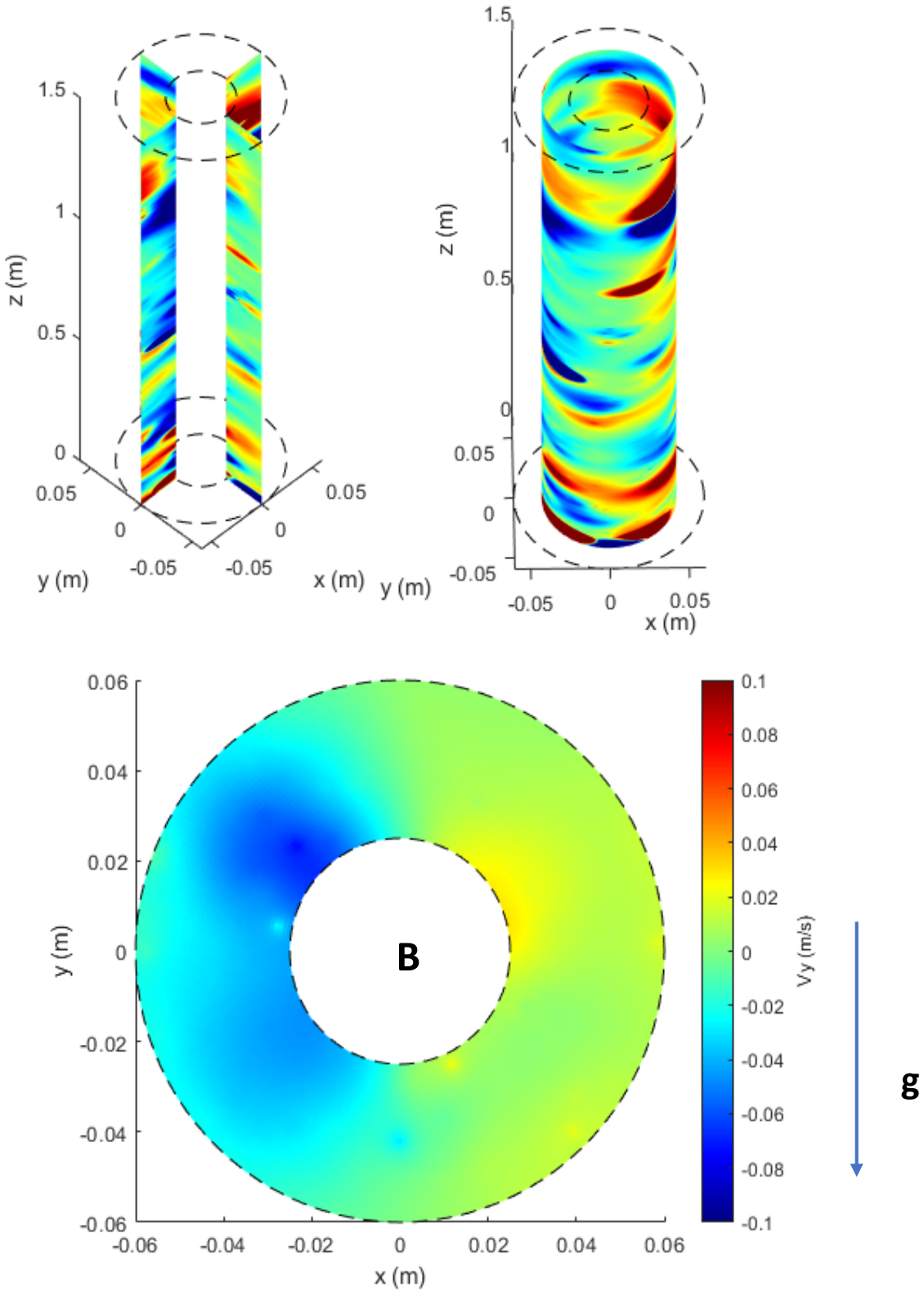

Fig 52. Velocity contour V_y for vertical annulus V_y at velocity 1 m/s.

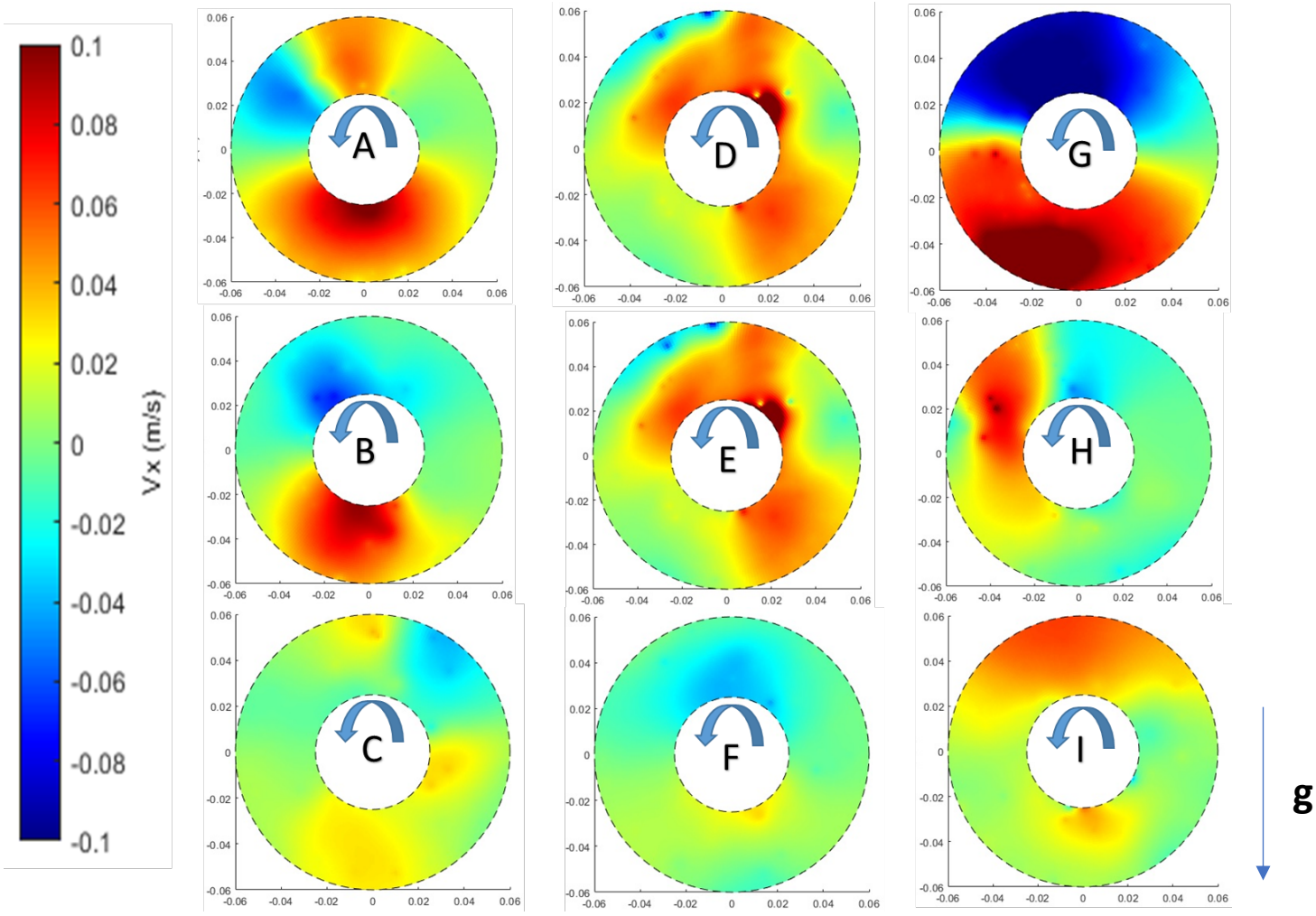

Fig. 53 Particle velocity contour for different inclination angles $\boldsymbol{V_X}$; Vertical (A= 0.5 m/s, B= 1m/s, C= 1.5 m/s), inclined 45° (D= 0.5m/s, E= 1m/s, F= 1.5 m/s) and Horizontal (G= 0.5 m/s, H=1 m/s, I= 1.5 m/s).

5.1.1 Effect of Inclination Angles and Annular Mud Velocity on Relative Cutting Concentration

The impact of wellbore deviation on RCC is studied for different annular velocities. The simulations were carried out for high viscosity mud (HVM), intermediate viscosity mud (IVM) and low viscosity mud (LVM) with velocities of 0.5 m/s, 1 m/s and 1.5 m/s and 60 rpm rotation of inner pipe. Three types of cuttings flow have been reported in experimental studies on the significance of well-bore inclination [95]. At vertical angles, the suspension mechanism is dominated, near horizontal angles, rolling mechanism is dominating and at intermediate inclination level a combination of suspension and rolling (transition from suspension to rolling) mechanisms is observed. The simulation results shown in Fig. 54 are for the effect of inclination angle on RCC with HVM. It can be seen that except at 0.5 m/s relative cutting concentration gradually increases as the well is deviated from vertical to horizontal. As it is mentioned before, due to the gravity force, the cuttings tend to accumulate near the lower wall of the wellbore with high inclination angles (Fig. 36). Consequently, RCC increases for deviated annuls in comparison with vertical wellbore in all three velocities except for the angle of $45°$ and velocity of 0.5 m/s t. At this annular velocity, for horizontal well, RCC slightly decreases as compared to 45 degree. Tomren et al. reported that the cuttings concentration faced an increase at inclination angles near $45°$ with lower annular velocities [14]. That is caused by the cuttings sliding down along the lower wall the annulus and nullifies the impact of other parameters.

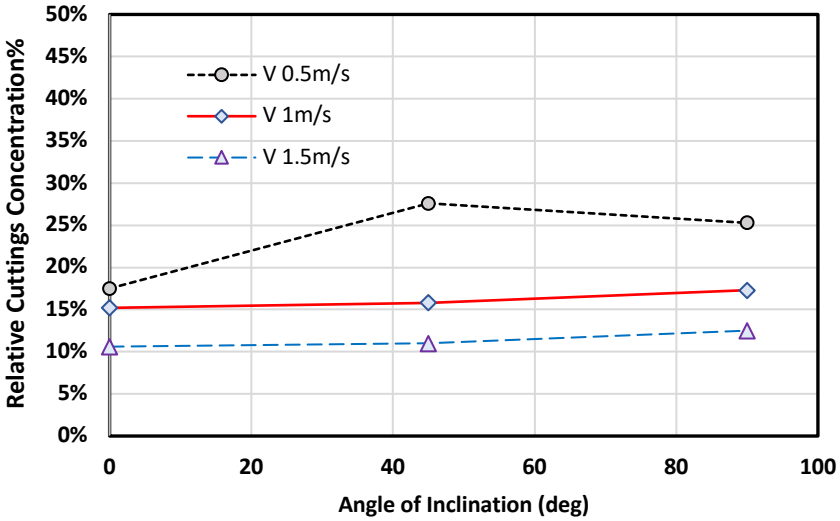

Fig. 54. Effect of angles of inclination at different mud velocities (HVM).

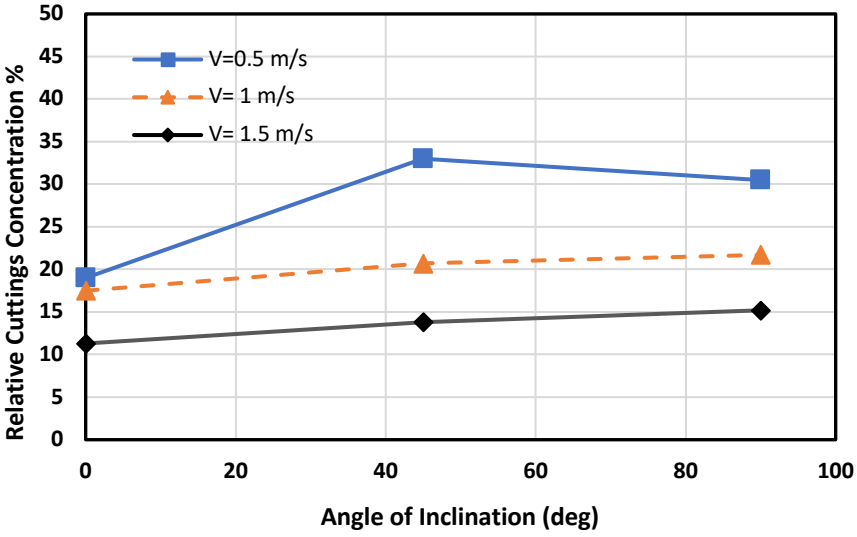

-

Fig. 55. Effect of angle on inclination at different annular velocities (IVM).

Furthermore, the simulations are carried out for intermediate mud viscosity (IVM) as well (Fig. 55). Increasing velocity from 0.5 to 1.5 m/s caused nearly a 40 % reduction in RCC in vertical annulus, where by increasing the annular velocity relative cutting concertation decreased 50% in horizontal annulus. It can be observed that deviation of the well from vertical position increases RCC at all annular velocities, except at 0.5m/s, similar to the case

of HVM. The impact of inclination angle is more notable at lower annular velocity of 0.5 m/s where RCC increased over 88% in from vertical to inclined $45°$ but further decreased by 8% in horizontal annulus as compared to 45 degree.

The comparison of RCC predicted by CFD-DEM model presented in Fig. 54 and Fig. 55 shows similar behaviour of both type of muds (HVM & IVM) where the RCC increased with the inclination angles ($0°$, $45°$, $90°$) at different annular velocities except for the inclination of $45°$ at velocity of 0.5 m/s.

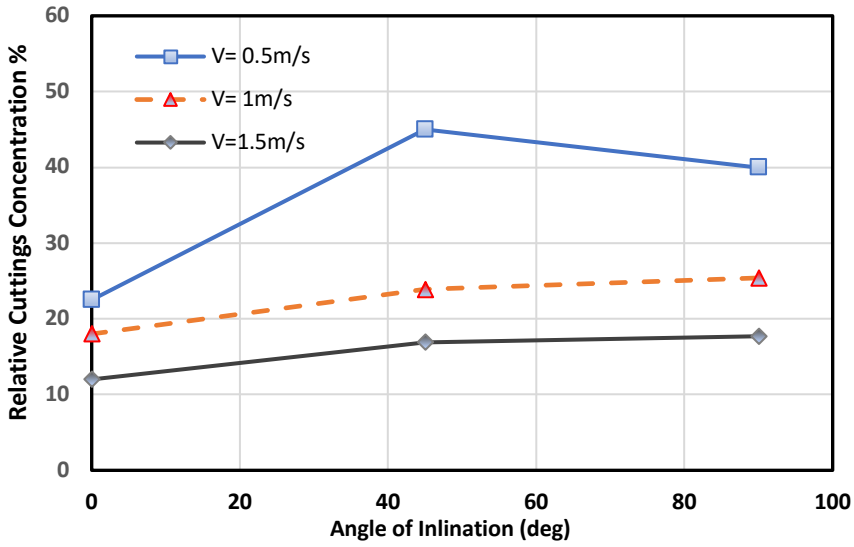

Fig. 56. Effect of angle on inclination at different annular velocities (LVM).

Moreover, the simulations are conducted for low mud viscosity (LVM) shown in Fig. 56. Increasing velocity from 0.5 to 1.5 m/s caused around 46 % reduction in vertical annulus where by increasing the annular velocity RCC decreased 55% in horizontal annulus. It can be observed that deviation of the well from vertical position increases the RCC at all annular velocities, again except for 0.5 m/s. The impact of inclination angle is more notable at lower annular velocity of 0.5 m/s where by increasing the deviation from vertical position, the RCC becomes double in inclined $45°$ and but later decreased by 11% from 45 degree to horizontal annulus, similar to the cases of HVM and IVM. It can be observed that by

reducing the mud viscosity from HVM to LVM, RCC increases where the effect of viscosity is more pronounced at low velocity of 0.5 m/s for horizontal annulus.

The cuttings distribution for different types of mud (LVM, IVM and HVM) in inclined $45°$ annulus with velocity of 0.5 m/s and 60 rpm is illustrated in Fig. 57. The cuttings accumulation at lower wall of the annulus can be observed where the uniformity of cuttings distribution is more notable at HVM.

Moreover, the cuttings distribution for LVM and HVM in horizontal annulus with velocity of 0.5 m/s and 60 rpm is shown in Fig. 58. It can be observed that the cuttings are accumulated at lower wall of horizontal annulus where the impact of HVM on the uniformity of cuttings distribution is significant in comparison with LVM.

The impact of inclination on cuttings transport is shown in Fig. 59. As it was mentioned in section 5.1, Clark et al.[95] reported three significant types of cuttings movement mechanism in their experimental study on the effects of well-bore inclination: suspension, transition and rolling. Suspension is occurred at the inclination angle near vertical, rolling in horizontal annulus and a combination of suspension and rolling (sliding) in inclined $45°$-$50°$. Suspension mechanism caused a uniform distribution in vertical annulus where the bed formation phenomena at lower wall annulus (due to gravity) in middle and higher inclination angles, ended in rolling mechanism of cuttings while sliding mechanism of transport occurred above the bed layer in inclined $45°$ annulus. At low velocity of 0.5 m/s the bed formation phenomenon is more notable where the drag force exerted on particles is lower in comparison with higher annular velocities. The sliding motion of cuttings in inclined $45°$ annulus at velocity of 0.5 m/s is dominating and leads to higher RCC for horizontal annulus at velocity of 0.5 m/s.

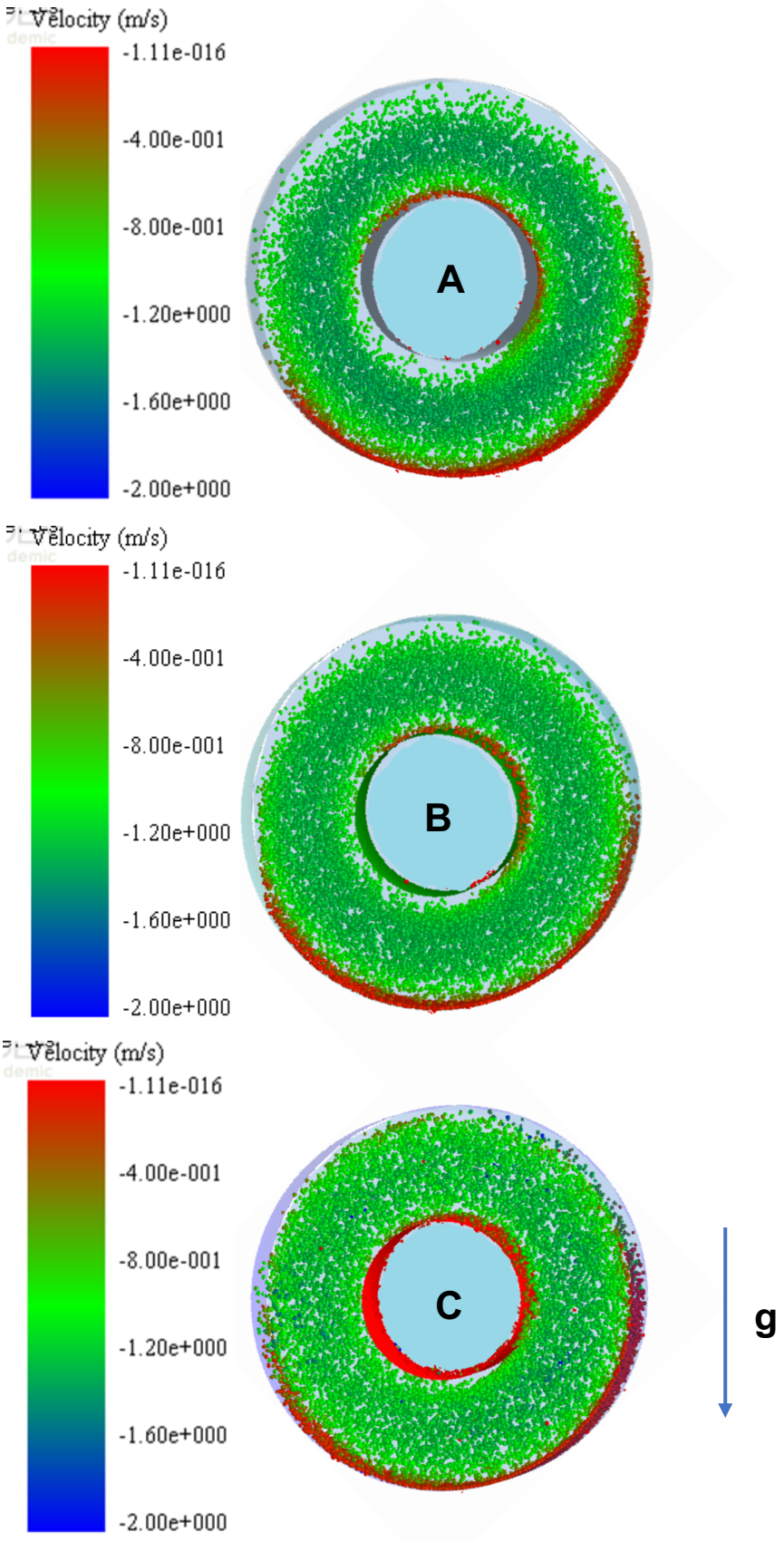

Fig. 57. Cuttings distribution in 45° annulus at V=0.5m/s; (A) LVM, (B) IVM and (C) HVM.

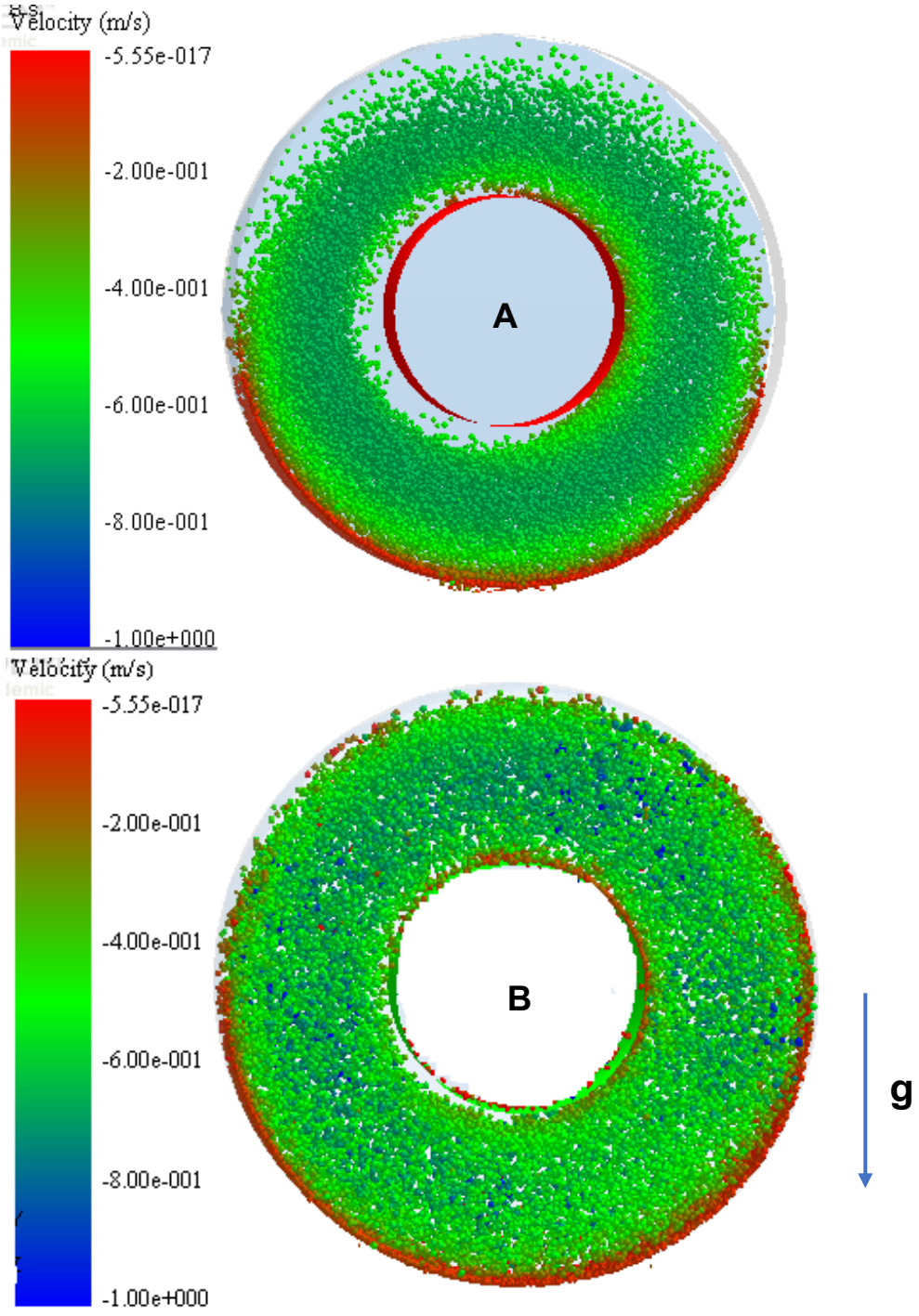

Fig. 58. Cuttings distribution in horizontal annulus at V=0.5 m/s; (A) LVM and (B) HVM.

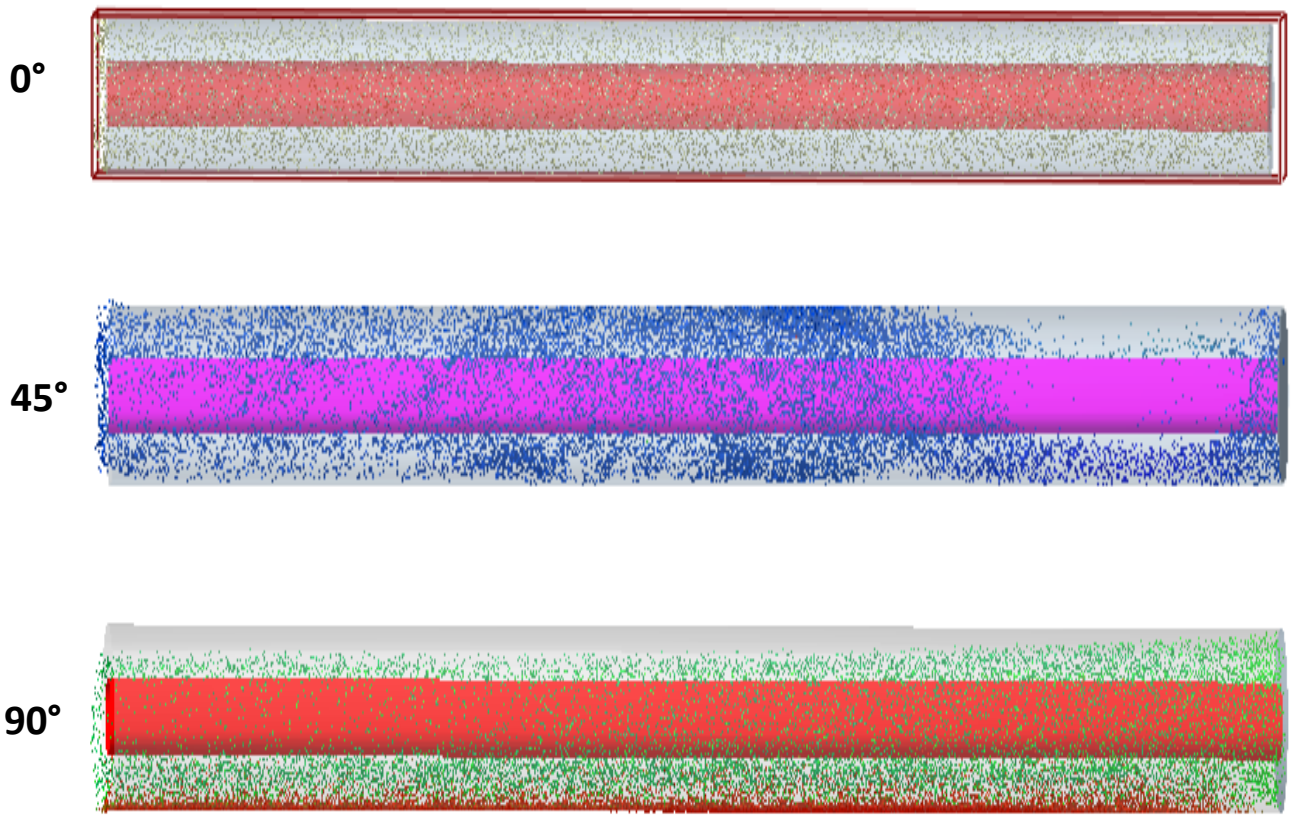

Fig. 59. Effects of inclination on cuttings transport mechanism at annular velocity 0.5m/s

5.2 Effect of Cuttings Size and Velocity

The effect of particle size on RCC is studied for the average particle diameters of 1mm and 1.4 mm. In these series of simulations, annular velocities were varied from 0.5 to 1.5 m/s but the mud viscosity was kept constant (HVM). The inner pipe was rotate at 60 rpm. Simulation results of RCC versus mud velocity through the length of horizontal annulus is illustrated in Fig. 60. By reducing cutting size in simulations from 1.4mm to 1 mm, at constant velocity of 0.5, 1 and 1.5 m/s, the RCC reduces 27%, 34% and 35% respectively. It means that at certain mud velocity, transport efficiency of larger particles is lower than smaller particle in the annular space. According to equation (2.21), slip velocity and Stokes number are higher for larger particles. Consequently, small particles are the easiest one to remove from the annulus and have better cleaning performance compared with larger sizes.

By increasing the annular velocity from 0.5 to 1.5 m/s, the RCC reduces 50% for larger particle where RCC reduces 60% for the smaller cutting size. It is observed that the impact of particle size on RCC is more pronounced at higher mud velocities due to the positive influence of increasing mud flow rate on removal of cuttings from the annulus.

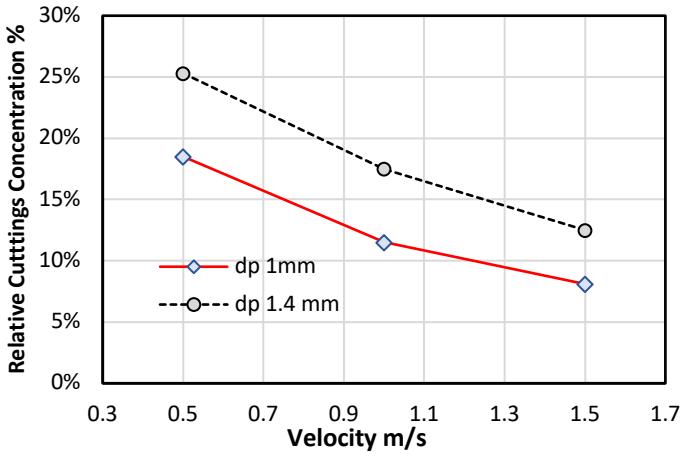

Fig. 60. Effect of cuttings size on cleaning efficiency at different mud velocities.

5.3 Effect of Drill Pipe Rotation and Velocity

The effect of drill pipe rotation on RCC for various mud velocities is investigated in this section. Simulations were carried out with average particle size of 1.4 mm and constant mud viscosity (HVM) with varying annular velocities and well inclinations. Fig. 61 demonstrates the effect of rotation on RCC for different annular velocities of horizontal well. An increase in drill pipe rotation tends to slightly reduce RCC in the annulus where by increasing drill pipe rotation from zero to 120 RPM at certain velocity of 0.5, 1 and 1.5 m/s, RCC reduces by 15%, 6% and 5%, respectively. Increasing the drill pipe rotation motivates the cuttings to travel in the middle of the annulus rather than near the walls due to the lifting effect. Moreover, it can be observed that at higher mud velocity the impact of drill pipe rotation on RCC in annulus is lower and the drill pipe rotation has negligible improvement in cuttings transport rate in the annulus. In comparison with other parameters

investigated in this study, drill pipe rotation shows less impact on RCC under turbulent flow regime and it is more pronounced at lower annul velocities.

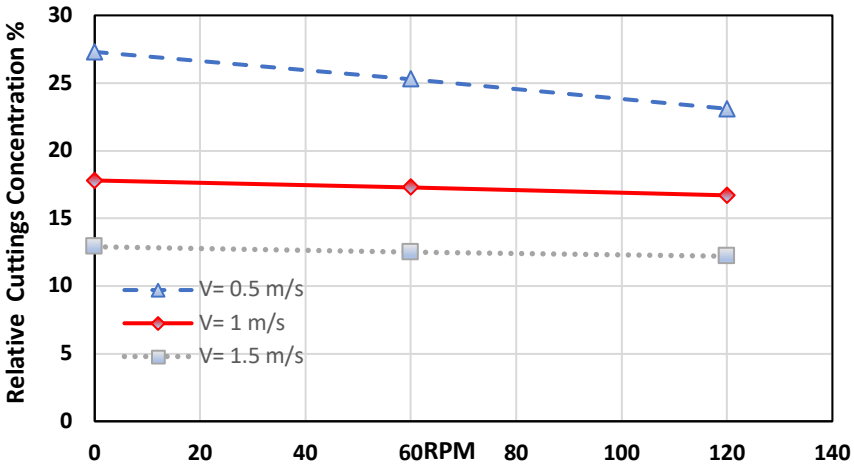

Fig. 61. Effect of inner pipe rotation on relative cuttings concentration in horizontal annulus

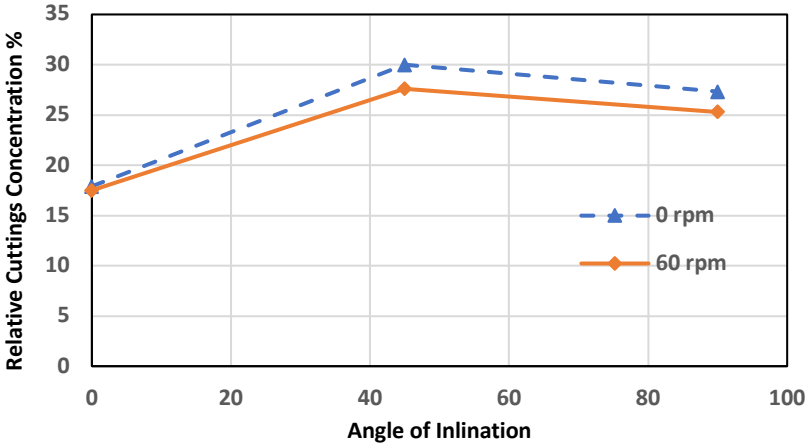

Fig. 62. Cuttings concentration vs. angle of inclination for different rpm (V= 0.5 m/s).

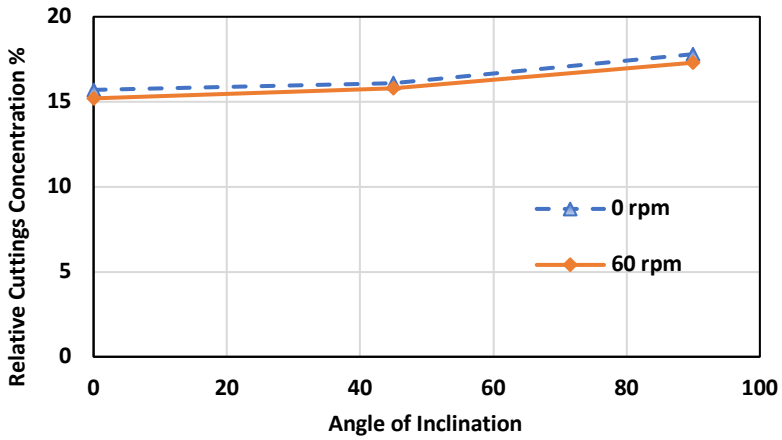

Fig. 63. Cuttings concentration vs. angle of inclination for different rpm (V= 1 m/s).

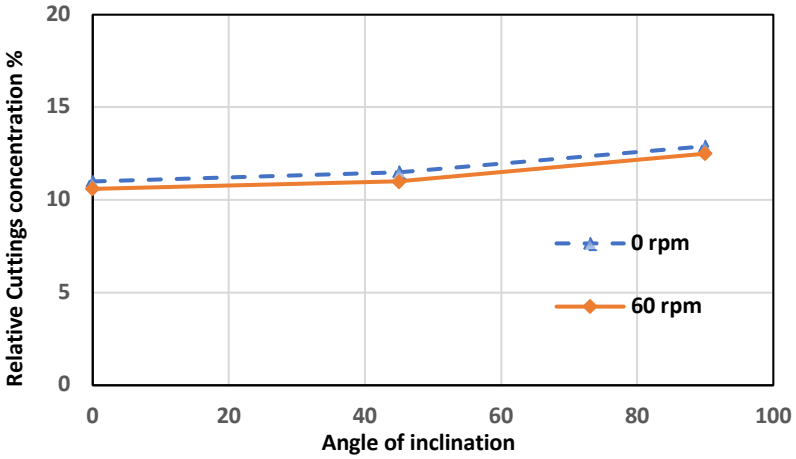

Fig. 64. Cuttings concentration vs. angle of inclination for different rpm (V= 1.5 m/s).

The percentage of RCC for the inclination angles of $0°$, $45°$ and $90°$ with HVM and different velocity (0.5 m/s, 1 /s and 1.5 m/s), for zero and rotating speed of 60 rpm are illustrated in Fig. 62, Fig. 63 and Fig. 64. It can be seen that in horizontal annulus, the effect of rotation is only noticeable for 0.5 m/s annular velocities. For vertical annulus, by increasing drill pipe rotation from zero to 60 RPM for all annular velocities, the RCC remains nearly constant. A noticeable effect of rotation can only be seen for the inclined $45°$ and horizontal annuli at annular velocity of 0.5 m/s, where increasing the drill pipe rotation from zero to 60 RPM, resulted in the RCC reduction by 8% and 7%, respectively. However, the impact of drill pipe rotation on decreasing the RCC is almost negligible at higher annular velocities of 1 and 1.5 m/s.

The selected particles streamlines are illustrated around the drill pipe at horizontal annulus for HVM with different annular velocities in Fig. 65. The streamlines of few particles are presented during the simulation time. The illustrations are at 0.9s of simulation for the annular velocities of 0.5, 1 and 1.5 m/s. It can be observed that cuttings streamline in annulus are more affected by drill rotation where the lower annular velocity of 0.5 m/s showed more sensitivity to drill pipe rotation while rotation has less impact at the higher annular velocities. Also, the entire cuttings trajectory is framed in Fig. 66 where the effect of drill pipe rotation can be seen for 0.5 and 1 m/s.

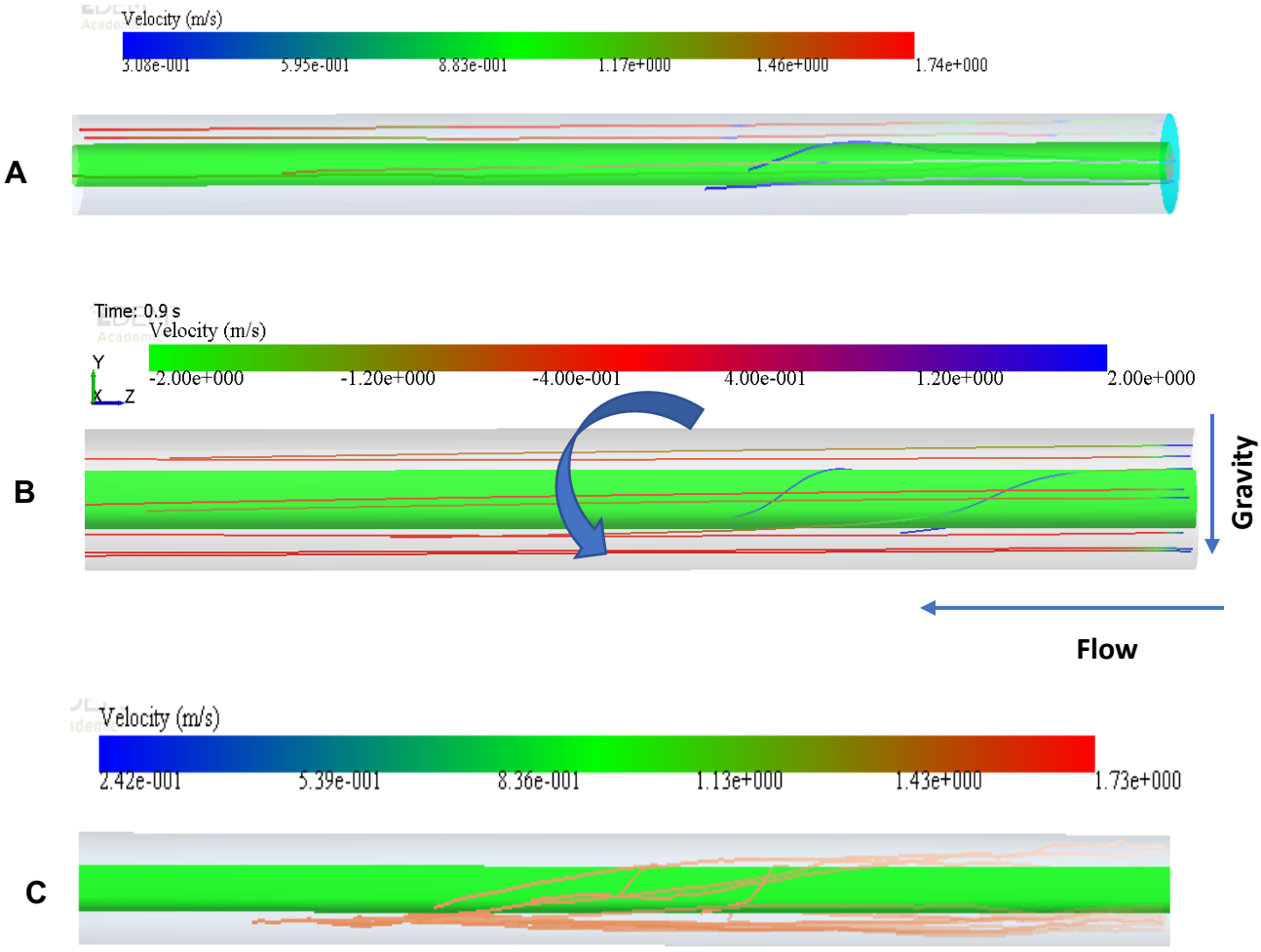

Fig. 65. Effect of inner pipe rotation on cuttings transport for selected particles streamline at horizontal wellbore; (A) V=1.5 m/s, (B) V= 1m/s and (C) V=0.5 m/s.

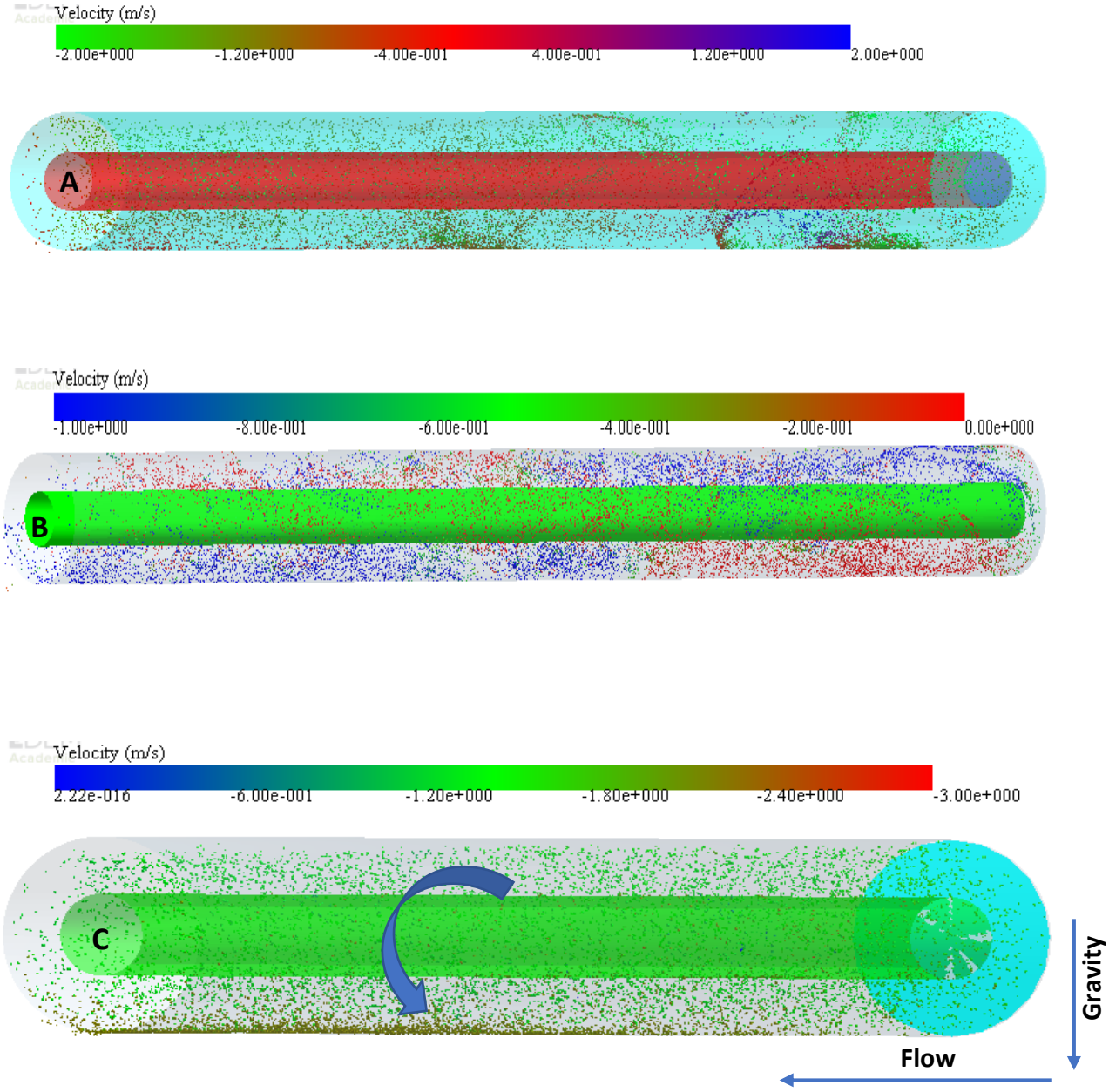

Fig. 66. Effect of drill pipe rotation in cuttings trajectory in horizontal annulus; (A) V= 0.5 m/s, (B) V= 1m/s and (C) V= 1.5 m/s.

5.4 Conclusions of Cuttings Size, Inclination Angle and Drill Pipe Rotation impact on Hole Cleaning

This section demonstrated the simulation results of hole cleaning efficiency with particular attention to inclination angle and mud velocity, cuttings size and drill pipe rotation on hole and results are evaluated on the basis of impact of these parameters on RCC. According to generated results, by increasing velocity the drag force exerted on particle can increase and cuttings can overcome the gravitational force. Also, by increasing the deviation from vertical position by increasing the radial component of slip velocity and impact of the bed formation phenomena at the lower wall of the deviated annuli, due to gravitational force, the percentage of RCC increases. Therefore, at the lower annular velocity and the inclination close to the horizontal, the particle deposition concentration increases and reduces the cuttings transport efficiency. The only exception observed is the behavior of the inclined $45°$ at lower annular velocity of 0.5 m/s where it has been shown that higher relative cuttings concentration exists at all types of mud viscosity. The impact of inclination angles on all three types of mud viscosity showed that by increasing the mud viscosity from LVM to HVM lower percentage of RCC is obtained at annulus, where the RCC increases from vertical to the inclination close to horizontal, except for the inclined $45°$ at the velocity of 0.5 m/s, since sliding of the cuttings down to the lower wall is the dominant motion.

The impact of cuttings size is investigated for average particles sizes of 1 and 1.4 mm in horizontal annulus. The results showed the better cuttings transport for smaller particle size at higher annular velocities where the lager particles size tend to settle due to the gravitational force.

The simulations were carried out for the effect of drill pipe rotation on RCC in horizontal annulus with different annular velocities where the drill pipe rotation varied from zero to 120 RPM. The generated results showed the impact of drill pipe rotation is more pronounced at lower annular velocity and mud viscosity (HVM) where the percentage of RCC is reduced by 15% when the drill pipe rotation is increased from zero to 120 RPM. For high mud viscosity, the effect of drill pipe rotation is minimal. Furthermore, the impact of drill pipe rotation at different annular velocities on RCC is investigated for vertical and

deviated annuli where the drill pipe rotation varies from zero to 60 RPM. The results showed that by increasing the drill pipe rotation the percentage of RCC reduced effectively at lower annular velocity of 0.5 m/s and the inclination close to horizontal. However, the contribution of drill pipe rotation on decreasing the percentage of RCC is almost negligible at vertical annulus.

Particle averaged velocity components in X, Y and Z direction for vertical, inclined $45°$ and horizontal annulus for high viscosity mud (HVM) at annular velocities of 0.5, 1 and 1.5 m/s with 60 rpm are illustrated in 9 graphs from Fig. 67 to Fig.75.

Velocity components shown in Fig. 67, Fig. 68 and Fig. 69 are highly influenced by annular velocity of 1.5 m/s and inclination angle. The cuttings average velocities are close to the annular velocity of 1.5 m/s for vertical annulus at z-direction while it reduced to 1.4 m/s and 1.2 m/s for inclined $45°$ and horizontal annulus, respectively.

For the annular velocity of 1 m/s the particle velocity components shown in Fig. 70, Fig. 71 and Fig. 72 at z-direction reached to an average value of 1 m/s for vertical annulus where the particle averaged velocities (Z-direction) are close to 0.9 m/s and 0.8 m/s for inclined $45°$ and horizontal annulus, respectively.

For the annular velocity of 0.5 m/s the particle velocity components shown in Fig. 73, Fig. 74 and Fig. 75 at z-direction are close to an average value of 0.5 m/s for vertical annulus, where it is close to 0.4 m/s for inclined $45°$. Here, the inclined $45°$ shows slightly lower average annular velocity in compare with horizontal annulus due to cuttings sliding down along the lower wall of the annulus.

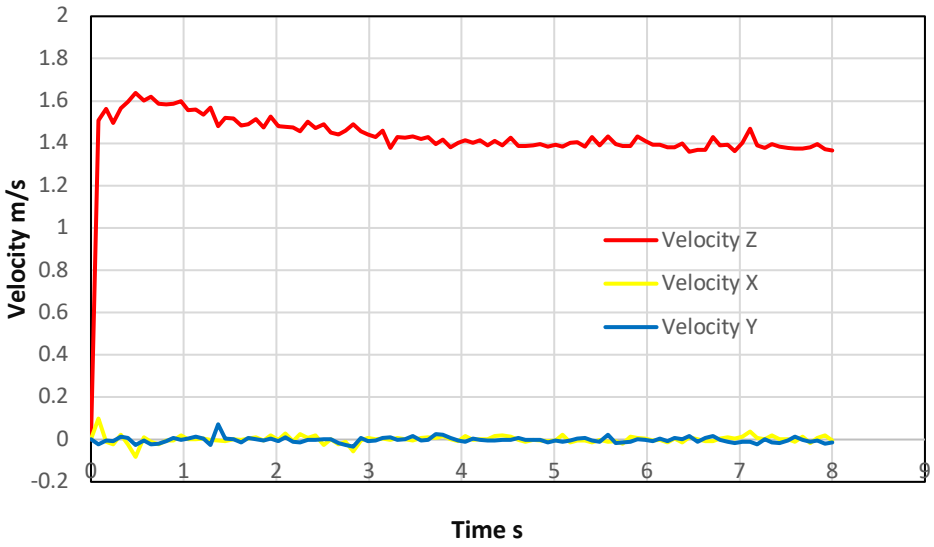

Fig. 67. Velocity components for vertical annulus at annular velocity 1.5 m/s.

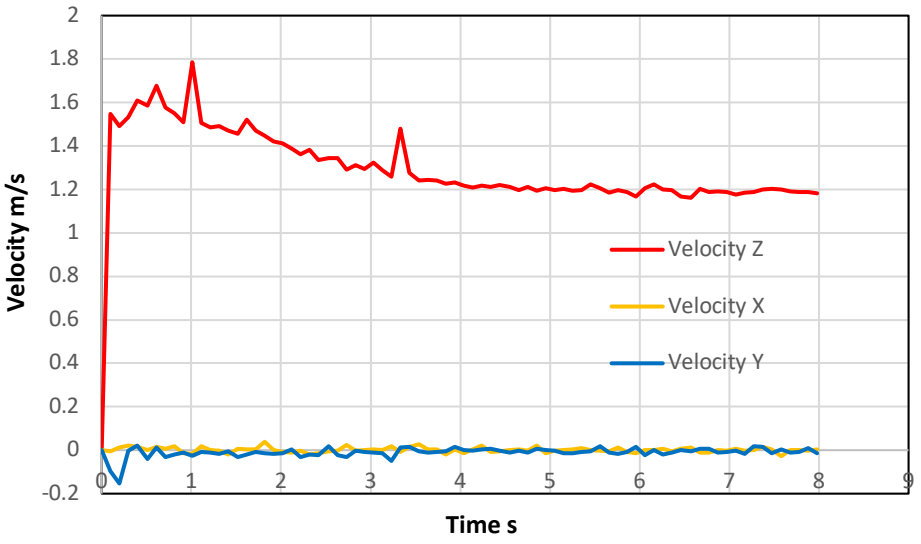

Fig. 68. Velocity components for horizontal annulus at annular velocity 1.5 m/s.

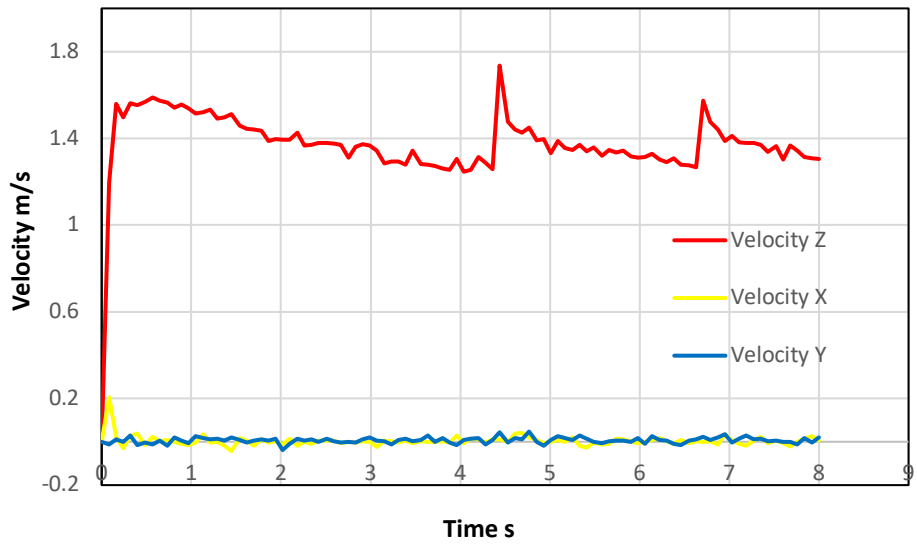

Fig. 69. Velocity components for inclined $45°$ at annular velocity 1.5 m/s.

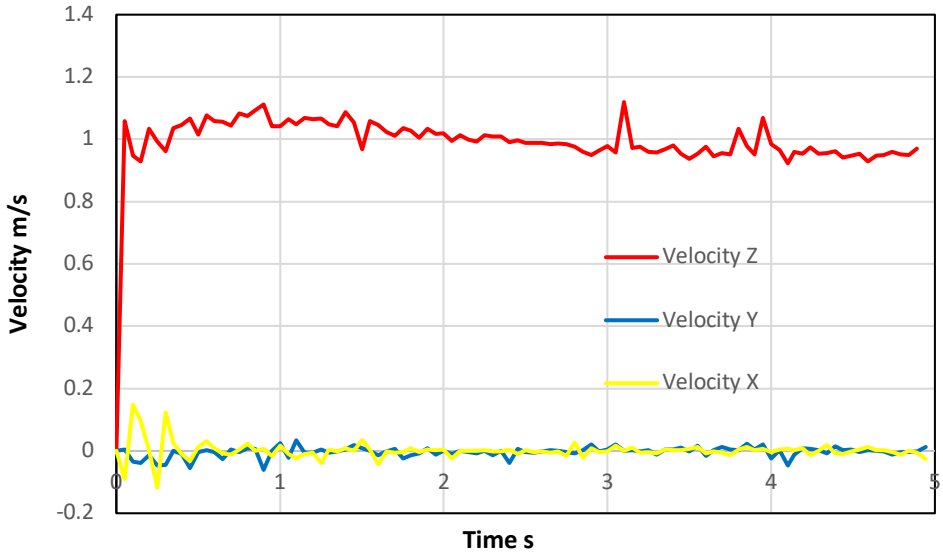

Fig. 70. Velocity components for vertical annulus at annular velocity 1 m/s.

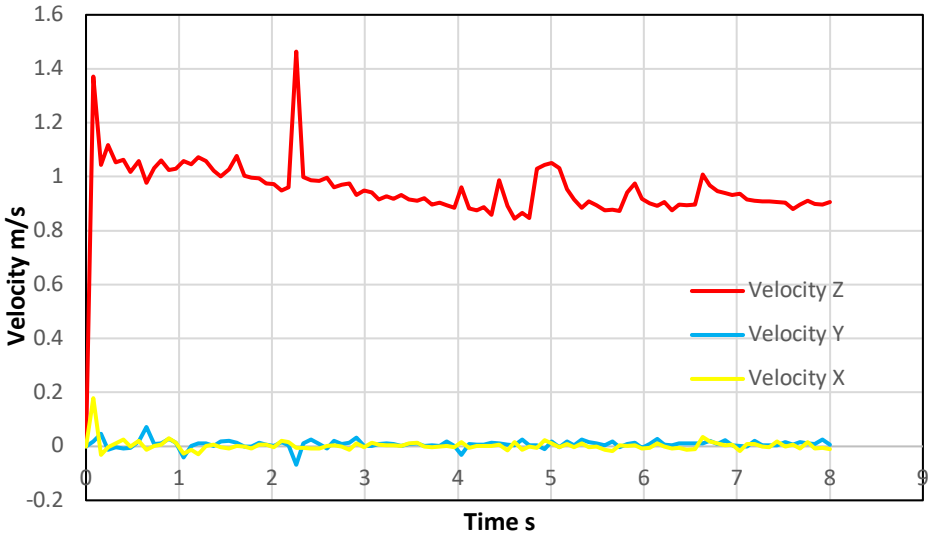

Fig.71. Velocity components for inclined $45°$ at annular velocity 1 m/s.

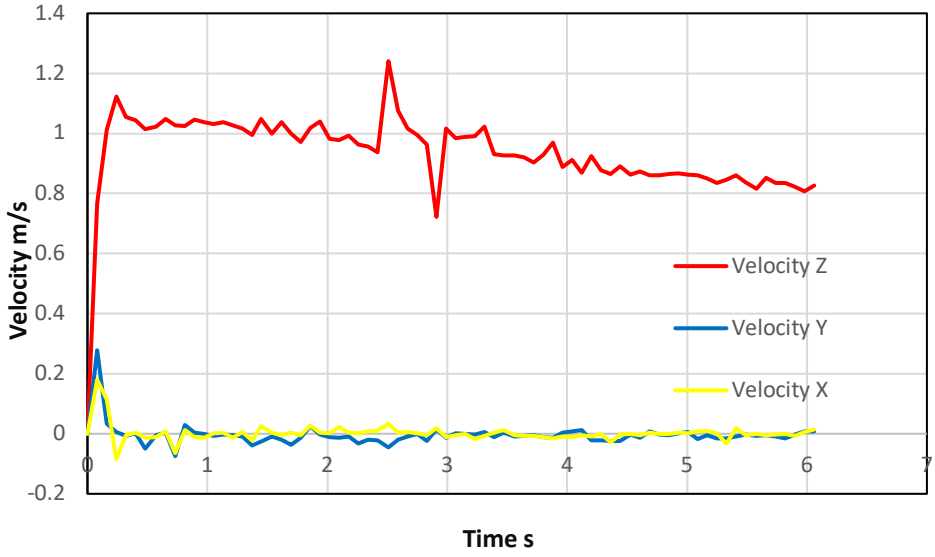

Fig. 72. Velocity components for horizontal annulus at annular velocity 1m/s.

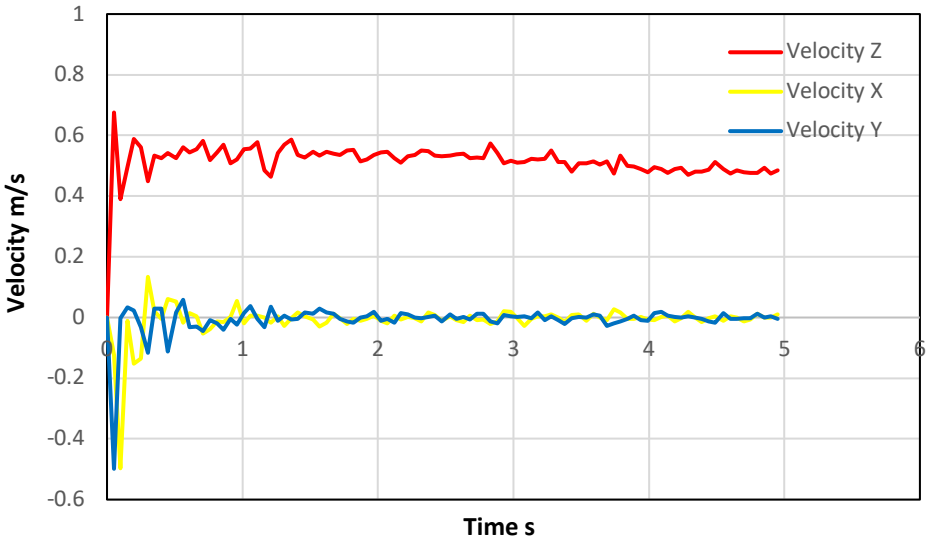

Fig. 73. Velocity components for vertical annulus at annular velocity 0.5 m/s.

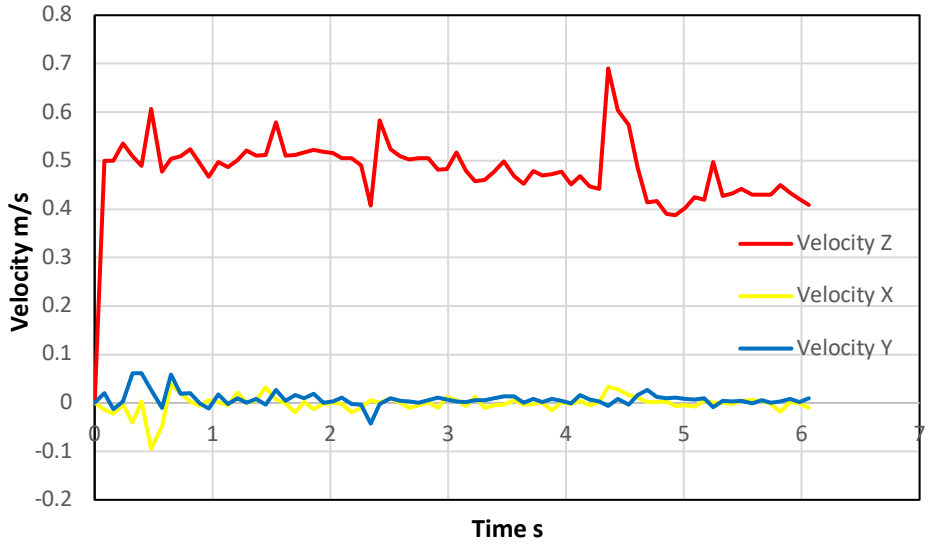

Fig. 74. Velocity component for inclined $\mathbf{45}^{\circ}$ at annular velocity 0.5 m/s.

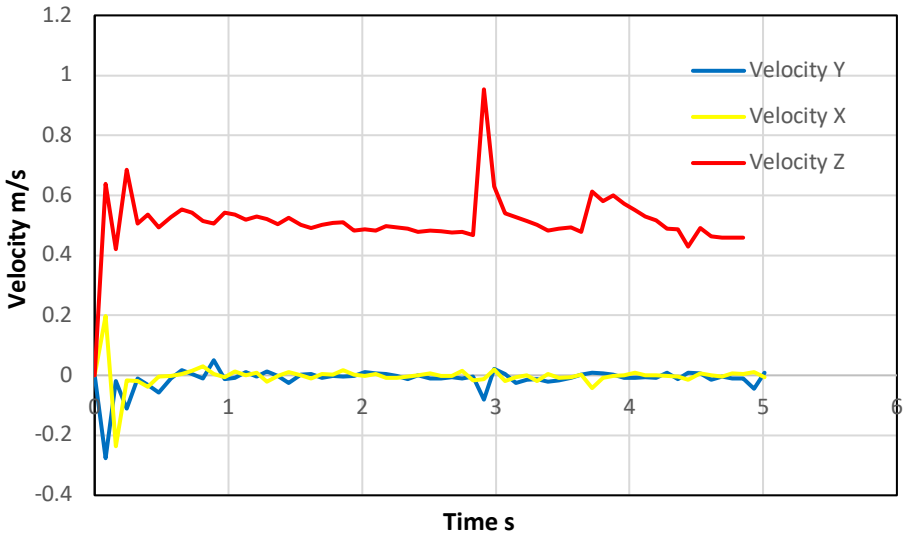

Fig. 75. Velocity components for horizontal annulus at annular velocity 0.5 m/s.

Chapter 6

Conclusions and Future Work

6. Conclusions and Future Work

In this final chapter, the conclusions for the findings of the two results chapters are given sequentially in section 6.1 followed by the recommendations for future work in section 6.2.

6.1 Conclusions

The work described in this study is undertaken to gain insight into fundamental aspects of hole cleaning process in oil-well drilling operation and effective parameters in drilling cuttings transport in annulus. In particular, the influence of particle (cuttings) interaction and fluid phase (mud) behaviour in cuttings transport in vertical and deviated annuli are investigated. Pervious experimental works and challenges associated with cuttings transport in annulus were reviewed and found that it is expensive and difficult to investigate the effects of various key parameters simultaneously. Many investigations were carried out to model cuttings transport in annulus using CFD, mainly in Eulerian framework, where only the continuous phase is considered and the solid phase character is lost in simulations. Finally, the recent studies on transportation mechanism in hole cleaning process using four-way coupling CFD-DEM method were reviewed. It found that a systematic study of the impact of mud rheology on drilling cuttings transport in annulus with appropriate mesh refinement for particle-fluid interaction near the wall region is still lacking in the literature. Through comprehensive investigation of previous studies, this work focused on optimisation of the hole cleaning in annulus using the numerical method based on Reynolds stress model (RES) embodied in commercial CFD code FLUENT, with flow solution provided by this method coupled to a second commercial code, EDEM, built on the discrete element method (DEM) which is employed for the prediction of the cuttings transport in the annulus.

In this study, relative cuttings concentration (RCC) is defined to represent the cuttings transport performance in annulus. In the terms of the effects of mud rheology on the cuttings transport, where the mud behavior obeys the Herschel-Buckley viscosity model, three types of mud viscosity with different yield value have examined in CFD-DEM model. The results generated for three yields values (YP=0.5 Pa, YP= 4 Pa and YP= 8 Pa) versus different annular velocities of V= 0.5 m/s, V= 1 m/s and V= 1.5 m/s in horizontal annulus showed a significant reduction in relative cuttings concentration by increasing the annular velocity from 0.5 m/s to 1.5 m/s. Reductions of 50.6 % for higher yield point (YP= 8 Pa), 50% for intermediate yield point (YP= 4 Pa) and 55% for lower yield point (YP=0.5) are recorded. At constant velocity of 0.5 m/s, RCC reduces 15 % from YP= 8 Pa to YP=0.5 and for velocity of 1.5 m/s, RCC reduces 5.5 % from YP= 8 Pa to YP=0.5. It is founded that the influence of yield value is more pronounced at lower annular velocities. Also, the sensitivity of yield point against inclination of angles is tested where changing mud from YP= 8 Pa to YP=0.5 at constant velocity of 1 m/s caused 17%, 34% and 32% reduction in RCC within vertical, inclined $45°$ and horizontal annuli, respectively.

The effects of particle size on hole cleaning efficiency is investigated for two average particle diameters of $d_p = 1mm$ and $d_p = 1.4mm$ in horizontal annulus. Simulation results of relative cuttings concentration versus different annular mud velocities showed 7% increase in RCC for larger particle size at constant velocity of 0.5 m/s, 6% increase at velocity of 1 m/s and 4% increase for the velocity of 1.5 m/s. Larger particle size of $d_p = 1.4mm$ faced a reduction of 50% in RCC for changing the mud annular velocity from V= 0.5 m/s to V= 1.5 m/s where RCC decreases around 60% for the smaller particle size of $d_p = 1mm$. Drilling cuttings transport in annulus is more improved with higher annular velocity for smaller particle size.

The impact of wellbore deviation on RCC for HVM is studied at different annular velocities of V= 0.5 m/s, V= 1 m/s and V= 1.5 with 60 rpm inner pipe rotation where dissimilar cuttings flow mechanism were observed at vertical and deviated annuli. Increasing annular velocity from 0.5 m/s to 1.5 m/s caused a 37% reduction of RCC in vertical annulus where by increasing the annular velocity RCC decreased 49% in horizontal annulus. Cuttings sliding flow mechanism at middle inclination, caused an irregular behaviour at low velocity of 0.5 m/s where the cuttings sliding on the lower wall of the annulus nullified the impact of

annular velocity. This phenomenon is not observed at higher velocity of 1 m/s and 1.5 m/s where the influence of annular velocity is dominant.

The effect of drill pipe rotation on hole cleaning in horizontal annulus at various annular mud velocities is investigated where the increasing drill pipe rotation from zero to 120 RPM caused 15%, 6% and 5% reductions in RCC at velocities of 0.5, 1 and 1.5 m/s, respectively. Also, the effects of drill pipe rotation on RCC at various annular velocities are tested in vertical and deviated $45°$ annuli. Increasing drill pipe rotation up to 60 RPM had negligible effect on vertical annulus, while at annular velocity of 0.5 m/s showed a reduction of 8% and 7% in inclined ($45°$) and horizontal annuli, respectively. The RCC reduction at higher velocities of 1 m/s and 1.5 m/s is almost negligible.

The research makes an original contribution to the literature in applying predictive techniques for hole cleaning study in oil and gas drilling with focus on mud rheology. It profits fundamental understanding of how cuttings transport is affected by different mud rheology, cuttings size, inclination of angle and drill pipe rotation and how those parameters affect the cuttings concentration in annulus and hole cleaning efficiency.

All in all, the main findings of this study can be abbreviated as follows:

1. Mud annular velocity role has dominant effect and it shows better performance and higher cleaning efficiency with increasing to its limiting value for all range of well inclinations, practically for higher angles of inclination.
2. The annular relative cuttings concentration RCC is lower for higher YP and it is observed that high viscosity mud with higher value of YP is effective for all inclination.
3. The effect of YP value is more pronounced at lower annular mud velocities and by increasing the velocity the impact of YP is reduced.
4. The cuttings size with smaller diameter transported easier than larger particles with same density and both cuttings size shows high sensitivity to higher value of velocities.
5. Impact of drill pipe rotation is more pronounced for lower value of annular mud velocities. Increasing drill pipe rotation from zero to 120 rpm improves the cleaning efficiency in deviated annuli at lower velocities where it is almost negligible at vertical annulus.

6.2 Recommendations for Future Work

A list of suggestions for future work based on the findings of this study is given:

1. In this work, the cuttings transport efficiency is studied in the annular space by investigating the impact of different parameters on relative cuttings concentration where the bottom hole of the well (near drill bit) with the effects of highly concentrated particle-fluid mixture can be considered in future work. Specifically, a focus can be made on the study of the effects of nozzle configuration, geometry, size and number of orifices (drill bit hydraulics) on cuttings transport efficiency.
2. Analysis of the influence of parameters controlling the non-Newtonian mud behaviour i.e. consist index (*k*), fluid behaviour index (*n*) and can be expanded in the mud rheology studies.
3. In this work, the impact of mud rheology on cleaning efficiency is investigated base on water-based mud properties. Improving the performance of oil-base mud in high temperature and complex wells can be the subject for the future work.
4. The study can be extended to faster generation rate (as a result of higher drilling rate) to understand the cleaning efficiency for higher drilling ranges.
5. Different cuttings size distribution can be investigated where the particles could be larger than the computational mesh size. This can be achieved using resolved CFD-DEM techniques which is computationally expensive, but it can be interesting in order to obtain high accuracy results in simulations. Unresolved CFD-DEM uses empirical drag force models to characterise particle-fluid interaction where the resolved CFD-DEM uses a very fine mesh and particles interaction is characterised with higher accuracy in comparison with unresolved CFD-DEM. Therefore, investigating the simulation gap between the resolved CFD-DEM and unresolved CFD-DEM through a size effect study in order to improve the accuracy of simulations in cutting transport efficiency can be considered in future work.

References

1. Ramsey, M.S., *Practical wellbore hydraulics and hole cleaning: unlock faster, more efficient, and trouble-free drilling operations*. 2019: Gulf Professional Publishing.
2. Katende, A., et al., *Improving the performance of oil based mud and water based mud in a high temperature hole using nanosilica nanoparticles.* 2019. **577**: p. 645-673.
3. Akhshik, S., et al., *CFD–DEM approach to investigate the effect of drill pipe rotation on cuttings transport behavior.* 2015. **127**: p. 229-244.
4. Osgouei, R., et al., *A New Model to Determine the Two-phase Drilling Fluid Behavior Through Horizontal Eccentric Annular Geometry, Part A: Flow Pattern Identification and Liquid Hold-up Estimation.* 2015. **37**(15): p. 1663-1673.
5. Akhshik, S., M. Behzad, and M.J.P. Rajabi, *CFD-DEM simulation of the hole cleaning process in a deviated well drilling: the effects of particle shape.* 2016. **25**: p. 72-82.
6. Cameron, C. *Drilling fluids design and management for extended reach drilling*. in *SPE/IADC Middle East Drilling Technology Conference*. 2001. OnePetro.
7. Rowe, P., *Drag forces in a hydraulic model of a fluidized bed-part I.* Trans. Inst. Chem. Eng., 1961. **39**: p. 43-54.
8. Schwarzkopf, J.D., et al., *Multiphase flows with droplets and particles*. 2011: CRC press.
9. Zeidler, H.U., *An experimental analysis of the transport of drilled particles in an annulus*. 1970.
10. Abrahamson, J., *Collision rates of small particles in a vigorously turbulent fluid.* Chemical Engineering Science, 1975. **30**(11): p. 1371-1379.
11. Elghobashi, S., *On predicting particle-laden turbulent flows.* Applied scientific research, 1994. **52**(4): p. 309-329.
12. Okrajni, S. and J. Azar, *The effects of mud rheology on annular hole cleaning in directional wells.* SPE Drilling Engineering, 1986. **1**(04): p. 297-308.
13. Brown, N., P. Bern, and A. Weaver. *Cleaning deviated holes: New experimental and theoretical studies*. in *SPE/IADC Drilling Conference*. 1989. Society of Petroleum Engineers.
14. Tomren, P., A. Iyoho, and J.J.S.D.E. Azar, *Experimental study of cuttings transport in directional wells.* 1986. **1**(01): p. 43-56.
15. Peden, J., J. Ford, and M. Oyeneyin. *Comprehensive experimental investigation of drilled cuttings transport in inclined wells including the effects of rotation and eccentricity*. in *European Petroleum Conference*. 1990. Society of Petroleum Engineers.

16. Sifferman, T. and T. Becker, *Hole cleaning in full-scale inclined wellbores.* SPE Drilling Engineering, 1992. **7**(02): p. 115-120.

17. Bassal, A.A., *The effect of drillpipe rotation on cuttings transport in inclined wellbores*. 1995, University of Tulsa.

18. Sanchez, R.A., et al. *The effect of drillpipe rotation on hole cleaning during directional well drilling*. in *SPE/IADC drilling conference*. 1997. Society of Petroleum Engineers.

19. Alfredo Sanchez, R., et al., *Effect of Drillpipe Rotation on Hole Cleaning During Directional-Well Drilling*. Vol. 4. 1999. 101-108.

20. Yu, M., et al. *An experimental study of hole cleaning under simulated downhole conditions*. in *SPE annual technical conference and exhibition*. 2007. OnePetro.

21. Bilgesu, H., et al. *Computational Fluid Dynamics (CFD) as a tool to study cutting transport in wellbores*. in *SPE Eastern Regional Meeting*. 2002. Society of Petroleum Engineers.

22. Bilgesu, H.I., N. Mishra, and S. Ameri. *Understanding the effect of drilling parameters on hole cleaning in horizontal and deviated wellbores using computational fluid dynamics*. in *Eastern Regional Meeting*. 2007. Society of Petroleum Engineers.

23. Wang, Z.-m., M. Li, and Y.-k. Hong, *Effect of drillpipe rotation on borehole cleaning for extended reach well.* Journal of Hydrodynamics, 2009. **21**(3): p. 366-372.

24. Han, S.-M., et al., *Solid–liquid hydrodynamics in a slim hole drilling annulus.* Journal of Petroleum Science and Engineering, 2010. **70**(3-4): p. 308-319.

25. Osgouei, R.E., M.E. Ozbayoglu, and T.K. Fu. *CFD simulation of solids carrying capacity of a newtonian fluid through horizontal eccentric annulus*. in *ASME 2013 Fluids Engineering Division Summer Meeting*. 2013. American Society of Mechanical Engineers.

26. Rooki, R., et al., *Simulation of cuttings transport with foam in deviated wellbores using computational fluid dynamics.* Journal of Petroleum Exploration and Production Technology, 2014. **4**(3): p. 263-273.

27. Sun, X., et al., *Effect of drillpipe rotation on cuttings transport using computational fluid dynamics (CFD) in complex structure wells.* Journal of Petroleum Exploration and Production Technology, 2014. **4**(3): p. 255-261.

28. Wang, Z.-m. and Z.-h. Long, *Study on three-layer unsteady model of cuttings transport for extended-reach well.* Journal of Petroleum Science and Engineering, 2010. **73**(1-2): p. 171-180.

29. Mohammadzadeh, K., S. Hashemabadi, and S. Akbari, *CFD simulation of viscosity modifier effect on cutting transport by oil based drilling fluid in wellbore.* Journal of Natural Gas Science and Engineering, 2016. **29**: p. 355-364.

30. Amanna, B., M.R.K.J.J.o.N.G.S. Movaghar, and Engineering, *Cuttings transport behavior in directional drilling using computational fluid dynamics (CFD).* 2016. **34**: p. 670-679.

31. Yilmaz, D., *Discrete phase simulations of drilled cuttings transport process in highly deviated wells*. 2013, Louisiana State University.

32. Tsuji, Y., T. Tanaka, and T. Ishida, *Lagrangian numerical simulation of plug flow of cohesionless particles in a horizontal pipe.* Powder technology, 1992. **71**(3): p. 239-250.

33. Akhshik, S., et al., *CFD–DEM model for simulation of non-spherical particles in hole cleaning process.* 2015. **33**(5): p. 472-481.

34. Akhshik, S., et al., *On the particle–particle contact effects on the hole cleaning process via a CFD–DEM model.* 2016. **34**(6): p. 736-743.

35. Akhshik, S., M.J.J.o.P.S. Rajabi, and Engineering, *CFD-DEM modeling of cuttings transport in underbalanced drilling considering aerated mud effects and downhole conditions.* 2018. **160**: p. 229-246.

36. Osgouei, R.E., M.E. Ozbayoglu, and T.K. Fu. *CFD simulation of solids carrying capacity of a newtonian fluid through horizontal eccentric annulus*. in *Fluids Engineering Division Summer Meeting*. 2013. American Society of Mechanical Engineers.

37. Osgouei, R.E.J.M.E.T.U., *Determination of cuttings transport properties of gasified drilling fluids.* 2010. **1**.

38. Model, T., et al., *Chapter 10. Modeling Turbulence.* 2001: p. 1-102.

39. Sun, B., et al., *Modeling of the critical deposition velocity of cuttings in an inclined-slimhole annulus.* 2017. **22**(04): p. 1213-1224.

40. Tsuji, Y., T. Kawaguchi, and T.J.P.t. Tanaka, *Discrete particle simulation of two-dimensional fluidized bed.* 1993. **77**(1): p. 79-87.

41. Shao, B., et al., *A study on non-spherical cuttings transport in CBM well drilling by coupled CFD-DEM.* 2019. **13**(1): p. 579-590.

42. Yan, T., et al., *Numerical investigation on horizontal wellbore hole cleaning with a four-lobed drill pipe using CFD-DEM method.* 2020. **375**: p. 249-261.

43. Akhshik, S., M. Behzad, and M. Rajabi, *CFD-DEM simulation of the hole cleaning process in a deviated well drilling: The effects of particle shape.* Particuology, 2016. **25**: p. 72-82.

44. Alobaid, F. and B.J.P. Epple, *Improvement, validation and application of CFD/DEM model to dense gas–solid flow in a fluidized bed.* 2013. **11**(5): p. 514-526.

45. Beetstra, R., M.A. van der Hoef, and J.J.A.j. Kuipers, *Drag force of intermediate Reynolds number flow past mono-and bidisperse arrays of spheres.* 2007. **53**(2): p. 489-501.

46. Cello, F., A. Di Renzo, and F.P.J.C.E.S. Di Maio, *A semi-empirical model for the drag force and fluid–particle interaction in polydisperse suspensions.* 2010. **65**(10): p. 3128-3139.

47. Cheng, N.-S.J.P.T., *Comparison of formulas for drag coefficient and settling velocity of spherical particles.* 2009. **189**(3): p. 395-398.

48. Deb, S. and D.K.J.P.t. Tafti, *A novel two-grid formulation for fluid–particle systems using the discrete element method.* 2013. **246**: p. 601-616.

49. Hill, R.J., D.L. Koch, and A.J.J.J.o.F.M. Ladd, *Moderate-Reynolds-number flows in ordered and random arrays of spheres.* 2001. **448**: p. 243-278.

50. Hölzer, A. and M.J.P.T. Sommerfeld, *New simple correlation formula for the drag coefficient of non-spherical particles.* 2008. **184**(3): p. 361-365.

51. Kafui, K., C. Thornton, and M.J.C.E.S. Adams, *Discrete particle-continuum fluid modelling of gas–solid fluidised beds.* 2002. **57**(13): p. 2395-2410.

52. Kuang, S., et al., *Computational investigation of horizontal slug flow in pneumatic conveying.* 2008. **47**(2): p. 470-480.

53. Peng, Z., et al., *Influence of void fraction calculation on fidelity of CFD-DEM simulation of gas-solid bubbling fluidized beds.* 2014. **60**(6): p. 2000-2018.

54. Schiller, L.J.Z.V.D.I., *A drag coefficient correlation.* 1933. **77**: p. 318-320.

55. van der Hoef, M.A., R. Beetstra, and J.J.J.o.f.m. Kuipers, *Lattice-Boltzmann simulations of low-Reynolds-number flow past mono-and bidisperse arrays of spheres: results for the permeability and drag force.* 2005. **528**: p. 233-254.

56. Van Wachem, B. and A.-E.J.C.E.J. Almstedt, *Methods for multiphase computational fluid dynamics.* 2003. **96**(1-3): p. 81-98.

57. Wee Chuan Lim, E., C.H. Wang, and A.B.J.A.j. Yu, *Discrete element simulation for pneumatic conveying of granular material.* 2006. **52**(2): p. 496-509.

58. Wu, C., A. Berrouk, and K.J.C.E.J. Nandakumar, *Three-dimensional discrete particle model for gas–solid fluidized beds on unstructured mesh.* 2009. **152**(2-3): p. 514-529.

59. Wu, C., et al., *Accurate void fraction calculation for three-dimensional discrete particle model on unstructured mesh.* 2009. **64**(6): p. 1260-1266.

60. Xiao, H. and J.J.C.i.C.P. Sun, *Algorithms in a robust hybrid CFD-DEM solver for particle-laden flows.* 2011. **9**(2): p. 297-323.

61. Zhao, J. and T.J.P.t. Shan, *Coupled CFD–DEM simulation of fluid–particle interaction in geomechanics.* 2013. **239**: p. 248-258.

62. Zhou, H., et al., *Lagrangian approach for simulating the gas-particle flow structure in a circulating fluidized bed riser.* 2002. **28**(11): p. 1801-1821.

63. Xu, C., et al., *Squeeze flow of interstitial Herschel–Bulkley fluid between two rigid spheres.* 2010. **8**(4): p. 360-364.

64. Andersson, B., et al., *Computational fluid dynamics for engineers*. 2011: Cambridge university press.

65. Pang, Y.S., et al., *A Computational Fluid Dynamics Study of Turbulence, Radiation, and Combustion Models for Natural Gas Combustion Burner.* 2018. **13**(1): p. 155-169.

66. Bird, R., W. Stewart, and E.J.I. Lightfoot 2nd, Hoboken, NJ, *Transport phenomena 2nd edn. John Wiely and Sons.* 2002.

67. Daly, B.J. and F.H.J.T.p.o.f. Harlow, *Transport equations in turbulence.* 1970. **13**(11): p. 2634-2649.

68. Ge, J., *Modeling and Experimental Study of Fluid Dynamics of Sand Granular Flow for Core Making*. 2018, The University of Alabama at Birmingham.

69. Han, T., A. Levy, and H.J.P.T. Kalman, *DEM simulation for attrition of salt during dilute-phase pneumatic conveying.* 2003. **129**(1-3): p. 92-100.

70. Kawaguchi, T., et al., *Quasi-three-dimensional numerical simulation of spouted beds in cylinder; Ento yokinai funryuso no junsanjigenteki suchi simulation.* 1998. **64**.

71. Kawaguchi, T., T. Tanaka, and Y.J.P.t. Tsuji, *Numerical simulation of two-dimensional fluidized beds using the discrete element method (comparison between the two-and three-dimensional models).* 1998. **96**(2): p. 129-138.

72. Kuwagi, K., T. Mikami, and M.J.P.T. Horio, *Numerical simulation of metallic solid bridging particles in a fluidized bed at high temperature.* 2000. **109**(1-3): p. 27-40.

73. Liffman, K. and M.J.C.E.S. Nguyen, *Onset of cohesive behaviour in gas fluidized beds: a numerical study using DEM simulation.* 2001. **56**: p. 4433-4438.

74. Mikami, T., H. Kamiya, and M.J.C.E.S. Horio, *Numerical simulation of cohesive powder behavior in a fluidized bed.* 1998. **53**(10): p. 1927-1940.

75. Ouyang, J. and J.J.C.E.S. Li, *Particle-motion-resolved discrete model for simulating gas–solid fluidization.* 1999. **54**(13-14): p. 2077-2083.

76. Rhodes, M.J., et al., *Use of discrete element method simulation in studying fluidization characteristics: influence of interparticle force.* 2001. **56**(1): p. 69-76.

77. Rhodes, M.J., et al., *Study of mixing in gas-fluidized beds using a DEM model.* 2001. **56**(8): p. 2859-2866.

78. Rong, D., T. Mikami, and M.J.C.E.S. Horio, *Particle and bubble movements around tubes immersed in fluidized beds–a numerical study.* 1999. **54**(23): p. 5737-5754.

79. Feng, Y., A.J.I. Yu, and e.c. research, *Assessment of model formulations in the discrete particle simulation of gas− solid flow.* 2004. **43**(26): p. 8378-8390.

80. Wen, C.Y. *Mechanics of fluidization*. in *Chem. Eng. Prog. Symp. Ser.* 1966.

81. Ergun, S.J.C.E.P., *Fluid flow through packed columns.* 1952. **48**: p. 89-94.

82. Gidaspow, D., *Multiphase flow and fluidization: continuum and kinetic theory descriptions*. 1994: Academic press.

83. Hoomans, B., et al., *Discrete particle simulation of bubble and slug formation in a two-dimensional gas-fluidised bed: a hard-sphere approach.* 1996. **51**(1): p. 99-118.

84. Johnson, K.L., et al., *Surface energy and the contact of elastic solids.* 1971. **324**(1558): p. 301-313.

85. Cundall, P.A. and O.D.J.g. Strack, *A discrete numerical model for granular assemblies.* 1979. **29**(1): p. 47-65.

86. Schetz, J.A. and A.E. Fuhs, *Fundamentals of fluid mechanics*. 1999: John Wiley & Sons.

87. Okrajni, S. and J.J.S.D.E. Azar, *The effects of mud rheology on annular hole cleaning in directional wells.* 1986. **1**(04): p. 297-308.

88. Balhoff, M.T., et al., *Rheological and yield stress measurements of non-Newtonian fluids using a Marsh Funnel.* 2011. **77**(3-4): p. 393-402.

89. Munson, B.R., D.F. Young, and T.H.J.O.L.R. Okiishi, *Fundamentals of fluid mechanics.* 1995. **10**(42): p. 831.

90. Al-Khdheeawi, E.A. and D.S.J.E. Mahdi, *Apparent viscosity prediction of water-based muds using empirical correlation and an artificial neural network.* 2019. **12**(16): p. 3067.

91. Sifferman, T.R., et al., *Drill cutting transport in full scale vertical annuli.* 1974. **26**(11): p. 1295-1302.

92. Iyoho, A.W., *DRILLED-CUTTINGS TRANSPORT BY NON-NEWTONIAN DRILLING FLUIDS THROUGH INCLINED, ECCENTRIC ANNULI.* 1981.

93. Tomren, P.H., *The transport of drilled cuttings in an inclined eccentric annulus*. 1979: University of Tulsa, Library, Thesis Duplication Service.

94. He, Y., A.E. Bayly, and A.J.P.T. Hassanpour, *Coupling CFD-DEM with dynamic meshing: A new approach for fluid-structure interaction in particle-fluid flows.* 2018. **325**: p. 620-631.

95. Clark, R. and K. Bickham. *A mechanistic model for cuttings transport*. in *SPE Annual Technical Conference and Exhibition*. 1994. Society of Petroleum Engineers.